University of Neuchâtel
Faculty of Science

Centre for Hydrogeology
and Geothermics (CHYN)

Ph.D. Thesis

Laboratory and numerical study of hyporheic flow in karst conduits and its effect on sediment-entrapped DNAPLs

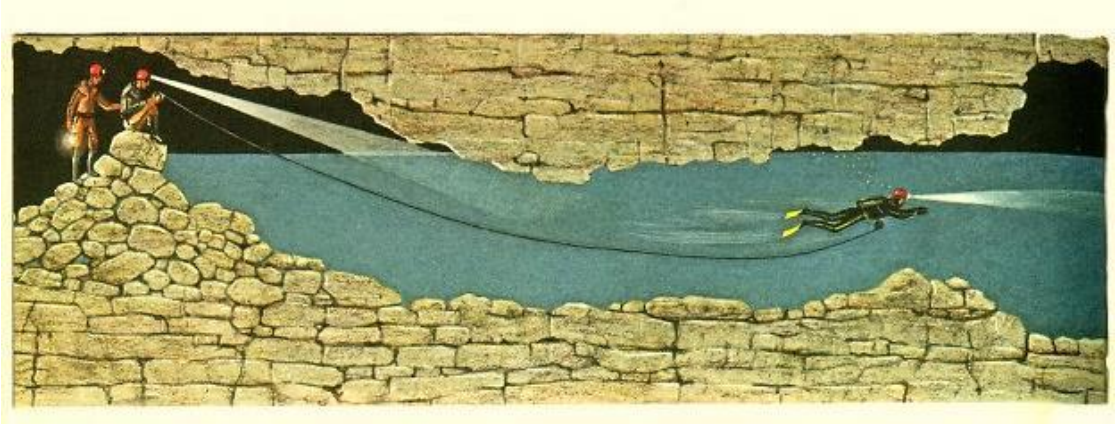

presented to the Faculty of Science of the University of Neuchâtel to satisfy the requirements of the degree of Doctor of Philosophy in Science

by

Yuexia Wu

Thesis defense date: 25.11.2013

Public presentation date: 18.12.2013

Ph.D. thesis evaluation committee:

Prof. Dr Daniel Hunkeler, University of Neuchâtel (Director of the thesis)

Prof. Dr Pierre Perrochet, University of Neuchâtel

Prof. Dr Nico Goldscheider, Karlsruhe Institute of Technology

UNIVERSITÉ DE NEUCHÂTEL

Faculté des sciences
Secrétariat-décanat de Faculté
Rue Emile-Argand 11
2000 Neuchâtel - Suisse
Tél: + 41 (0)32 718 2100
E-mail: secretariat.sciences@unine.ch

IMPRIMATUR POUR THESE DE DOCTORAT

La Faculté des sciences de l'Université de Neuchâtel autorise l'impression de la présente thèse soutenue par

Madame Yuexia WU

Titre:

Laboratory and numerical study of hyporheic flow in karst conduits and its effect on sediment-entrapped DNAPLs

sur le rapport des membres du jury composé comme suit:

- Prof. Daniel Hunkeler, Université de Neuchâtel, directeur de thèse
- Prof. Pierre Perrochet, Université de Neuchâtel,
- Prof. Nico Goldscheider, Karlsruhe Institute for Technology, Karlsruhe, Allemagne

Neuchâtel, le 9 décembre 2013

Le Doyen, Prof. P. Kropf

Acknowledgements

I would like to thank all the persons that contributed to the accomplishment of my PhD thesis:

— Prof. Daniel Hunkeler, my PhD director & friend out of PhD life, is definitely one of the most important persons, during not only my PhD work, but also in my future career who impresses and influences me by his rigorous attitudes in working on scientific research, the innovative and cautious way of thinking. Without his advices, patience, encouragements, great support in my research work, I would not be able to complete my PhD thesis. I am grateful to his accompany throughout my PhD journey, in developing the ideas, trying out lab experiments, finding out resolutions to problems, sharing interesting and exciting findings.

— Roberto Costa, for his help in setting up the laboratory apparatus. My laboratory experiments were always encouraged and progressed with his excellent work of making things come true. Pierre Schnegg, for his coordinates with Roberto Costa in successfully realizing the function of the laboratory model. Dr. Sven Friedel and Zoran Vidakovic from COMSOL, Inc. for their great technical support in numerical modeling.

— Prof. Nico Goldscheider, for his introducing me to CHYN, and his advices on defining my PhD thesis at the very beginning. Prof. Pierre Perrochet, for his helpful discussions on numerical modeling and help in resolving some mathematical and numerical problems step-by-step.

— All the members of the hydrochemistry and contaminants group, Florian Breider, Simon Jeannottat, Bibiane Schlunegger, Jordi Palau Capdevilla, Daniel Bouchard for their help in everyday laboratory troubleshooting, Christian Moeck for his discussion and help in correcting some of the chapters, and Daniel Käser, Alice Badin, Jessie Meeks, Philipp Wanner, Clara Laugsch, Oliver Schilling. I enjoyed very much the working atmosphere and communications in science, life with them.

— The Chinese community, especially all my friends in IMT-EPFL who are all on their PhD in Neuchâtel. Time with them cured my homesickness. Thanks particularly to Dr Hui Gao for her countless lunch-time scientific advices in carrying out my laboratory experiments, to Hailan Nong for assisting my laboratory work during weekends even, and to Xinchang Liu for his critical comments on some questions referring to mathematics and physics.

— All the CHYN members, especially to Prof. Jean-Paul Schaer, who showed me some local geological background, which made me more love Switzerland and Neuchâtel.

— My parents, for their great support of my studying abroad and understanding of my absence in every family dinner during the past several years.

— The chinese scholarship council (CSC) who provides me 4-years scholarship to study in Switzerland, and financial support from Prof. Daniel Hunkeler and Prof. Pierre Perrochet.

Extended abstract

Contamination of karst aquifer, particularly by organic compounds, such as the Dense Non-aqueous Phase Liquids (DNAPLs) constitutes a threat for water supply and the environment. Due to the presence of large openings in karst systems and the high density of DNAPLs they may frequently reach conduits and accumulate at low points such as siphon structures that likely also contain sediments. Hence sediment-entrapped DNAPLs are commonly encountered and present as a continuous phase of organic liquid denoted as DNAPL pool. DNAPLs present in conduits are particularly problematic for the water quality as most of the flow in karst systems transits through conduits before reaching springs. The longevity of DNAPL pools will depend on the flow of water through the sediment which is referring to as karst hyporheic flow. In contrast to surface water, hyporheic exchange has received little attention so far, although it has potentially a strong influence on the fate of contaminants in karst systems. The thesis addressed this lack of knowledge. The objective of the thesis was first to verify whether karst hyporheic flow could occur between the conduit and sediments, and second, to investigate how the hyporheic flow mediates the dissolution of sediment-entrapped DNAPL pools. A laboratory analog resembling a siphon conduit partly filled with sediments was built to investigate hyporheic flow and DNAPL pool dissolution. Experiments with the laboratory analog and numerical modeling are the main research approaches throughout this study.

First, the driving force and characteristics of hyporheic exchange between the conduit and sediment system was investigated using the laboratory analog model. Influences of conduit flow (expressed as Reynolds number *Re*), conduit angle and sediment properties (grain size/permeability) on the flow pattern and magnitude of hyporheic exchange were explored. Sediment-source tracer tests were carried out at varied flow rates for sediments of variable grain size to characterize hyporheic flow patterns and to evaluate solute transport processes (by the mean travel time MTT and dispersion of tracer plume σ^2). Numerical modeling with a two-domain approach assuming pressure continuity across the conduit-sediment interface was employed to simulate the sediment-source tracer tests and flow fields. Results of the sediment-source tracer tests showed that MTT and σ^2 decreased with increasing conduit *Re* and increasing sediment permeability, and were smaller for the steeper conduit angle. Flow pattern in the sediment was characterized by zones of forward and reverse flow induced by the conduit bends. Simulation of the pressure fields showed that flow in sediment was driven by the pressure gradients along the sediment and water interface (SWI), imposed by the overlying conduit flow. While in streambeds, pressure gradients are usually induced by the sediment surface topography, in the current investigated system enhanced pressure gradients occurred on top of a flat sediment surface due to the conduit bends. The observed and simulated flow patterns in different sediments were identical under the same conduit *Re* for the same conduit angle. However, the magnitude of flow in the sediment varied with sediment permeability for the same conduit *Re* and geometry. The calculated exchange flux q_{int} by numerical simulations increased linearly with the conduit *Re* for all

types of sediment and conduit angle, and was higher for a steeper conduit angle. The relationships established among q_{int} and the various controlling factors also suggested that sediment properties had the strongest influence on the exchange flux.

Based on these insights into the karst hyporheic flow, the dissolution of a sediment-entrapped DNAPL pool facilitated by hyporheic flow was further investigated by the same analog model and numerical simulations. Influences of conduit flow and conduit angle on the dissolution rate were evaluated. Dissolution experiments with a well-defined DNAPL pool consisting of a surrogate compound were carried out to quantify the mass transfer rate. Soluble tracer test with a solidified pool was performed to visually trace the solute plume dissolved from DNAPL pool surface, and was compared to the DNAPL pool dissolution reproduced by numerical modeling. The mass transfer coefficient k_m, calculated with the effluent concentration at steady state from dissolution experiments was used to quantify the mass transfer rate. The experimental k_m were compared with the values calculated by numerical simulations. The dissolution rate for the conduits-sediment system was also compared to the well investigated pool dissolution in a semi-infinite porous media as a reference case. The observed k_m increased with the conduit *Re* and was higher for the steeper conduit angle, which were in agreement with the results from numerical simulations. Both the observed and simulated k_m increased linearly with the average groundwater flow velocity $\overline{U}$ in the sediment. However, k_m were higher compared to the values predicted by a 2D analytical model which is conventionally applied for the semi-infinite porous media. The higher k_m was likely due to the hyporheic flow pattern characterized by upward curved streamlines in karst conduit sediment. The curved streamlines carry dissolved compounds away from the DNAPL/water interface, while in a semi-infinite porous media upward transport only occurs by transverse dispersion.

In conclusion, the study confirmed the occurrence of hyporheic flow between karst conduit and sediment through a laboratory analog investigation. Pressure gradient along the sediment and water interface drove the exchange of flow and solute between the conduit and sediment domains. Conduit flow condition, sediment properties and conduit geometry/angle played a combined role in the hyporheic exchange between conduit and sediment. The pattern of hyporheic flow was controlled by the conduit flow rate and conduit angle. The magnitude of flow in sediment was determined by sediment permeability. The exchange flux increased with the conduit flow rate and sediment permeability and was higher in steeper angle conduit. Sediment grain size/permeability had the strongest influence on the magnitude of exchange flux in contrast to conduit flow and conduit angle. The mass transfer rate of hyporheic flow-mediated DNAPL pool dissolution was found to increase linearly with the average groundwater flow velocity in sediment. The study highlights that a higher mass transfer rate/shorter longevity is to be expected in the shallow karst conduit sediment than in a semi-infinite porous medium due to the influence of the hyporheic flow pattern. The study of potential karst hyporheic flow and relevant processes has implications on the sequestration, transportation and transformation of contaminants in karst aquifer. The exchange of flow and solutes between conduit and sediment potentially plays a significant role in the biogeochemical and karstification processes as

well. While the study clearly highlighted the mechanism of hyporheic exchange and its potential role on contaminant fate, further studies are required that approach field conditions in more detail. In particular, the upper limit of the flow rate should be extended to the turbulent range, effect of sediment movement of contaminant fate should be considered and the effect of more complex conduits geometries and sediment assemblies should be explored.

Keywords:

karst hyporheic flow, conduit and sediment, DNAPL pool dissolution, exchange flux, mass transfer coefficient

Table of Contents

Notation

a radius of conduit, L

A_{na} surface contact area, L^2

a_{na} specific interfacial area between non-aqueous and aqueous phases per unit volume, L^2/L^3

b thickness of sediment layer, L

C aqueous phase solute concentration, M/L^3

C_s solute solubility concentration, M/L^3

C_∞ aqueous phase solute concentration far away from source zone, M/L^3

C_{out} average effluent concentration, M/L^3

$\overline{d}_p$ mean grain size of a porous media, L

Da dimensionless Darcy number, expressed as k/h^2, k is the permeability of underlying porous media, h is the height of flow column

D_L, D_{TH}, D_{TV} longitudinal, transverse horizontal and, transverse vertical directions, respectively, L

D_m molecular diffusion coefficient, L^2/T

D_e effective molecular diffusion coefficient, L^2/T

g gravitational acceleration, L/T^2

H conduit diameter, L

J solute mass flux to aqueous phase, $M/L^2/T$

$K°$ mass transfer rate coefficient, $1/T$

k_m time invariant overall mass transfer coefficient, L/T

k permeability of porous media, L^2

K hydraulic conductivity, L/T

L_o length scale of the solute plume, L

L_p pool length, L

l characteristic length , denotes to the stagnant layer thickness δ, or mean grain size of a porous media $\overline{d}_p$, or conduit diameter H, respectively, L

p pressure , Pa

Pe dimensionless Peclet number, $Pe = Ul/D_m$

q Darcy velocity (filter/seepage velocity, discharge per unit area), L/T

Re dimensionless Reynolds number, expressed as $\overline{U}l// v$

Sh Sherwood number, $Sh = Kl/D_m$

t time, T

U fluid velocity vector or interstitial flow velocity, L/T

$\overline{U}$ average groundwater flow velocity, L/T

$\overline{U_c}$ average flow velocity in conduit, L/T

U_B slip velocity at the interface, L/T

x, y, z spatial coordinates in the longitudinal, transverse horizontal, and transverse vertical directions, respectively, L

Greek letters

α_L, α_{TH} , α_{TV} longitudinal, transverse horizontal, and transverse vertical dispersivities, respectively, L

δ_s thickness of stagnant layer, L

δ boundary layer thickness at the water and porous medium interface under slip flow condition, L

μ dynamic viscosity of the fluid, M/L/T

$\tilde{\mu}$ effective viscosity, M/L/T

v kinetic viscosity, L^2/T, $v=\mu/\rho$

ρ fluid density, M/L^3

ε porosity of the porous media, dimensionless

$\alpha_{B\text{-}J}$ empirical slip coefficient of the Beavers and Joseph boundary condition

β geometric scaling factor, dimensionless

γ equals to $\alpha_{B-J}/\sqrt{k}$, 1/L

σ^2 variance (of tracer plume)

θ conduit angle degree

Abbreviation

DNAPLs Dense Non-aqueous Phase Liquids

BTC Breakthrough Curves

MTT Mean travel time

SWI Sediment and water interface

WDI Water and DNAPL interface

Chapter 1

DNAPLs in karst hydrogeological settings

1.1 GROUNDWATER CONTAMINATION BY DNAPL

Chlorinated solvents were first produced in the nineteenth century and since then have been widely used in many industries, such as electronics, instrument manufacturing, dry cleaning, photographic processing and printing (Pankow and Cherry, 1996). These organic liquids are referred to as "Dense Non-aqueous Phase Liquids" (DNAPLs) since they are immiscible with water and denser than water. Among the most widely used DNAPLs are carbon tetrachloride (CCl_4), 1,1,1-Trichloroethane (TCA), Trichloroethylene (TCE) and Tetrachloroethylene (PCE) (Westrick et al., 1984). Other DNAPLs include halogenated benzenes, polychlorinated biphenyls (PCBs), some pesticide, coal tar and creosote. Halogenated hydrocarbons are almost without exception significantly denser than water by more than 10% (Mackay et al., 1985). The chlorinated DNAPLs are of concerns as they are frequently found in groundwater and threaten human health due to their toxicity. Many of them are classified as carcinogenic substance.

DNAPLs have been disposed in many waste sites. Their high density and low viscosity make them very mobile. Once introduced to the subsurface by spills, leaks, or intentional disposal they can penetrate deep into the underground through gravitational motion. DANPLs will be trapped in the pore space at residual saturation (Held and Illangasekare, 1995a; Held and Illangasekare, 1995b), or accumulate on top of low permeability layers as pools (Christ et al., 2010; Kueper et al., 1993; Pearce et al., 1994; Whelan et al., 1994). The zone where DNAPL is present is usually denoted as source zone.

While DNAPL source zones are usually restricted to the area where DNAPLs were released, gaseous or dissolved molecules can migrate further contaminating an extended volume of the subsurface and eventually reach receptors such as pumping wells or rivers. Most chlorinated DNAPLs are highly volatile leading to extensive gas phase contamination (Wang et al., 2012; Yu et al., 2009). These vapors could then dissolve in infiltrating rainwater and reach groundwater. In the saturated zone, groundwater flow through DNAPL source zones leads to the formation of plumes of dissolved contaminants (Chapman and Parker, 2005; Chapman et al., 2007; Rivett et al., 2006). Although DNAPLs are hydrophobic, the solubility of chlorinated hydrocarbons is usually many orders of magnitude higher compared with drinking water standards. A relatively small amount of chlorinated DNAPL has the potential to contaminate groundwater over a significant area for decades.

Under aerobic conditions, highly chlorinated compounds are very stable and hence no attenuation due to biodegradation occurs. Under strongly reducing conditions, they can be degraded via reductive

dechlorination. Less chlorinated compounds (for example vinyl chloride) can also be oxidized to CO_2 (Becker and Seagren, 2009; Haest et al., 2012; Hood et al., 2008; Hunkeler et al., 1999; Sercu et al., 2013; Shepherd et al., 2006; Tsai et al., 2009).

1.2 DNAPLs IN KARST SETTINGS

Karst aquifers provide drinkable water for hundreds of millions of people, accounting for 25 % of the world's groundwater resources (Ford and Williams, 2007). Although there is an extensive and rapidly growing literature on contaminants in porous media and fractured aquifers, the investigation of contaminant transport in karst aquifers is just at the beginning (Herman et al., 2012; Uhlman and Barner, 1998; Vesper et al., 2001). Transport mechanisms of heavy metals, LNAPLs and DNAPLs in karst aquifers have been recognized as open questions that need to been properly framed (White, 2002). DNAPLs can migrate to considerable depth in karst aquifers due to the presence of large subsurface openings. Once chlorinated DNAPLs intrude and accumulate in a karst aquifer, they will become a contamination source for decades or longer. Due to the complex networks of preferential pathways in karst aquifers, through which DNAPLs might migrate, it is difficult to locate and remediate karst aquifers contaminated by DNAPLs. In the following, important characteristics of karst aquifers that influence DNAPL migration are discussed. Studies on DNAPLs in karst settings are reviewed and finally a conceptual model of the DNAPL fate in karst aquifers is provided.

1.2.1 Characteristics of karst aquifer

Karst aquifers form in soluble rocks such as limestone and dolomite, and are characterized by voids of varied sizes and different flow regimes. Karst aquifers comprise three types of voids, which cause the permeability to span over many orders of magnitude. The primary porosity (referred as matrix porosity) is created during the deposition of rock, ranging from less than 1% (Bailly-Comte et al., 2010) to 30–50% (Martin et al., 2006; Renken et al., 2008). The secondary porosity are fractures (or fissures) arising from rock folding and faults. Conduits are considered to be the tertiary porosity created by dissolution and circulation of groundwater through fractures, with diameter from 5–16 mm (Howard, 1964) to tens of meters. Soluble rock with small primary porosity usually hosts strongly developed karst conduit networks, while those of higher original porosity tend to have poorly developed karst features (Ford and Williams, 2007).

Flow within the aquifer is divided into two modes, turbulent conduit flow and diffuse Darcian flow in fine fractures or the matrix (Atkinson, 1977). Although karst rocks may have primary porosity and secondary fracture porosity, most water is transmitted by conduits (tertiary porosity) developed by dissolution. A significant conduit flow component and associated turbulent flow is a distinct feature of karst. Non-Darcian behavior occurs in conduits when apertures exceed about 1 cm (Howard and Groves, 1995; White, 2002). Therefore, in karst aquifers, the range of conditions under which Darcy's law can be considered valid is very restricted (Mangin, 1975).

1.2.2 Site investigations of DNAPLs in karst aquifer

There have been some investigations of spill, dump and superfund sites which all demonstrate clearly the rapid movement and deep storage of DNAPLs in karst aquifer. Crawford and Ulmer (1994) investigated the movement of chloroform and TCE as DNAPL and dissolved phase at train derailment site near Lewisburg, Tennessee. Large quantities of chloroform-contaminated groundwater were pumped from a recovery well drilled into a sediment-filled cave. Their investigations also demonstrated that DNAPLs (TCE and chloroform) were likely to find their way through lower permeability material via fractures or interconnecting features and got into a confined aquifer. Jancin and Ebaugh (2002) studied the migration of DNAPL in a karst area with a thick overburden consisting of loess and alluvial sediments on top of the bedrock surface in southwestern Kentucky. Although the clay-filled depressions on the bedrock surface acted as barriers to downdip migration in the uppermost bedrock, permeable sands filled in deep top of bedrock lows and large solution fractures allowed DNAPL migration across bedrock layering. DNAPL that had penetrated through the overburden mainly migrated along slightly dipping bedding planes in the limestone formation.

Other field studies focus on the response of dissolved compounds from DNAPLs to hydrological events. Han and Wang (2004) studied the temporal and spatial evolution of carbon tetrachloride occurring in karst groundwater from a pesticide manufacturer. During a storm event, concentrations of the dissolved compounds were found to increase near the source zone while decrease in the discharge zone due to a dilution effect. In another field study of organic contaminants in karst aquifer (Mahler and Massei, 2007), peak concentration of PCE (Perchloroethylene) and Atrazine occurred simultaneously during storm events although they likely originated from different sources. PCE likely originated from point source contamination while atrazine originated from a diffuse input. The similar concentration patterns suggest a possible common storage place between the input zone and spring outlet. Both studies show that contamination of DNAPLs at springs has a direct relationship with recharge events. However, identification of DNAPL source zones and implementation of remediation is challenging in karst aquifer.

1.2.3 Conceptual model and DNAPL behavior in karst aquifers

Based on field studies, a conceptual model of DNAPL behaviors in karst settings has been proposed by Wolfe et al. (1997) as illustrated in Fig.1.1. The main injection points that DNAPLs enter into karst subsurface are sinking streams, sinkholes, and diffuse input through regolith and rock interface. The processes that control DNAPL behaviors in subsurface are summarized in Fig.1.2. Pooled and residual DNAPL can occur in both the vadose and ground-water zone. DNAPL source zones deplete through mass transfer to other phases by volatilization, dissolution and matrix diffusion. Therein, the dissolved-phase plume acts as an intermediate in transfer processes among phases. In terms of karst aquifers, the occurrence and fate of DNAPL in the subsurface exhibit their own characteristics in addition to the similar cases occurring in granular aquifer.

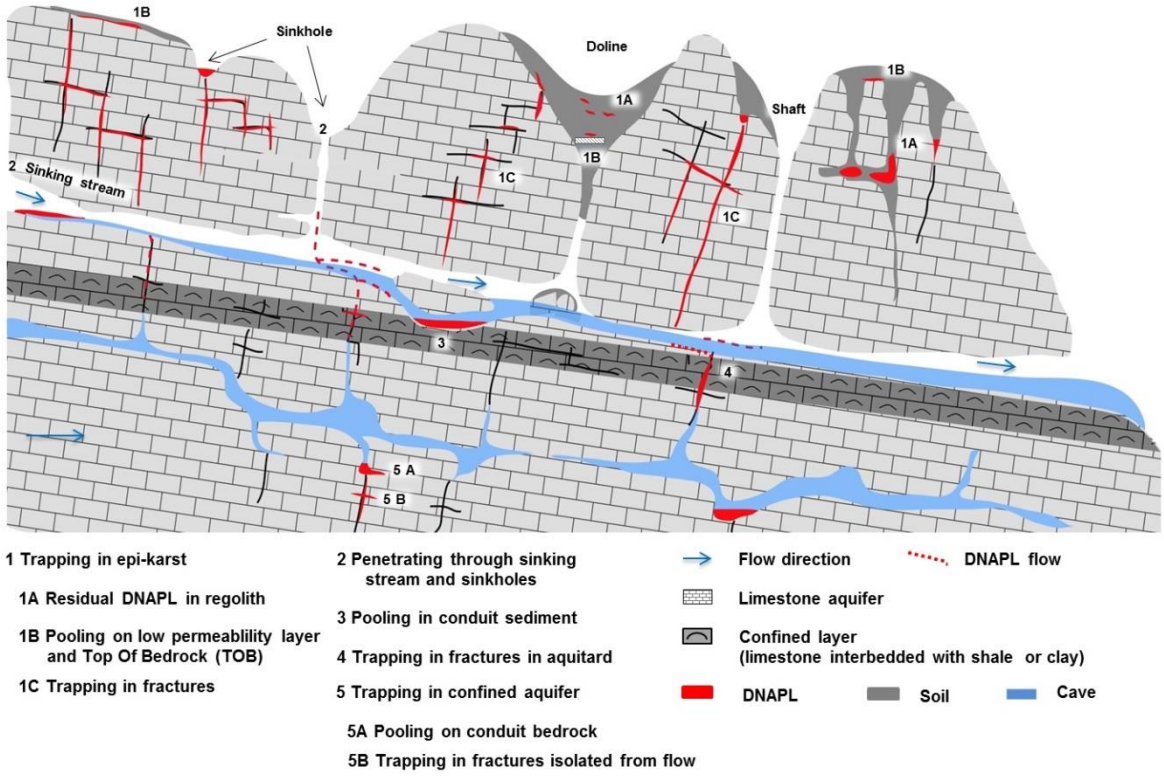

Fig.1.1 Distribution of potential DNAPL-accumulation sites in a hypothetical karst spring, case 3 is the targeted scenario of the thesis (Modified based on Wolfe 1997)

The accumulation of DNAPLs in karst aquifer can occur at three main locations, the epikarst zone, the active conduit system and deep phreatic zone as Loop and White (2001) generalized. The epikarst zone is characterized by the secondary voids ranging from fractures (millimeters to centimeters) to open shafts (meters to tens of meters), and the irregular regolith/bedrock interface. DNAPLs might become trapped (Hofstee et al., 1997; Hofstee et al., 1998; Kueper et al., 1993; Zhang and Smith, 2001) at residual saturation in soil, as pools on top of low permeability layers, e.g., clay or impermeable limestone (Fig.1.1 Case 1B), or within fractures. Depending on the degree of fracturation, vertical pathways in the vadose zone are, however, not always directed to draining conduits. They are often offset along bedding planes and deflected by lithologic and structural barriers, and intercepted by dry caves. DNAPLs could become trapped in these voids with less chance to access active flowpath (Fig.1.1 Case 1A). For DNAPL trapped in the epikarst, volatilization in vadose zone and dissolution in saturated zone are the dominant removal processes. These processes have been investigated so far for granular porous media but not for epikarst settings (Anderson et al., 1992a; Anderson et al., 1992b; Chrysikopoulos et al., 2000; Dela Barre et al., 2002; Imhoff et al., 1998; Lee and Chrysikopoulos, 2002; Miller et al., 1990; Rivett and Feenstra, 2005; Rivett et al., 2001; Schwille, 1988).

DNAPLs could enter into the active conduit system through sinkholes which are usually connected directly to phreatic conduits with rapid flow. DNAPLs can penetrate through sinkholes via three different ways: by direct infiltration through sinking streams (Fig.1.1 Case 2), by slow infiltration through soil plugging sinkholes, or by contaminated soil falling into conduits. The direct connection between sinkholes and conduit system allows contaminants to travel rapidly to springs

(Loop and White, 2001). DNAPLs could intrude into the sediment pile in conduits, become entrapped as residue or form pools at the base of the sediment pile. The pore space distribution within the clastic sediments in conduits, and their hydraulic connection with conduit flow are important factors for the dissolution and transport of DNAPL components.

DNAPLs could further move into any available porosity below the local base level and be trapped in the deep portion of the aquifer. Compared with the active conduit flow circulation above, the flow rates are low in the deeper bedrock and DNAPLs can remain in storage for long periods of time (Fig.1.1 Case 5B).

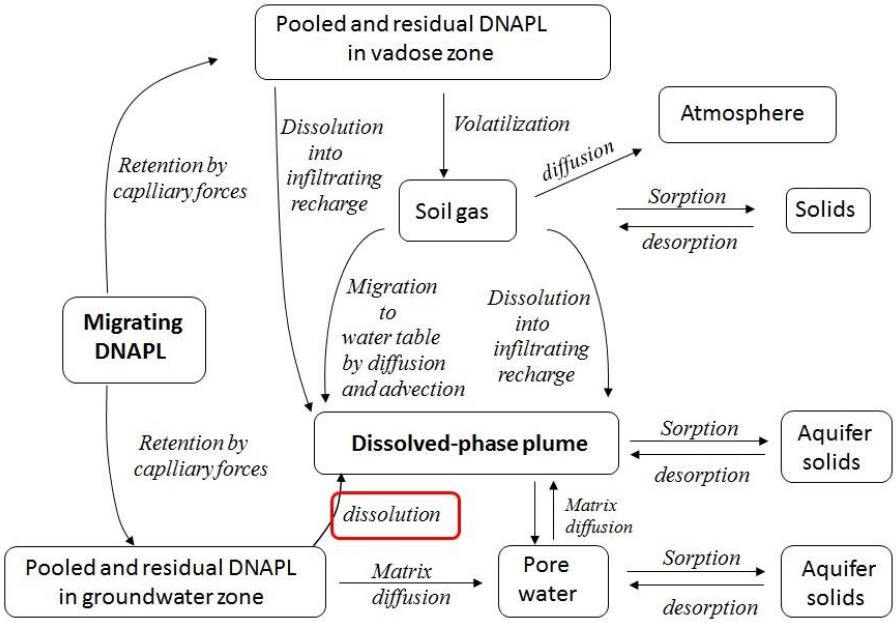

Fig.1.2 Processes controlling DNAPL distribution and fate in the subsurface (by Wolfe 1997), the process to be studied in our work is highlighted with red frame

From these possible DNAPL locations presented above, DNAPLs present in conduits in the phreatic zone likely lead to the highest levels of dissolved contaminants at springs since most water transits through these zones. In addition, DNAPLs in conduit sediment may be transported on suspended sediment or with entrained bulk sediment. During low and moderate flow condition when sediments are stable, dissolution will be the dominant process for DNAPL depletion, especially in water-filled conduit, which is the targeted process of this study.

While the processes that control the rate of DNAPL dissolution in fractured rock and unconsolidated sediments have been investigated in detail (Dickson and Thomson, 2003; Kueper and McWhorter, 1991; McLaren et al., 2012; O'Hara et al., 2000; Schaefer et al., 2009; Yang et al., 2012), dissolution of DNAPL in karst aquifers has received little attention so far. Hence, the study will focus on the dissolution of DNAPL in a conduit and sediment system. As a basis for these studies, common morphological features of karst conduits and factors that control the flow and sediment distribution in conduits will be reviewed.

1.2.4 Morphology of karst conduits, flow processes and sediment distribution

The conduit morphology is strongly influenced by the paths that guided the original dissolution of the bedrock. The axes and geometry of conduits can be influenced by the fold pattern by tectonic movement. Investigation of cave systems indicates the frequent occurrence of water-filled phreatic loops in cave system (Fig.1.3). Such structures have for example been detected in the Hölloch, Switzerland, Swildon's hole II-XII, England (Ford and Ewers, 1978) and the Krupaja siphon spring channel (Milanovic, 2007). At the loop bases clastic debris is often deposited, limiting the access to cave passage. Vertical amplitude of looping varies in different systems from <15 m to several hundred meters, depending on the dipping of strata and the dimensions of fractures. The looping structure is likely enhanced by the higher dissolution rate at sinkholes and draining springs, and the lower dissolution rate at the connecting passages (Dreybrodt, 1990; Groves and Howard, 1994b; White, 1977), leading to the siphon forms commonly encountered in caves.

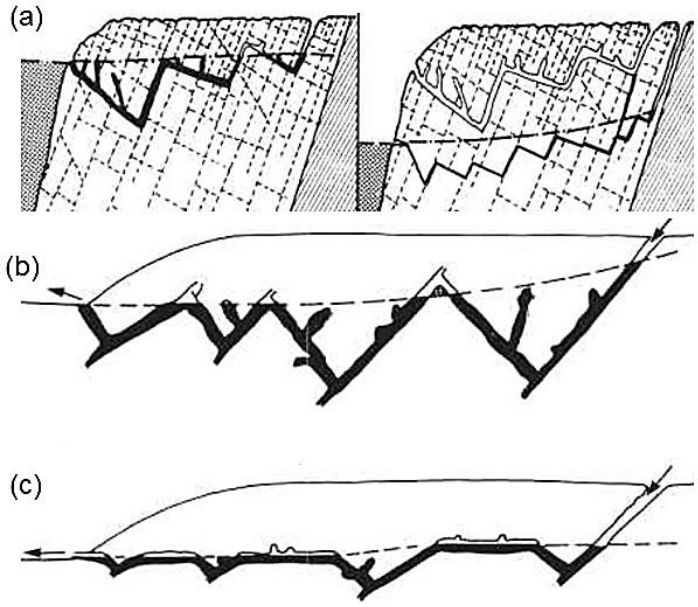

Fig.1.3 Illustration on (a) successive phreatic loops developed in massive of limestone; (b) (c)deep phreatic cave with multiple loops, hypothesized by Ford and Ewers (1977)

Flow processes in karst aquifer can be highly variable. Depending on the hydraulic gradients and conduit diameters, flow in conduit may be fast turbulent or laminar flow (early stage of cave development (Groves and Howard, 1994a). Flow could be continuous or discontinuous controlled by conduit morphological features. Water level in conduit stream changes with recharge condition. Flow in conduits may function as free-surface open channel flow or full pressurized pipe flow. Water-filled portion of the conduits may descend to sumps and then rise again to open channels. Conduit velocities range from cm/s to m/s (Worthington and Ford, 2009). They are usually many orders of magnitude faster than groundwater velocities of m/d in granular or fractured porous media. Open channel flow in karst systems is not intrinsically different from open channel flow in surface streams. Conduits show similar type of deposits as in surface streams with meandering channels, point bars, and other features (Herman et al., 2012).

The conduit systems are very rich in clastic sediments (Herman et al., 2012; Schroeder and Ford, 1983). Only recently the role of clastic sediment has been demonstrated as an intrinsic part of karst hydrologic systems and also as an important mechanism of contaminant transport (Herman et al., 2012; Herman et al., 2008). Clastic sediments include allochthonous sediments carried by sinking streams or by soil washdown from the epikarst, and autochthonous sediments such as breakdown and residual insoluble material from the dissolution of limestone, e.g., chert nodules. Increased paved areas with urbanization dramatically increase water and sediment entering conduit system through sinkholes. The conduit system acts as a mixing chamber where the injected materials are sorted and rearranged. The clastic sediments are usually thought to form a more permeable medium encapsulated by the relatively impermeable limestone wall of the conduit (Loop and White, 2001).

The sequence of cave sediments records the history of conduit hydrology. Deposition of sediments with varied grain size is an indicator of the conduit flow capacity. Clastic sediments in karst aquifers fall into roughly three size classes, clay, silt and fine sand (few micrometers to 0.2 mm); sands, gravels, and small cobbles (0.5–100 mm); boulders (>200 mm). The middle range grains are most easily mobilized and are most frequently studied in flume tests. Many conduits undulate in the vertical plane with downloops and up-loops (Ford and Ewers, 1978). The downloops act as sediment traps (Fig. 1.4). The trapped sediment protects the floor and lower walls of the conduit from dissolution by the flowing water. High heads developed during flood flows may flush sediments out of conduits. During moderate to low flows the clastic material may deposit back and again block the passage.

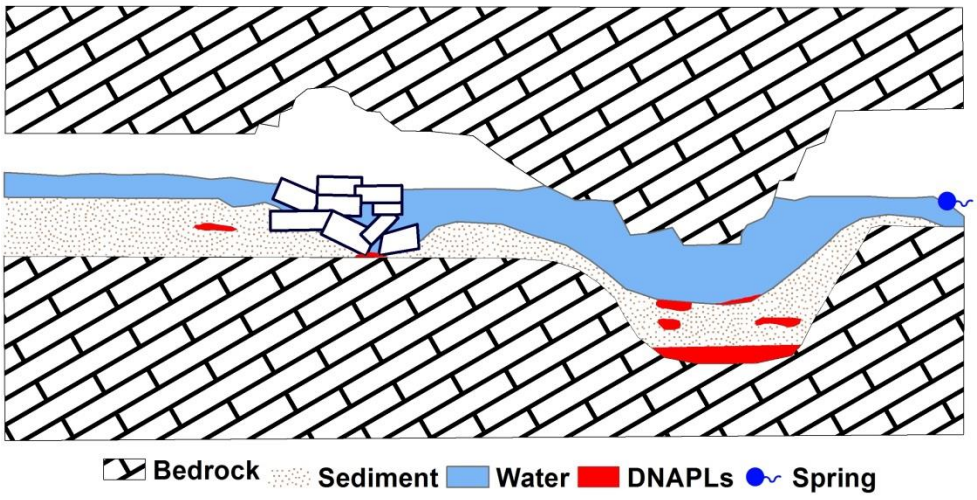

Fig. 1.4 Segment of conduit showing undulating profile with contaminant trapping sites (Loop and White 2001)

As the natural karst systems are quite complicated and there are barely any sites where DNAPLs have been located and accessible for study, this study will rely on a laboratory analog resembling karst conduit with sediments. In the following, previous applications of laboratory analog models in karst research will be reviewed.

1.3 ANALOG MODELS IN KARST SETTINGS

For karst studies, two types of analog can be distinguished: One is the single medium analog, which contains either limestone porous media, or an individual conduits feature; the other type is the dual-medium analog consisting of a conduits with surrounding matrix, which better represents the duality of karst aquifer.

The first type of analog is commonly used to study the reactive transport of solutes in limestone media. Curk (1997) studied the retardation of tracer Uranine to limestone samples in a column filled with crushed rock. Tracer tests showed negligible retardation with constant inflow of high concentration (1µg/l) Uranine at high flow. However, retardation became perceptible at low flow due to the increased residence time and matrix diffusion. Transport and sorption of microsphere and pathogen were investigated using intact limestone cores (Harvey et al., 2008; Renken et al., 2008; Renken et al., 2005; Shapiro et al., 2008). The tracer tests showed that preferential flow paths have a stronger influence on the transport of colloids than of nonreactive tracer. In addition, the high matrix porosity of limestone was effective in removing oocyst-sized microspheres. Hauns (1999) investigated the effect of pools in karst conduits on the dispersion of solutes (Hauns, 1999; Hauns et al., 2001a; Hauns et al., 2001b). Laboratory tracer tests showed evident tailing related to the presence of the pool. Dispersion was decreasing with increasing flow rate. In contrary, dispersion was found to increase with flow rate from field tracer tests performed in a cave pool stream. Additionally, numerical simulations of flow and solute transport in channels of different shapes by Computational Fluid Dynamics (CFD) showed the highest dispersion for angular channels. Single feature analogs provide a simplified way for laboratory experiments similarly to column experiments with granular porous media. They, however, do not represent some key features of karst aquifers such as the duality of flow.

The second type of analogs is constructed more closely based on the conceptual model of dual flow in karst aquifers. The sequestration of solutes from conduits into the matrix was investigated using an apparatus consisting of a cylinder pipe enclosed by a chamber packed with glass beads (Li, 2011; Li, 2012; Li and Loper, 2011; Li et al., 2008; Li et al., 2010). Sequestration was classified into two extremes: active sequestration by advection due to significant pressure difference between conduit and matrix during high flow regime (flooding seasons); and passive sequestration, characterized by shear-flow induced for instance by the wavy bedform configuration with no significant pressure difference between the two domains under low flows (ordinary hydrological seasons). Small-scale pressure variation (shear-flow sequestration) at the conduit-matrix boundary was sufficient to transfer solutes and nutrients to a sublayer of porous media adjacent to the conduits where bacteria may thrive. This zone was termed as hyporheic zone (Li et al., 2012). Another research group investigated conduit-matrix exchange processes by using a rectangular conduit overlain by a porous media made of glass beads (Faulkner et al., 2009; Hu, 2010). The experiments of Hu showed visually the intruded tracer plume from conduit to the matrix through the transparent plexiglas wall. Both the studies from Li et al and Hu et al showed the significance of flow exchange between conduit and matrix on the

solute transport in karst aquifers. Hydraulic head in each domain was controlled independently in both the two analogs. The matrix simulated in both the analogs was very permeable, which was not representative for limestone with low primary porosity and permeability. Different concepts were used to describe the conduits-matrix coupling in numerical models. Li et al. adopted a no-slip boundary condition, whereas, Hu et al. used a Beaver-Joseph interfacial boundary to couple the two domains. The different concepts used to represent the interfacial boundary will be further discussed in the section of modeling approach in Chapter 2.

1.4 STUDY PURPOSE AND APPROACH

While several studies have proposed the conceptual models of DNAPL behaviors in karst as reviewed above, the postulated processes have not been investigated experimentally so far. This thesis focuses on the fate of DNAPLs trapped in sediments present in karst conduits. As most of the flow transits through conduits such zones might be a particularly important source of dissolved compounds. The main aim is to gain a better understanding of the processes that control the rate of DNAPL dissolution and hence the longevity of a sediment-buried DNAPL source zone in conduits. The flow rate in the sediment at the water/DNAPL interface is a key factor that controls mass transfer of DNAPL compounds to the dissolved phase. Hence, the quantification of DNAPL dissolution requires a good understanding of hyporheric exchange processes between the conduit and sediment domain. Therefore, the first part of this PhD was dedicated to conduit-sediment exchange processes before investigating the dissolution of sediment-entrapped DNAPL pools. The role of conduit flow rate, sediment properties and conduit geometry on hyporheic flow and dissolution process will be investigated. Laboratory analogs have been demonstrated to be useful in understanding conduit-matrix exchange processes, and hence such an approach was adopted in this study. Tracer tests and numerical simulations for characterizing flow and solute transport processes were applied throughout the thesis. The objectives and research approaches of each chapter are summarized below.

Chapter 2: First, the two key processes – hyporheic exchange and DNAPL pool dissolution were reviewed and discussed before further exploring the specific issues when applying these concepts to karst conduit and sediment system. The driving forces that induce hyporheic exchange in surface water and biogeochemical implications of hyporheic flow were presented. The potential karst hyporheic flow was discussed based on indications from some field studies. Then, the conceptual model of pool dissolution and methods to quantify the mass transfer rate were summarized. Finally, for applying an appropriate mathematical approximation of flow and transport processes in the conduit and sediment system, different governing equations and boundary conditions for modeling flow in the dual domains were compared.

Chapter 3: To investigate hyporheic flow processes in the conduit-sediment system, a laboratory analog resembling a siphon partly filled with sediment was built. Two systems with different conduit angles accounting for hydraulic effect from geological dipping were set up to study the influence of

conduit angle on flow and transport processes. Flow regimes and dispersive property in conduit were defined by in-conduit tracer tests. Sediment-source tracer tests were used to characterize hyporheic flow patterns in the sediment domain, and to investigate the influence of conduit flow condition (parameterized by Reynolds number *Re*) and conduit angle on solute transport. The driving force and magnitude of hyporheic flow in the conduit and sediment system were investigated by analyzing pressure and flow fields by numerical simulation. The mathematical model in representing flow motion and solute transport processes was evaluated by comparing the simulated BTCs with that from tracer tests. Finally, by calculation from numerical model, the relationship between the overall exchange flux q_{int} and conduit *Re* was established.

Chapter 4: Furthermore, the role of sediment properties on hyporheic exchange between conduit and sediment was investigated in addition to the effect of conduit flow rate and conduit angle. The same sediment-source tracer tests and numerical simulations were conducted as in Chapter 3 for sediments of variable grain sizes. The relative roles of different controlling factors on the hyporheic flow pattern and magnitude of exchange flux were evaluated based on the numerical simulations of flow fields and the overall exchange flux q_{int}.

Chapter 5: With the solid understanding of hyporheic flow in conduit-sediment systems, a well-defined DNAPL pool with surrogate compound was created at the bottom of the sediment to study influences of conduit flow and angle on the mass transfer rate of DNAPL compounds to the dissolved phase. Mass transfer coefficients k_m were quantified and relationship between k_m and conduit *Re* was established. As the dissolved plume was invisible, a solidified pool of soluble tracer was created to track the transport of the solute plume originating from the DNAPL pool surface. To highlight differences in the dissolution processes between a conduit-sediment system and a classical porous media, k_m predicated by a 2D model for a semi-infinite porous media was compared with the observed and simulated values. The mass transfer rate in karst conduit sediment and semi-infinite porous medium was further compared and discussed.

Chapter 6: The last chapter is summary and conclusions of the whole thesis, includes also some discussion of limitations of the study and outlook of the future work.

1.5 REFERENCE

Anderson, M.R., Johnson, R.L., Pankow, J.F., 1992a. Dissolution of dense chlorinated solvents into ground-water .1. Dissolution from a well-defined residual source. Ground Water, 30(2): 250-256.

Anderson, M.R., Johnson, R.L., Pankow, J.F., 1992b. Dissolution of dense chlorinated solvents into groundwater .3. Modeling contaminant plumes from fingers and pools of solvent. Environmental Science & Technology, 26(5): 901-908.

Atkinson, T.C., 1977. Diffuse flow and conduit flow in limestone terrain in mendip hills, somerset (great-britain). Journal of Hydrology, 35(1-2): 93-110.

Bailly-Comte, V. et al., 2010. Water exchange and pressure transfer between conduits and matrix and their influence on hydrodynamics of two karst aquifers with sinking streams. Journal of Hydrology, 386(1-4): 55-66.

Becker, J.G., Seagren, E.A., 2009. Modeling the effects of microbial competition and hydrodynamics on the dissolution and detoxification of dense nonaqueous phase liquid contaminants. Environmental Science & Technology, 43(3): 870-877.

Chapman, S.W., Parker, B.L., 2005. Plume persistence due to aquitard back diffusion following dense nonaqueous phase liquid source removal or isolation. Water Resources Research, 41(12).

Chapman, S.W., Parker, B.L., Cherry, J.A., Aravena, R., Hunkeler, D., 2007. Groundwater-surface water interaction and its role on TCE groundwater plume attenuation. Journal of Contaminant Hydrology, 91(3-4): 203-232.

Christ, J.A., Ramsburg, C.A., Pennell, K.D., Abriola, L.M., 2010. Predicting DNAPL mass discharge from pool-dominated source zones. Journal of Contaminant Hydrology, 114(1-4): 18-34.

Chrysikopoulos, C.V., Lee, K.Y., Harmon, T.C., 2000. Dissolution of a well-defined trichloroethylene pool in saturated porous media: Experimental design and aquifer characterization. Water Resources Research, 36(7): 1687-1696.

Crawford, N.C., Ulmer, C.S., 1994. Hydrogeologic investigations of contaminant movement in karst aquifers in the vicinity of a train derailment near lewisburg, tennessee. Environmental Geology, 23(1): 41-52.

Curk, B.C., 1997. Laboratory tracer experiment in carbonate porous media from Slovenia. Tracer Hydrology: 19-26.

Dela Barre, B.K., Harmon, T.C., Chrysikopoulos, C.V., 2002. Measuring and modeling the dissolution of nonideally shaped dense nonaqueous phase liquid pools in saturated porous media. Water Resources Research, 38(8).

Dickson, S.E., Thomson, N.R., 2003. Dissolution of entrapped DNAPLs in variable aperture fractures: Experimental data and empirical model. Environmental Science & Technology, 37(18): 4128-4137.

Dreybrodt, W., 1990. The role of dissolution kinetics in the development of karst aquifers in limestone - a model simulation of karst evolution. Journal of Geology, 98(5): 639-655.

Faulkner, J., Hu, B.X., Kish, S., Hua, F., 2009. Laboratory analog and numerical study of groundwater flow and solute transport in a karst aquifer with conduit and matrix domains. Journal of Contaminant Hydrology, 110(1-2): 34-44.

Ford, D., Williams, P., 2007. Karst hydrologeology and geomorphology. Wiley, England.

Ford, D.C., Ewers, R.O., 1978. Development of limestone cave systems in dimensions of length and depth. Canadian Journal of Earth Sciences, 15(11): 1783-1798.

Groves, C.G., Howard, A.D., 1994a. Early development of karst systems .1. Preferential flow path enlargement under laminar-flow. Water Resources Research, 30(10): 2837-2846.

Groves, C.G., Howard, A.D., 1994b. Minimum hydrochemical conditions allowing limestone cave development. Water Resources Research, 30(3): 607-615.

Haest, P.J., Springael, D., Seuntjens, P., Smolders, E., 2012. Self-inhibition can limit biologically enhanced TCE dissolution from a TCE DNAPL. Chemosphere, 89(11): 1369-1375.

Han, B.P., Wang, X.Y., 2004. Groundwater contamination by carbon tetrachloride in Karstic area in China. Acta Scientiae Circumstantiae (In Chinese), 24(6): 982-988.

Harvey, R.W. et al., 2008. Pathogen and chemical transport in the karst limestone of the Biscayne aquifer: 3. Use of microspheres to estimate the transport potential of Cryptosporidium parvum oocysts. Water Resources Research, 44(8).

Hauns, M., 1999. Modeling tracer and particle transport in karst conduit structures, PhD thesis, Neuchâtel University, Neuchâtel.

Hauns, M., Atteia, O., Leibundgut, C., 2001a. Colloid transport in karst conduits: a CFD-based model. New Approaches Characterizing Groundwater Flow, Vols 1 and 2, 99-102 pp.

Hauns, M., Jeannin, P.Y., Atteia, O., 2001b. Dispersion, retardation and scale effect in tracer breakthrough curves in karst conduits. Journal of Hydrology, 241(3-4): 177-193.

Held, R.J., Illangasekare, T.H., 1995a. Fingering of dense nonaqueous phase liquids in porous-media .1. Experimental investigation. Water Resources Research, 31(5): 1213-1222.

Held, R.J., Illangasekare, T.H., 1995b. Fingering of dense nonaqueous phase liquids in porous-media .2. Analysis and classification. Water Resources Research, 31(5): 1223-1231.

Herman, E., Toran, L., White, W., 2012. Clastic sediment transport and storage in fluviokarst aquifers: an essential component of karst hydrogeology. Carbonates and Evaporites, 27(3-4): 211-241.

Herman, E.K., Toran, L., White, W.B., 2008. Threshold events in spring discharge: Evidence from sediment and continuous water level measurement. Journal of Hydrology, 351(1-2): 98-106.

Hofstee, C., Dane, J.H., Hill, W.E., 1997. Three-fluid retention in porous media involving water, PCE and air. Journal of Contaminant Hydrology, 25(3-4): 235-247.

Hofstee, C., Oostrom, M., Dane, J.H., Walker, R.C., 1998. Infiltration and redistribution of perchloroethylene in partially saturated, stratified porous media. Journal of Contaminant Hydrology, 34(4): 293-313.

Hood, E.D. et al., 2008. Demonstration of enhanced bioremediation in a TCE source area at Launch Complex 34, Cape Canaveral Air Force Station. Ground Water Monit. Remediat., 28(2): 98-107.

Howard, A.D., 1964. Process of limestone cavern development. International Journal of Speleology, 1: 47-60.

Howard, A.D., Groves, C.G., 1995. Early development of karst systems .2. Turbulent-flow. Water Resources Research, 31(1): 19-26.

Hu, B.X., 2010. Examining a coupled continuum pipe-flow model for groundwater flow and solute transport in a karst aquifer. Acta Carsologica, 39(2): 347-359.

Hunkeler, D., Aravena, R., Butler, B.J., 1999. Monitoring microbial dechlorination of tetrachloroethene (PCE) in groundwater using compound-specific stable carbon isotope ratios: Microcosm and field studies. Environmental Science & Technology, 33(16): 2733-2738.

Imhoff, P.T., Arthur, M.H., Miller, C.T., 1998. Complete dissolution of trichloroethylene in saturated porous media. Environmental Science & Technology, 32(16): 2417-2424.

Jancin, M., Ebaugh, W.F., 2002. Shallow lateral DNAPL migration within slightly dipping limestone, southwestern Kentucky. Engineering Geology, 65(2-3): 141-149.

Kueper, B.H., McWhorter, D.B., 1991. The behavior of dense, nonaqueous phase liquids in fractured clay and rock. Ground Water, 29(5): 716-728.

Kueper, B.H., Redman, D., Starr, R.C., Reitsma, S., Mah, M., 1993. A field experiment to study the behavior of tetrachloroethylene below the water-table - spatial-distribution of residual and pooled dnapL. Ground Water, 31(5): 756-766.

Lee, K.Y., Chrysikopoulos, C.V., 2002. Dissolution of a well-defined trichloroethylene pool in saturated porous media: experimental results and model simulations. Water Research, 36(15): 3911-3918.

Li, G., 2011. Spatially varying dispersion to model breakthrough curves. Ground Water, 49(4): 584-592.

Li, G., 2012. Calculation of karst conduit flow using dye tracing experiments. Transport in Porous Media, 95(3): 551-562.

Li, G., Cheng, Y., Zhao, B., 2012. Analysis of the effect of the beavers-joseph interface condition on flow in karst conduits. Journal of the American Water Resources Association, 48(6): 1233-1240.

Li, G., Loper, D.E., 2011. Transport, dilution, and dispersion of contaminant in a leaky karst conduit. Transport in Porous Media, 88(1): 31-43.

Li, G., Loper, D.E., Kung, R., 2008. Contaminant sequestration in karstic aquifers: Experiments and quantification. Water Resources Research, 44(2).

Li, G., Shang, Y., Gao, J., 2010. Scale analysis of the significance of dispersion in mixing-transport in conduits. Journal of Cave and Karst Studies, 72(3): 150-155.

Loop, C.M., White, W.B., 2001. A conceptual model for DNAPL transport in karst ground water basins. Ground Water, 39(1): 119-127.

Mackay, D.M., Roberts, P.V., Cherry, J.A., 1985. Transport of organic contaminants in groundwater. Environmental Science & Technology, 19(5): 384-392.

Mahler, B., Massei, N., 2007. Anthropogenic contaminants as tracers in an urbanizing karst aquifer. Journal of Contaminant Hydrology, 91(1-2): 81-106.

Mangin, A., 1975. Contribution a l'etude hydrodynamique des aquiferes karstiques., Univ. Dijon . Laboratoire souterrain du C.N.R.S., 261 pp.

Martin, J.M., Screaton, E.J., Martin, J.B., 2006. Monitoring well responses to karst conduit head fluctuations: Implications for fluid exchange and matrix transmissivity in the Floridan aquifer. In: Harmon, R.S., Wicks, C.M. (Eds.), Perspectives on Karst Geomorphology, Hydrology, and Geochemistry. Geological Society of America Special Papers, pp. 209-217.

McLaren, R.G., Sudicky, E.A., Park, Y.J., Illman, W.A., 2012. Numerical simulation of DNAPL emissions and remediation in a fractured dolomitic aquifer. Journal of Contaminant Hydrology, 136: 56-71.

Milanovic, S., 2007. Hydrogeological characteristics of some deep siphonal springs in Serbia and Montenegro karst. Environmental Geology, 51(5): 755-759.

Miller, C.T., Poiriermcneill, M.M., Mayer, A.S., 1990. Dissolution of trapped nonaqueous phase liquids - mass-transfer characteristics. Water Resources Research, 26(11): 2783-2796.

O'Hara, S.K., Parker, B.L., Jorgensen, P.R., Cherry, J.A., 2000. Trichloroethene DNAPL flow and mass distribution in naturally fractured clay: Evidence of aperture variability. Water Resources Research, 36(1): 135-147.

Pankow, J.F., Cherry, J.A., 1996. Dense chlorinated solvents and other DNAPL's in groundwater. Waterloo Press, Portland, Oregon.

Pearce, A.E., Voudrias, E.A., Whelan, M.P., 1994. Dissolution of TCE and TCA pools in saturated subsurface systems. Journal of Environmental Engineering-Asce, 120(5): 1191-1206.

Renken, R.A. et al., 2008. Pathogen and chemical transport in the karst limestone of the Biscayne aquifer: 1. Revised conceptualization of groundwater flow. Water Resources Research, 44(8).

Renken, R.A. et al., 2005. Assessing the vulnerability of a municipal well field to contamination in a karst aquifer. Environmental & Engineering Geoscience, 11(4): 319-331.

Rivett, M.O., Chapman, S.W., Allen-King, R.M., Feenstra, S., Cherry, J.A., 2006. Pump-and-treat remediation of chlorinated solvent contamination at a controlled field-experiment site. Environmental Science & Technology, 40(21): 6770-6781.

Rivett, M.O., Feenstra, S., 2005. Dissolution of an emplaced source of DNAPL in a natural aquifer setting. Environmental Science & Technology, 39(2): 447-455.

Rivett, M.O., Feenstra, S., Cherry, J.A., 2001. A controlled field experiment on groundwater contamination by a multicomponent DNAPL: creation of the emplaced-source and overview of dissolved plume development. Journal of Contaminant Hydrology, 49(1-2): 111-149.

Schaefer, C.E., Callaghan, A.V., King, J.D., McCray, J.E., 2009. Dense nonaqueous phase liquid architecture and dissolution in discretely fractured sandstone blocks. Environmental Science & Technology, 43(6): 1877-1883.

Schroeder, J., Ford, D.C., 1983. Clastic sediments in castleguard cave, columbia icefields, alberta, canada. Arctic and Alpine Research, 15(4): 451-461.

Schwille, F., 1988. Dense chlorinated solvents in porous and fractured media - Model experiments. Lewis, Boca Raton, FL.

Sercu, B. et al., 2013. The influence of in situ chemical oxidation on microbial community composition in groundwater contaminated with chlorinated solvents. Microbial Ecology, 65(1): 39-49.

Shapiro, A.M., Renken, R.A., Harvey, R.W., Zygnerski, M.R., Metge, D.W., 2008. Pathogen and chemical transport in the karst limestone of the Biscayne aquifer: 2. Chemical retention from diffusion and slow advection. Water Resources Research, 44(8).

Shepherd, K.A., Ellis, P.A., Rivett, M.O., 2006. Integrated understanding of urban land, groundwater, baseflow and surface-water quality - The City of Birmingham, UK. Science of the Total Environment, 360(1-3): 180-195.

Tsai, T.T., Kao, C.M., Yeh, T.Y., Liang, S.H., Chien, H.Y., 2009. Application of surfactant enhanced permanganate oxidation and bidegradation of trichloroethylene in groundwater. Journal of Hazardous Materials, 161(1): 111-119.

Uhlman, K., Barner, W., 1998. Contaminant transport mechanisms in karst terranes. In: Johnson, I.A., FernandezJauregui, C.A. (Eds.), Hydrology in the Humid Tropic Environment. Iahs Publication. Int Assoc Hydrological Sciences, Wallingford, pp. 327-335.

Vesper, D., Loop, C.M., White, W.B., 2001. Contaminant transport in karst aquifers, Theoretical and applied karstology, pp. 101-111.

Wang, X., Unger, A.J.A., Parker, B.L., 2012. Simulating an exclusion zone for vapour intrusion of TCE from groundwater into indoor air. Journal of Contaminant Hydrology, 140: 124-138.

Westrick, J.J., Mello, J.W., Thomas, R.F., 1984. The groundwater supply survey. Journal American Water Works Association, 76(5): 52-59.

Whelan, M.P., Voudrias, E.A., Pearce, A., 1994. Dnapl pool dissolution in saturated porous-media - procedure development and preliminary-results. Journal of Contaminant Hydrology, 15(3): 223-237.

White, W.B., 1977. The role of solution kinetics in the development of karst aquifers. Mem.Int.Assoc.Hydrgeol., 12: 503-507.

White, W.B., 2002. Karst hydrology: recent developments and open questions. Engineering Geology, 65(2-3): 85-105.

Wolfe, W.J., Haugh, C.J., Webbers, A., Diehl, T.H., 1997. Preliminary conceptual models of the occurrence, fate, and transport of chlorinated solvents in karst regions of Tennessee. USGS Water-Resources Investigation Report 97-4097.

Worthington, S.R.H., Ford, D.C., 2009. Self-organized permeability in carbonate aquifers. Ground Water, 47(3): 326-336.

Yang, Z., Niemi, A., Fagerlund, F., Illangasekare, T., 2012. Effects of single-fracture aperture statistics on entrapment, dissolution and source depletion behavior of dense non-aqueous phase liquids. Journal of Contaminant Hydrology, 133: 1-16.

Yu, S., Unger, A.J.A., Parker, B., 2009. Simulating the fate and transport of TCE from groundwater to indoor air. Journal of Contaminant Hydrology, 107(3-4): 140-161.

Zhang, Z.F., Smith, J.E., 2001. The velocity of DNAPL fingering in water-saturated porous media: laboratory experiments and a mobile-immobile-zone model. Journal of Contaminant Hydrology, 49(3-4): 335-353.

Chapter 2

Relevant processes and mathematical description

The rate of DNAPL pool dissolution in karst conduit and sediment settings depends on two main factors: The intensity of water flow through the sediments and the mass transfer rate of molecules across the DNAPL/water interface. Each of these factors has received a lot of attention in previous studies but their interaction in conduit-sediment system has not yet been considered so far. Mass transfer across NAPL/water interfaces has extensively been studied for fully water-saturated porous media. Numerous studies on hyporheic flow have investigated the interaction between free flow in surface water and porous media flow in the underlying sediments. In the following, the main findings from these two fields are briefly reviewed, followed by a discussion of the mathematical methods to the coupled free flow and porous media flow.

2.1 DNAPL POOL DISSOLUTION

Understanding the dissolution process of DNAPL is of importance for site management and remediation. The rate of mass transfer from the DNAPL will influence the dissolved compound concentrations in groundwater as well as the lifetime of a DNAPL source zone (Pankow and Cherry, 1996). Numerous studies have investigated how the interphase mass flux varies as a function of the DNAPL architecture and groundwater flow conditions in unconsolidated granular media (Anderson et al., 1992a; Anderson et al., 1992b; Chrysikopoulos and Kim, 2000; Geller and Hunt, 1993; Hunt et al., 1988). The morphology of the DNAPL source zone, DNAPL solubility and interstitial velocity at the water/NAPL interface has been identified as important factors that control the dissolution process.

The entrapment architecture of DNAPLs strongly influences the processes of mass transfer (Fure et al., 2006; Page et al., 2007). A portion of the DNAPL may be trapped and immobilized as blobs or ganglia within the pore spaces, referred to as residual NAPL (Hunt et al., 1988). In addition, DNAPLs can accumulate as pools when encountering an impermeable layer while migrating downward (Chrysikopoulos et al., 1994).

During dissolution of both pools and residual NAPL, the flux to the aqueous phase proceeds via diffusion across the phase boundary. The total flux rate is dependent on the interfacial area between the NAPL and water-filled pores with active flow (Butcher and Gauthier, 1994). Of the two configurations, residual NAPL dissolution is expected to proceed at a faster rate, because of the larger

surface area available for interphase mass transfer (Schwille, 1988). NAPL pools tend to be aligned in groundwater flow direction hence limiting the contact with flowing groundwater (Anderson et al., 1992b). The rate of dissolution into groundwater flowing above a thin pool of chlorinated hydrocarbons (CHC) will also be controlled by the rate at which vertical dispersion can move the contaminant away from the water /DNAPL interface (WDI) and into the clean water above the pool (van der Waarden et al., 1971; van der Waarden et al., 1977). Hence DNAPL pool dissolution tends to have a strong influence on the lifetime of a DNAPL contamination and will be discussed in more detail.

2.1.1 Conceptual model of DNAPL pool dissolution

DNAPL pools typically only have a small height but are long, due to their accumulation on top of low permeability layers (Schwille, 1988). The shape of a dissolved plume above a DNAPL pool in uniform groundwater flow is illustrated in Fig. 2.1.

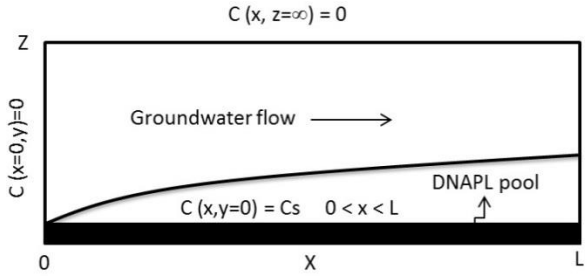

Fig. 2.1 Illustration of DNAPL pool dissolution experiment of Schwille (1998)

The dissolution rate is controlled by diffusion/transverse dispersion along the concentration gradients above the interface. If the concentration gradients are known, one can calculate the dissolution rate. For the dissolution of DNAPL pool of a regular geometry, an analytical equation of the concentration profile was derived which permits calculation of the dissolution rate (Bird et al., 1960; Hunt et al., 1988). The equation was derived based on the advection-dispersion equation in a steady-state form. Assuming that the pool is wide relative to the horizontal transverse mixing process, the dissolution process can be approximated in a two-dimensional vertical section. Neglecting horizontal dispersion which does not influence significantly the dissolution rate, the two-dimensional form of transport equation is (Johnson and Pankow, 1992):

$$\overline{U}\frac{\partial C}{\partial x} = D_{TV}\frac{\partial^2 C}{\partial z^2} \qquad \text{(Eq. 2.1)}$$

$$D_{TV} = D_e + \overline{U}\alpha_{TV} \qquad \text{(Eq. 2.2)}$$

Where $\overline{U}$ is the average flow velocity, C is the concentration, x is longitudinal coordinate, z is vertical coordinate, D_{TV} is the transverse vertical dispersion coefficient, D_e is the molecular diffusion coefficient, α_{TV} is the transverse vertical dispersivity. The vertical transverse dispersion in groundwater system is generally small. At low groundwater velocity (0.1 m/d), vertical dispersion is on the order of molecular diffusion (Sudicky, 1986).

For dissolution of a DNAPL pool into a semi-infinite porous media in vertical direction, an analytical solution was derived by Hunt et al. (1988). Assuming that the concentration is always at saturation at the interface, the following concentration profile at downgradient edge of the pool is obtained ($x = L_p$, L_p is pool length)

$$C(L_p, z) = C_s \, erfc\left(\frac{z}{2\left(\frac{D_{TV} L_p}{\overline{U}}\right)^{1/2}}\right) \qquad \text{(Eq. 2.3)}$$

For residual DNAPL, it is impossible to know the microscopic concentration gradient that control dissolution at the pore scale. Due to the lack of knowledge, the dissolution is characterized by the mass transfer coefficient k_m. It is not a fundamental physical property, but rather an effective parameter influenced by different factors. There are a variety of models describing mass transfer among phases. A common form of mass transfer relationship is given by (Miller et al., 1990):

$$J = k_m \cdot (C_s - C_\infty) \qquad \text{(Eq. 2.4)}$$

Where J is solute mass flux to aqueous phase ($ML^{-2}T^{-1}$); k_m is mass transfer coefficient (LT^{-1}), C_s is the solute solubility concentration (ML^{-3}) and C_∞ is aqueous phase solute concentration (ML^{-3}) (Pankow and Cherry, 1996). For the dissolution of DNAPL residuals, the mass transfer rate is defined per volume of porous media ($ML^{-3}T^{-1}$). Hence, the mass transfer rate coefficient $K°$ (T^{-1}) is used rather than k_m by multiplying k_m with a_{na}, $a_{na} = A_{na}/V$, where a_{na} is the specific interfacial area (L^{-1}), A_{na} is the surface contact area (L^2), V is the volume of the porous media (L^3).

Supposing the C_∞ is zero, the analytical solution of k_m for the regular DNAPL pool dissolution is given by Johnson and Pankow (1992):

$$k_m = \frac{J}{C_s} = \frac{2\varepsilon}{\sqrt{\pi}} \sqrt{D_{TV} \overline{U} / L_p} \qquad \text{(Eq. 2.5)}$$

where ε is porosity. The mass transfer coefficient k_m is a parameter controlled largely by the water flow conditions. Laboratory studies show that, at groundwater flow velocities below 1 m/d (1e–5 m/s), the dissolution of residual DNAPL is not limited by the rate of interphase mass transfer but by the DNAPL solubility and molecular diffusion coefficient. Stagnant film model is most commonly used to describe this mass transfer rate by Fick's law, $k_m = D_m/\delta_s$, where D_m is molecular diffusion coefficient, δ_s is the thickness of stagnant layer. In contrast, dissolution become mass transfer rate limited when groundwater flow velocities is above 1 m/d (Imhoff et al., 1998; Schwille, 1988). In the DNAPL pool dissolution, less-than-saturated dissolved concentrations are often observed when averaging over the effluent water above the interface. Only a small cross-sectional area of DNAPL pool is exposed to horizontal groundwater flow. Hence dissolution of DNAPL pool occurs predominantly along the margins of the pool, leading to a much lower dissolution rate than for a residual zone.

Furthermore, the dissolution of both non-ideally shaped and well-defined DNAPL pool were investigated by some authors in a three-dimensional saturated porous media through lab experiments and numerical modeling (Chrysikopoulos, 1995; Chrysikopoulos et al., 2000; Dela Barre et al., 2002;

Kim and Chrysikopoulos, 1999; Lee and Chrysikopoulos, 2002). These studies demonstrated the significant influence of groundwater flow velocity on the mass transfer rate of pool dissolution and the dissolved plume transportation.

2.1.2 Dimensionless numbers in mass transfer correlation

Mass transfer models in a general dimensionless form may be applicable to a range of contaminants, porous media, and flow conditions (Imhoff et al., 1998). In the literature reporting mass transfer data, dimensionless numbers are commonly used to quantify mass transfer coefficients by correlation with characteristic parameters that can easily be determined.

Sherwood number *Sh* is defined as the ratio of mass flux to the diffusive flux, which basically normalizes the mass flux to a compound specific property (diffusion coefficient) $Sh = k_m l/D_m$, where l is characteristic length which could be the stagnant layer thickness δ_s or grain size of a porous medium $\overline{d}_p$, D_m is the diffusion coefficient. It could be further correlated with Reynolds number *Re*, $Re = Ul/v$, where U is flow velocity, ν is kinematic viscosity, and Peclet number *Pe*, $Pe = Ul/D_m$, which involves flow considerations. The Sherwood number is commonly used in mass transfer correlation for residual NAPL. Some authors also use it as correlation for NAPL pools with the characteristic length l related to the pool size rather than the mean grain size (Kim and Chrysikopoulos, 1999).

More correlations among these dimensionless numbers are given in Pankow and Cherry (1996) summarizing the previous works. These correlations relate mass transfer coefficients to the measurable features of the porous media such as grain size. This then makes it possible to estimate mass transfer coefficients based on porous media characteristics.

2.2 HYPORHEIC FLOW IN WATER-SEDIMENT MEDIA

As discussed above, the rate of DNAPL dissolution strongly depends on the water flow rate along the DNAPL/water interface. In the case of DNAPL present in karst sediments, the flow field in the sediment needs to be known to quantify DNAPL dissolution. There are many studies on flow processes in streambed sediments, referred to as hyporheic flow, and mechanisms that induce it. In contrast, there is hardly any information available on flow in sediments present in karst conduit, which is here also referred to as hyporheic flow. In the following, the occurrence and mechanisms of hyporheic flow in streambed sediments will be briefly reviewed which serves as a basis for the study of hyporheic flow in karst sediments.

2.2.1 Hyporheic flow in surface hydrology

In a broad sense, the hyporheic zone is defined as the subsurface region within streambeds that exchanges water with the surface (Valett et al., 1993). The hyporheic zone is beyond direct observation and not easily sampled by traditional methods (White, 1993). The concept of coupled

surface-subsurface flows was initially proposed by Vaux (1968) in the context of fish spawning as part of his investigations of interstitial flow through gravel beds. He recognized the connection between hydrodynamic conditions in the stream and the pressure distribution at the sediment-water interface (SWI). During hyporheic exchange flow (HEF) water infiltrates into sediment and returns to the stream, which is critical to the functioning of steam ecosystems (Käser et al., 2013). Interactions between free flowing water and underlying sediments also take place in other environmental systems, e.g., overland flow during rainfall events, benthic boundary layer at lakes, wetlands and some ocean bottoms.

The driving forces of hyporheic flow are classified into categories: bedform-/flow-induced pressure variations related to velocity variations over obstacles (hydrodynamically induced advection); hydraulic gradient caused by geomorphological features, e.g. stream meanders, and in-stream structures, e.g. debris dam, riffle-pool sequences (hydrostatically induced advection); turbulent momentum transfer (Käser et al., 2009). Other drivers summarized by Santos et al. (2012) in coastal context includes: hydraulic gradients in coastal zones; seasonal oscillation of water table; wave and tidal pumping; fluid shear; density-driven convection; bio-irrigation and bio-perturbation and sediment compaction. All these driving forces addressed act essentially through pressure difference imposing on the sediment-water interface.

The bedform induced exchange has been thoroughly investigated by many researchers because it is commonly encountered at almost all free flowing water and sediment interfaces (Cardenas and Gooseff, 2008; Cardenas and Wilson, 2006; Cardenas and Wilson, 2007b; Cardenas et al., 2008; Sawyer et al., 2011; Thibodeaux and Boyle, 1987). The interaction of free flow with the streambed topography generates an irregular pressure distribution along the interface thus causing water circulation within the underlying porous media (Cardenas and Wilson, 2007a). In many hyporheic exchange studies, idealized triangular bedform topography was assumed (Cardenas and Wilson, 2007b; Elliott and Brooks, 1997). Hyporheic flow occurs over a wide spatial scale ranging from millimeters to kilometers, and temporal scale from seconds to years (Boulton et al., 1998). Understanding the timescales of surface water-groundwater — hyporheic exchange is a step towards quantifying the rates of important biogeochemical reactions (Cardenas, 2008), e.g., the cycling of nitrogen. Hyporheic flow could have a positive effect on water quality by filtration and due to biogeochemical transformation of solutes as shown for streams (Boulton et al., 1998; Mermillod-Blondin et al., 2000; Mermillod-Blondin et al., 2004; Vervier et al., 1993), or impair the water quality by releasing contaminants trapped in the sediments, for example DNAPLs (Zhang et al., 2000; Zoumis et al., 2001).

2.2.2 Hyporheic flow in karst settings

Similar as in streambeds, hyporheic flow could also occur in sediments present in karst conduits although the process has received little attention so far (Herman et al., 2012). Two types of hyporheic processes can be distinguished depending on the permeability of the rock surrounding the conduit. In

case of low permeability rock, hyporheic exchange mainly occurs between the conduits and sediments. For high permeability rock, exchange between conduits and the rock matrix can be relevant, too.

There is hardly any data on hyporheic flow in karst conduits are available so far. Temperature measurements made in karst sediments by Dogwiler and Wicks (2005) suggest that hyporheic flow might indeed occur. In a theoretical study, Cardenas and Gooseff (2008) evaluated the effect of a cover (e.g. an ice layer) on hyporheric exchange in streambed sediments using numerical simulations which has some similarities to karst conduits. They observed that the cover leads to an increased but shallower hyporheic flow compared to open channel for an analogous bedform. They also speculated that the additional resistance due to the cover might lead to a decrease in bed form steepness and thus indirectly influenced hyporheic exchange. Reinterpretation of results from previous studies on contaminant transport suggests that karst hyporheic flow could have an effect on water quality. While contaminant breakthrough is rapid during high flow events (Einsiedl et al., 2010; Magal et al., 2013; Mahler and Massei, 2007; Mahler and Garner, 2009; Pronk et al., 2007), hyporheic flow might improve water quality during base flow when likely a higher fraction of conduit water might exchange with sediments. For example, Morasch (2013) observed a strong decrease in atrazine concentration between the swallow hole and karst spring. This was assumed to be caused by the sorption of contaminants to sediment particles within karst aquifer, and biodegradation by autochthonous endokarst microbial communities.

Early studies also demonstrate the retention of contaminants in karst conduits although the possible role of hyporheic exchange was not specifically evaluated (Heinz et al., 2009; Iker et al., 2010; Wilhartitz et al., 2009). Heinz et al. (2009) observed a delayed release of the bacterial contamination from the aquifer and decreasing organic micro-pollutant concentrations between a swallow hole and a spring. They hypothesized that biotransformation was responsible for the decreasing concentrations rather than only sorption or dilution. Wilhartitz et al. (2009) revealed that the microbial communities associated with the karst sediments contributed to self-purification processes. Iker et al. (2010) observed low atrazine concentrations in karst springs despite the application of high loads in the catchment. Using microcosms studies, they demonstrate a high potential for atrazine biodegradation in karst sediments previously exposed to atrazine, which could contribute to self-purification in the karst system.

In addition, toxic metals (Munteanu et al., 2012) and PCBs were found to accumulate in cave sediments (Pezdirc et al., 2011). Although the studies do not specifically address hyporheic flow, the presence of contaminants in sediments and the biodegradation potential are indirect indicators of hyporheic flow.

2.3 MATHEMATICAL DESCRIPTION OF FREE FLOW AND POROUS MEDIA

As a basis for modeling flow and transport processes in the conduit and sediment system, concepts of coupling between the two domains and their mathematical description are reviewed. Free flow/porous media interfaces are commonly encountered in natural situations (e.g. overland flow during rainfall events, benthic boundary layer at lakes, wetlands and some ocean bottoms), technical applications (e.g. thermal insulation, filtration processes, solidification of multi-components melts, spreading on porous substrates), and bio-engineering applications (e.g. blood vessels).

Due to its theoretical and practical interest, intense research activities were carried out to study these coupled processes (see Gobin and Goyeau (2008) for a review). The problem is characterized by fast moving flow above the interface and slow porous media flow below which leads to inherent difficulties in modeling the flow through the whole domains. There is no general agreement on the exact mathematical representation of the boundary condition at the interface between free flow and porous media, which remains an active research field (Gobin and Goyeau, 2008; Le Bars and Worster, 2006; Shavit et al., 2004). While numerical models have provided insights into processes and increased predictive capabilities, there is a lack of measurements and experimental data (Santos et al., 2012). The modeling approaches can be divided into two types, single domain and two-domain approaches. The two-domain approach addresses each domain separately with different flow equations and the coupling of flow needs to be considered. In contrast, the single domain approach uses one generalized formulation across the two domains, without specification of the interfacial boundary conditions. In summary, the selection of the approach depends on flow conditions and properties of the porous medium in question.

2.3.1 Two domain approach

For the two domain approach, fluid flow in the free flow region is described with the Navier-stokes equation, which is strictly a statement of conservation of momentum. For incompressible fluids, the equations correspond to:

$$\frac{\partial}{\partial t}(\rho U) + \rho U \cdot \nabla U = -\nabla p + \mu \nabla^2 U + \rho g \qquad \text{(Eq. 2.6)}$$

Where U the fluid velocity vector, ρ is the fluid density, p is the pressure field, μ is the dynamic viscosity of the fluid, g is gravitational acceleration. The Navier-Stokes equation (Eq. 2.6) is strictly a statement of the conservation of momentum. The additional mass continuity equation (Eq. 2.7) is usually needed, which describes the conservation of mass for the incompressible flow.

$$\nabla \cdot U = 0 \qquad \text{(Eq. 2.7)}$$

The derivation of Navier-Stokes equations begins with application of Newton's second law of motion. For a control volume, the time-rate of change of momentum equals the sum of forces acting on the material region. The left side is the acceleration, composed of unsteady acceleration and

convective acceleration. The right side is a sum of forces, divergence of stress (pressure stress and shear stress), body force if any (gravity for example).

At low flow velocities, advective inertial forces are small compared to viscous forces, also denoted as creeping flow. Under this conditions, the simpler Stokes equation can be used rather than the full Navier-Stokes equation. Neglecting the inertial force, the left side of Navier-Stokes equation becomes zero, producing the Stokes equations

$$0 = -\nabla p + \mu \nabla^2 U + \rho g \qquad \text{(Eq. 2.8)}$$

This is a typical situation in flows where the fluid velocities are very slow, i.e. Re « 1, the viscosities are very large, or the length-scales of the flow are very small. The momentum equation suggests that the pressure gradient is balanced by viscous forces due to fluid-fluid interactions.

For the sediment domain, Darcy's law and Brinkman's equation are widely used to study flow in porous media (Le Bars and Worster, 2006). In a homogeneous layer of low porosity, Darcy's law is most commonly used. Darcy' equation relates the macroscopic pressure gradient to the average flow in porous media.

$$\frac{\mu}{k} q = -\nabla p + \rho g \qquad \text{(Eq. 2.9)}$$

$$q = \varepsilon U \qquad \text{(Eq. 2.10)}$$

q is the Darcy velocity or flux (discharge per unit area, m/s) and ε is the porosity. Darcy's flow equation provides a linear relation between velocity and pressure in the porous media neglecting the inertial effects. The extension of Darcy's law was introduced by Brinkman to account for dissipation of momentum by macroscopic viscous forces, referred to as Brinkman's equation, of the form (Brinkman, 1947; Neale and Nader, 1974):

$$\frac{\mu}{k} q = -\nabla p + \tilde{\mu} \nabla^2 q + \rho g \qquad \text{(Eq. 2.11)}$$

$\tilde{\mu}$ is the effective viscosity, The left term is same as in Darcy's law and only addresses the microscopic viscous effect due to the presence of grains. The right second term is introduced to account for macroscopic shear effect in high porosity medium, usually greater than 0.9 (Nield, 1991). The value of the effective viscosity $\tilde{\mu}$ approaches limits in the pure solid with no flow ($\tilde{\mu} \to \infty$), and in pure liquid ($\tilde{\mu} \to \mu$). Its value in a porous media is therefore expected to be larger than the viscosity of the fluid and depends on the structure of the porous media, with a common approximation $\tilde{\mu} = \mu/\varepsilon$ (Vafai and Tien, 1981). Brinkman used an identical value for both viscosities. There is however, a remarkable disagreement with respect to the $\tilde{\mu}/\mu$ ratio among authors (Shavit et al., 2004), either larger or smaller than 1 for better matching the experimental results. Utilization of Darcy's law implies fluid slip at macroscopic boundaries, while the Brinkman term accounts for energy loss due to viscous effects induced by flow along macroscopic boundaries.

Many studies make use of the two-domain approach to analyze theoretical and practical problems (Cardenas and Wilson, 2007a; Cardenas and Wilson, 2007b; Discacciati et al., 2002; Faulkner et al., 2009; Kiwan and Alzahrany, 2008; Qin and Kaloni, 1993). Flow within each domain is solved separately. The combination of two domains requires appropriate interfacial conditions that describe the fluid flow across the surface of porous media. The solution of the velocity profile near the interface is sensitive to the boundary condition.

Coupling of flow

Different types of interfacial conditions between a porous medium and a fluid layer have been proposed (Alazmi and Vafai, 2001), which can be classified into two main categories, slip and no-slip interface conditions. Slip condition assumes the occurrence of a discontinuity in the interfacial tangential velocity. A non-negligible velocity exists at the interface where viscous shear appears to penetrate into the permeable material (Beavers and Joseph, 1967):

$$\frac{dU}{dz} = \gamma\,(U_B - q) \qquad \text{(Eq. 2.12)}$$

$$\gamma = \frac{\alpha_{B-J}}{\sqrt{k}} \qquad \text{(Eq. 2.13)}$$

Where U_B is the slip velocity at the interface, q is the Darcy velocity within the porous region, k is permeability of porous media, dU/dz is the velocity gradient, γ depends on the properties of the fluid and the permeable material, characterizing the boundary layer thickness δ (the depth until which the velocity gradients due to shear forces occurs), which is on the order of $\sqrt{k}$ (Kaviany, 1995). However, experimental studies suggest that δ is of the order of the grain diameter, which is much larger than the theoretical prediction (Goharzadeh et al., 2005; Gupte and Advani, 1997). The measured δ from (Goharzadeh et al., 2005) for different materials and grain size is 40-100 times the theoretical estimation. $\alpha_{B\text{-}J}$ is an empirical slip parameter, a dimensionless quantity depending on the structure of permeable material, with a wide range from 0.1 to 4. A widely used mathematical representation for $\alpha_{B\text{-}J}$ is $\sqrt{\tilde{\mu}/\mu}$ (Neale and Nader, 1974). However, the literature exhibits a remarkable disagreement in terms of the ratio of $\tilde{\mu}/\mu$, from <1 to >10 (Alazmi and Vafai, 2001; Shavit et al., 2004).

A no-slip boundary corresponds to zero flow velocity at the solid boundary due to viscous forces. It applies at the interface where slip velocities are so small that they could be ignored. For a compact porous medium of lower porosity, no-slip boundary condition is a safe assumption in almost every case (Tachie et al., 2003). Such conditions can be considered representative of many natural systems such as, lake sediments and some ocean bottoms.

2.3.2 Single domain approach

The single domain approach uses a generalized formulation for both the free flow and porous media which is widely used in industrial applications (Bousquet-Melou et al., 2002; Krishnan et al., 2005; Le Bars and Worster, 2006) and numerical simulation dealing with natural convection (Hsu and Cheng, 1985; Kiwan and Khodier, 2008; Lauriat and Prasad, 1987; Sivasankaran and Bhuvaneswari,

2013; Tong and Subramanian, 1985). In this approach, the porous layer is considered as a pseudo-fluid. The free flow and porous media are treated as a continuum. The transition from the free flow to the porous media is achieved through a continuous spatial variation of properties, such as the permeability k, porosity ε and viscosity μ. It is computationally efficient comparing to the two-domain coupling approach. This approach avoids explicit specification of the interfacial boundary condition between water and sediment by applying a generalized Darcy-Brinkman equation (Beckermann et al., 1988; Bennon and Incropera, 1987; Kaempfer and Rappaz, 2003)

$$\frac{\partial}{\partial t}(\rho q) + \frac{\rho}{\varepsilon} q \cdot \nabla q = -\varepsilon \nabla p + \varepsilon \rho g + \tilde{\mu} \nabla^2 q - \frac{\mu \varepsilon}{k} q \qquad \text{(Eq. 2.14)}$$

In the fluid channel, $\varepsilon = 1$, then $q = U$ in Eq. 2.10, the permeability is infinite, so the Darcy term approaches zero, and Eq. 2.14 reduces to Navier-Stokes equation. In the porous domain, the permeability is much smaller than in the fluid domain, Darcy's term becomes predominant.

The modeling approach applied in this study and the justifications will be presented after the experimental setup to be introduced in Chapter 3.

2.4 REFERENCE

Alazmi, B., Vafai, K., 2001. Analysis of fluid flow and heat transfer interfacial conditions between a porous medium and a fluid layer. International Journal of Heat and Mass Transfer, 44(9): 1735-1749.

Anderson, M.R., Johnson, R.L., Pankow, J.F., 1992a. Dissolution of dense chlorinated solvents into ground-water .1. Dissolution from a well-defined residual source. Ground Water, 30(2): 250-256.

Anderson, M.R., Johnson, R.L., Pankow, J.F., 1992b. Dissolution of dense chlorinated solvents into groundwater .3. Modeling contaminant plumes from fingers and pools of solvent. Environmental Science & Technology, 26(5): 901-908.

Beavers, G.S., Joseph, D.D., 1967. Boundary conditions at a naturally permeable wall. Journal of Fluid Mechanics, 30: 197-207.

Beckermann, C., Viskanta, R., Ramadhyani, S., 1988. Natural-convection in vertical enclosures containing simultaneously fluid and porous layers. Journal of Fluid Mechanics, 186: 257-284.

Bennon, W.D., Incropera, F.P., 1987. A continuum model for momentum, heat and species transport in binary solid liquid-phase change systems .1. Model formulation. International Journal of Heat and Mass Transfer, 30(10): 2161-2170.

Bird, R.B., Stewart, W.E., Lightfoot, E.N., 1960. Transport phenomena. John Wiley and Sons, New York.

Boulton, A.J., Findlay, S., Marmonier, P., Stanley, E.H., Valett, H.M., 1998. The functional significance of the hyporheic zone in streams and rivers. Annual Review of Ecology and Systematics, 29: 59-81.

Bousquet-Melou, P., Goyeau, B., Quintard, M., Fichot, F., Gobin, D., 2002. Average momentum equation for interdendritic flow in a solidifying columnar mushy zone. International Journal of Heat and Mass Transfer, 45(17): 3651-3665.

Brinkman, H.C., 1947. A calculation of the viscous force exerted by a flowing fluid on a dense swarm of particles. Applied Scientific Research Section a-Mechanics Heat Chemical Engineering Mathematical Methods, 1(1): 27-34.

Butcher, J.B., Gauthier, T.D., 1994. Estimation of residual dense NAPL mass by inverse modeling. Ground Water, 32(1): 71-78.

Cardenas, M.B., 2008. The effect of river bend morphology on flow and timescales of surface water-groundwater exchange across pointbars. Journal of Hydrology, 362(1-2): 134-141.

Cardenas, M.B., Gooseff, M.N., 2008. Comparison of hyporheic exchange under covered and uncovered channels based on linked surface and groundwater flow simulations. Water Resources Research, 44(3).

Cardenas, M.B., Wilson, J.L., 2006. The influence of ambient groundwater discharge on exchange zones induced by current-bedform interactions. Journal of Hydrology, 331(1-2): 103-109.

Cardenas, M.B., Wilson, J.L., 2007a. Dunes, turbulent eddies, and interfacial exchange with permeable sediments. Water Resources Research, 43(8).

Cardenas, M.B., Wilson, J.L., 2007b. Hydrodynamics of coupled flow above and below a sediment-water interface with triangular bedforms. Advances in Water Resources, 30(3): 301-313.

Cardenas, M.B., Wilson, J.L., Haggerty, R., 2008. Residence time of bedform-driven hyporheic exchange. Advances in Water Resources, 31(10): 1382-1386.

Chrysikopoulos, C.V., 1995. 3-dimensional analytical models of contaminant transport from nonaqueous phase liquid pool dissolution in saturated subsurface formations. Water Resources Research, 31(4): 1137-1145.

Chrysikopoulos, C.V., Kim, T.J., 2000. Local mass transfer correlations for nonaqueous phase liquid pool dissolution in saturated porous media. Transport in Porous Media, 38(1-2): 167-187.

Chrysikopoulos, C.V., Lee, K.Y., Harmon, T.C., 2000. Dissolution of a well-defined trichloroethylene pool in saturated porous media: Experimental design and aquifer characterization. Water Resources Research, 36(7): 1687-1696.

Chrysikopoulos, C.V., Voudrias, E.A., Fyrillas, M.M., 1994. Modeling of contaminant transport resulting from dissolution of nonaqueous phase liquid pools in saturated porous-media. Transport in Porous Media, 16(2): 125-145.

Dela Barre, B.K., Harmon, T.C., Chrysikopoulos, C.V., 2002. Measuring and modeling the dissolution of nonideally shaped dense nonaqueous phase liquid pools in saturated porous media. Water Resources Research, 38(8).

Discacciati, M., Miglio, E., Quarteroni, A., 2002. Mathematical and numerical models for coupling surface and groundwater flows. Applied Numerical Mathematics, 43(1-2): 57-74.

Dogwiler, T., Wicks, C.M., 2005. Thermal variations in the hyporheic zone of a karst stream. Speleogenesis Evol Karst Aquifers, 3(1): 1-11.

Einsiedl, F., Radke, M., Maloszewski, P., 2010. Occurrence and transport of pharmaceuticals in a karst groundwater system affected by domestic wastewater treatment plants. Journal of Contaminant Hydrology, 117(1-4): 26-36.

Elliott, A.H., Brooks, N.H., 1997. Transfer of nonsorbing solutes to a streambed with bed forms: Laboratory experiments. Water Resources Research, 33(1): 137-151.

Faulkner, J., Hu, B.X., Kish, S., Hua, F., 2009. Laboratory analog and numerical study of groundwater flow and solute transport in a karst aquifer with conduit and matrix domains. Journal of Contaminant Hydrology, 110(1-2): 34-44.

Fure, A.D., Jawitz, J.W., Annable, M.D., 2006. DNAPL source depletion: Linking architecture and flux response. Journal of Contaminant Hydrology, 85(3-4): 118-140.

Geller, J.T., Hunt, J.R., 1993. Mass-transfer from nonaqueous phase organic liquids in water-saturated porous-media. Water Resources Research, 29(4): 833-845.

Gobin, D., Goyeau, B., 2008. Natural convection in partially porous media: a brief overview. International Journal of Numerical Methods for Heat & Fluid Flow, 18(3-4): 465-490.

Goharzadeh, A., Khalili, A., Jorgensen, B.B., 2005. Transition layer thickness at a fluid-porous interface. Physics of Fluids, 17(5).

Gupte, S.K., Advani, S.G., 1997. Flow near the permeable boundary of a porous medium: An experimental investigation using LDA. Experiments in Fluids, 22(5): 408-422.

Heinz, B. et al., 2009. Water quality deterioration at a karst spring (Gallusquelle, Germany) due to combined sewer overflow: evidence of bacterial and micro-pollutant contamination. Environmental Geology, 57(4): 797-808.

Herman, E., Toran, L., White, W., 2012. Clastic sediment transport and storage in fluviokarst aquifers: an essential component of karst hydrogeology. Carbonates and Evaporites, 27(3-4): 211-241.

Hsu, C.T., Cheng, P., 1985. The brinkman model for natural-convection about a semi-infinite vertical flat-plate in a porous-medium. International Journal of Heat and Mass Transfer, 28(3): 683-697.

Hunt, J.R., Sitar, N., Udell, K.S., 1988. Nonaqueous phase liquid transport and cleanup .1. Analysis of mechanisms. Water Resources Research, 24(8): 1247-1258.

Iker, B.C., Kambesis, P., Oehrle, S.A., Groves, C., Barton, H.A., 2010. Microbial atrazine breakdown in a karst groundwater system and its effect on ecosystem energetics. Journal of Environmental Quality, 39(2): 509-518.

Imhoff, P.T., Arthur, M.H., Miller, C.T., 1998. Complete dissolution of trichloroethylene in saturated porous media. Environmental Science & Technology, 32(16): 2417-2424.

Johnson, R.L., Pankow, J.F., 1992. Dissolution of dense chlorinated solvents into groundwater .2. Source functions for pools of solvent. Environmental Science & Technology, 26(5): 896-901.

Kaempfer, T.U., Rappaz, M., 2003. Modelling of macrosegregation during solidification processes using an adaptive domain decomposition method. Model. Simul. Mater. Sci. Eng., 11(4): 575-597.

Käser, D.H., Binley, A., Heathwaite, A.L., 2013. On the importance of considering channel microforms in groundwater models of hyporheic exchange. River Res. Appl., 29(4): 528-535.

Käser, D.H., Binley, A., Heathwaite, A.L., Krause, S., 2009. Spatio-temporal variations of hyporheic flow in a riffle-step-pool sequence. Hydrol. Process., 23(15): 2138-2149.

Kaviany, M., 1995. Principles of heat transfer in porous media. Springer, NewYork.

Kim, T.J., Chrysikopoulos, C.V., 1999. Mass transfer correlations for nonaqueous phase liquid pool dissolution in saturated porous media. Water Resources Research, 35(2): 449-459.

Kiwan, S., Alzahrany, M.S., 2008. Effect of using porous inserts on natural convection heat transfer between two concentric vertical cylinders. Numer. Heat Tranf. A-Appl., 53(8): 870-889.

Kiwan, S., Khodier, M., 2008. Natural convection heat transfer in an open-ended inclined channel-partially filled with porous media. Heat Transf. Eng., 29(1): 67-75.

Krishnan, S., Murthy, J.Y., Garimella, S.V., 2005. A two-temperature model for solid-liquid phase change in metal foams. Journal of Heat Transfer-Transactions of the Asme, 127(9): 995-1004.

Lauriat, G., Prasad, V., 1987. Natural-convection in a vertical porous cavity - a numerical study for brinkman-extended darcy formulation. Journal of Heat Transfer-Transactions of the Asme, 109(3): 688-696.

Le Bars, M., Worster, M.G., 2006. Interfacial conditions between a pure fluid and a porous medium: implications for binary alloy solidification. Journal of Fluid Mechanics, 550: 149-173.

Lee, K.Y., Chrysikopoulos, C.V., 2002. Dissolution of a well-defined trichloroethylene pool in saturated porous media: experimental results and model simulations. Water Research, 36(15): 3911-3918.

Magal, E. et al., 2013. Determination of pollution and recovery time of karst springs, an example from a carbonate aquifer in Israel. Journal of contaminant hydrology, 145: 26-36.

Mahler, B., Massei, N., 2007. Anthropogenic contaminants as tracers in an urbanizing karst aquifer. Journal of Contaminant Hydrology, 91(1-2): 81-106.

Mahler, B.J., Garner, B.D., 2009. Using nitrate to quantify quick flow in a karst aquifer. Ground Water, 47(3): 350-360.

Mermillod-Blondin, F., Des Chatelliers, M.C., Marmonier, P., Dole-Olivier, M.J., 2000. Distribution of solutes, microbes and invertebrates in river sediments along a riffle-pool-riffle sequence. Freshwater Biology, 44(2): 255-269.

Mermillod-Blondin, F. et al., 2004. Relative influence of bioturbation and predation on organic matter processing in river sediments: a microcosm experiment. Freshwater Biology, 49(7): 895-912.

Miller, C.T., Poiriermcneill, M.M., Mayer, A.S., 1990. Dissolution of trapped nonaqueous phase liquids - mass-transfer characteristics. Water Resources Research, 26(11): 2783-2796.

Morasch, B., 2013. Occurrence and dynamics of micropollutants in a karst aquifer. Environ. Pollut., 173: 133-137.

Munteanu, C.-M., Giurginca, A., Giurginca, M., Panaiotu, C.-G., Niculescu, G., 2012. Potentially toxic metals concentrations in soils and cave sediments from karst areas of mehedinti and gorj counties (romania). Carpathian Journal of Earth and Environmental Sciences, 7(1): 193-204.

Neale, G., Nader, W., 1974. Practical significance of brinkmans extension of darcys law - coupled parallel flows within a channel and a bounding porous-medium. Canadian Journal of Chemical Engineering, 52(4): 475-478.

Nield, D.A., 1991. The limitations of the brinkman-forchheimer equation in modeling flow in a saturated porous-medium and at an interface. International Journal of Heat and Fluid Flow, 12(3): 269-272.

Page, J.W.E., Soga, K., Illangasekare, T., 2007. The significance of heterogeneity on mass flux from DNAPL source zones: An experimental investigation. Journal of Contaminant Hydrology, 94(3-4): 215-234.

Pankow, J.F., Cherry, J.A., 1996. Dense chlorinated solvents and other DNAPL's in groundwater. Waterloo Press, Portland, Oregon.

Pezdirc, M., Heath, E., Mali, L.B., Bulog, B., 2011. PCB accumulation and tissue distribution in cave salamander (Proteus anguinus anguinus, Amphibia, Urodela) in the polluted karstic hinterland of the Krupa River, Slovenia. Chemosphere, 84(7): 987-993.

Pronk, M., Goldscheider, N., Zopfi, J., 2007. Particle-size distribution as indicator for fecal bacteria contamination of drinking water from karst springs. Environmental Science & Technology, 41(24): 8400-8405.

Qin, Y., Kaloni, P.N., 1993. Creeping flow past a porous spherical-shell. Z. Angew. Math. Mech., 73(2): 77-84.

Santos, I.R., Eyre, B.D., Huettel, M., 2012. The driving forces of porewater and groundwater flow in permeable coastal sediments: A review. Estuarine Coastal and Shelf Science, 98: 1-15.

Sawyer, A.H., Cardenas, M.B., Buttles, J., 2011. Hyporheic exchange due to channel-spanning logs. Water Resources Research, 47.

Schwille, F., 1988. Dense chlorinated solvents in porous and fractured media - Model experiments. Lewis, Boca Raton, FL.

Shavit, U., Rosenzweig, R., Assouline, S., 2004. Free flow at the interface of porous surfaces: A generalization of the Taylor brush configuration. Transport in Porous Media, 54(3): 345-360.

Sivasankaran, S., Bhuvaneswari, M., 2013. Natural convection in a porous cavity with sinusoidal heating on both sidewalls. Numer. Heat Tranf. A-Appl., 63(1): 14-30.

Sudicky, E.A., 1986. A natural gradient experiment on solute transport in a sand aquifer - spatial variability of hydraulic conductivity and its role in the dispersion process. Water Resources Research, 22(13): 2069-2082.

Tachie, M.F., James, D.F., Currie, I.G., 2003. Velocity measurements of a shear flow penetrating a porous medium. Journal of Fluid Mechanics, 493: 319-343.

Thibodeaux, L.J., Boyle, J.D., 1987. Bedform-generated convective-transport in bottom sediment. Nature, 325(6102): 341-343.

Tong, T.W., Subramanian, E., 1985. A boundary-layer analysis for natural-convection in vertical porous enclosures - use of the brinkman-extended darcy model. International Journal of Heat and Mass Transfer, 28(3): 563-571.

Vafai, K., Tien, C.L., 1981. Boundary and inertia effects on flow and heat-transfer in porous-media. International Journal of Heat and Mass Transfer, 24(2): 195-203.

Valett, H.M., Hakenkamp, C.C., Boulton, A.J., 1993. Perspectives on the hyporheic zone: Integrating hydrology and biology. Introduction. Journal of the North American Benthological Society, 12(1): 40-43.

van der Waarden, M., Bridie, A., Groenewo.Wm, 1971. Transport of mineral oil components to groundwater .1. Model experiments on transfer of hydrocarbons from a residual oil zone to trickling water. Water Research, 5(5): 213-&.

van der Waarden, M., Groenewoud, W.M., Bridie, A., 1977. Transport of mineral-oil components to groundwater .2. Influence of lime, clay and organic soil components on rate of transport. Water Research, 11(4): 359-365.

Vaux, W.G., 1968. Intragravel flow and interchange of water in a streambed. United States Fish and Wildlife Service Fishery Bulletin, 66(3): 479-&.

Vervier, P., Dobson, M., Pinay, G., 1993. Role of interaction zones between surface and ground waters in doc transport and processing - considerations for river restoration. Freshwater Biology, 29(2): 275-284.

White, D.S., 1993. Perspectives on defining and delineating hyporheic zones. Journal of the North American Benthological Society, 12(1): 61-69.

Wilhartitz, I.C. et al., 2009. Heterotrophic prokaryotic production in ultraoligotrophic alpine karst aquifers and ecological implications. Fems Microbiology Ecology, 68(3): 287-299.

Zhang, Y., Wu, R.S.S., Hong, H.S., Poon, K.F., Lam, M.H.W., 2000. Field study on desorption rates of polynuclear aromatic hydrocarbons from contaminated marine sediment. Environmental Toxicology and Chemistry, 19(10): 2431-2435.

Zoumis, T., Schmidt, A., Grigorova, L., Calmano, W., 2001. Contaminants in sediments: remobilisation and demobilisation. Science of the Total Environment, 266(1-3): 195-202.

Chapter 3

Experimental investigation of hyporheic flow in conduit-sediment system

ABSTRACT

Karst conduits are often partly filled by clastic sediments. Flow through such sediments can have a strong impact on the fate of sediment-entrapped contaminants. In contrast to stream bed sediments, hyporheic flow in karst sediments has received little attention so far. For karst sediments, conduit bends could induce hyporheic flow, in addition to bedforms or obstacles. The main aim of this study was to investigate flow processes in a conduit-sediment system using a laboratory model resembling a siphon and numerical modeling. In the laboratory system, zones with forward and reverse flow occurred in the sediment due to the conduit bends. As demonstrated with sediment-source tracer test, entrapped solutes were generally flushed out more rapidly at a higher flow rate and steeper conduit angle. Numerical modeling assuming pressure continuity across the conduit-sediment interface reproduced the flow patterns and breakthrough curves (BTCs) well. Based on the model, the magnitude of hyporheic exchange is expected to increase linearly with the flow rate and was higher for a steeper conduit angle. However, the increase in flushing intensity was not evenly distributed throughout the sediments but occurred mainly adjacent to the conduit bends consistent with observations from tracer tests. This study confirms that conduit bends could have a strong influence on hyporheic flow in karst sediments.

3.1 INTRODUCTION

Many environmental systems involve free flowing water over a sediment layer, e.g., flow over streambed, overland flow during rainfall events, benthic boundary layer at lakes, wetlands and some ocean bottoms. Mechanisms of advective flow in such sediments have received increasing attention, especially hyporheric flow in streambed sediments, due its importance for biogeochemical and ecological processes in streams (Choe et al., 2004; Harvey and Fuller, 1998; Karwan and Saiers, 2012; Packman and Brooks, 2001). Different driving forces have been identified that induce hyporheic flow, including bedform and obstacle generated flushing, wave and tidal pumping, and biogenic processes (Cardenas, 2008; Cardenas and Gooseff, 2008; Cardenas and Wilson, 2006; Cardenas and Wilson, 2007b; Santos et al., 2012; Sawyer et al., 2011; Thibodeaux and Boyle, 1987).

Similarly as in streams, hyporheic exchange could also occur in karst conduits that often contain sediments. In such systems, hyporheic flow could have a positive effect on water quality by filtration and due to biogeochemical transformation of solutes similarly as for streams (Boulton et al., 1998; Mermillod-Blondin et al., 2000; Mermillod-Blondin et al., 2004; Vervier et al., 1993) or impair the water quality by releasing contaminants trapped in the sediments, for example dense non-aqueous liquids (DNAPLs) (Zhang et al., 2000; Zoumis et al., 2001). However, hyporheic flow in karst conduits has received little attention so far. Cardenas and Gooseff (2008) have evaluated the effect of a cover (e.g., an ice layer) on hyporheic exchange in streambed sediments using numerical simulations which has some similarities to karst conduits. They observed that the cover led to an increased but shallower hyporheic flux compared to open channels for an analogous bedform. They also hypothesized that the additional resistance due to the cover might lead to a decrease in bedform steepness and thus indirectly influence hyporheic exchange. Furthermore, the exchange processes between conduits and the matrix was simulated in a laboratory analogue study (Faulkner et al., 2009; Li et al., 2008).

While in karst conduits, hyporheic exchange could be driven by the bedform topography similarly as in streambeds, the geometry of the karst conduits that directs the flow towards the sediment surface could play an important role, too. In the classical illustration of the karst genesis within carbonate rock (Ford and Ewers, 1978), discrete passages are preferentially developed following bedding planes and fractures both along and perpendicular to the dip of the stratum. These passages often evolve into siphon forms (Milanovic, 2007). In such structures, hyporheic flow might even occur in a flat sediment layer due to pressure gradients induced by the flow approaching the sediment surface at an angle and shear forces of water flowing along the sediment surface. Such a situation could for example occur in a siphon partly filled by sediments. Karst conduits are rich in clastic sediments of varied sizes, from clays and silts, to sands and gravels, and large to cobbles and boulders. Contaminants such as heavy metals (Vesper and White, 2003), and fecal bacteria (Pronk et al., 2006; Pronk et al., 2007) can become trapped in sediments and might be remobilized with suspended matter originating from sediment deposits.

The main aim of this study was to explore how conduit-constrained flow that approaches a sediment surface at an angle drives hyporheic exchange. The study included laboratory experiments and numerical simulations. In this study, the sediments were assumed to have a higher permeability than the surrounding rock matrix and hence exchange processes with the matrix were not taken into account (Loop and White, 2001). The laboratory system had a shape that grossly resembled a common element of a karst conduit. In the laboratory system, the effects of two different conduit curvatures and different flow velocities on hyporheic exchange were explored. Hyporheic exchange was visualized and quantified by injecting a small volume of a fluorescent tracer in the sediment and recording the tracer flow pattern with a video camera and the breakthrough curve with a fluorescence spectrometer. Numerical modeling was used to evaluate flow paths in more detail and to gain an additional understanding of the mechanisms controlling flow and transport processes.

3.2 METHODS

3.2.1 Experimental setup

A laboratory analog model was chosen to investigate the interaction of flow and solute transport between conduit and sediments in detail. The conduit consisted of glass tubes with a total length of about 0.9 m, internal diameter of 2 cm, and a horizontal central part for packing sediments (Fig. 3.1). The photo of the experimental setup is shown in Appendix a, Fig. A1. Two systems were constructed with tubes attached at an angle of 15° (denoted as 15D) with a curvature of 0.04 (ratio of the tube radius to curve radius) and 45° (denoted as 45D) with a curvature of 0.1, respectively. These dimensions were chosen by scaling down typical siphon conduits (Milanovic, 2007), and to ensure that the system is compatible with flow rates feasible in a laboratory setting and with the available parts for controlling flow and measuring tracer concentrations.

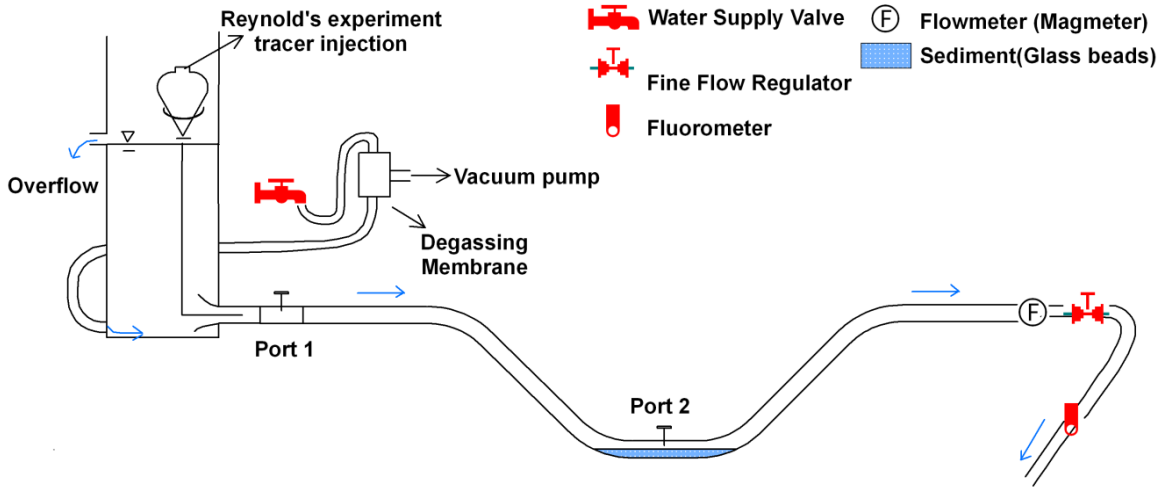

Fig. 3.1 Schematic diagram of experimental apparatus for streamline tracing and sediment tracer tests

A water tank with a constant head of 25 cm above the tube inlet fed the tube entering from a trumpet mouth entrance (Fig. 3.1). The water entering the tank was degassed by passing through a membrane module under vacuum to avoid bubble formation in the system that would disturb the online tracer analysis. At the outflow of the tube, a Sika induQ magnetic-inductive flow meter (Sika, Germany) was attached (accuracy: 1% of reading), followed by a LVN (Locker Valve Needle) valve (SMC, Japan) to control the flow. A fraction of the outflowing water was pumped at a constant rate (85 ml/min) through a fluorescence spectrometer.

The sediment consisted of glass beads of a diameter of 1 mm resulting in a stable packing even at larger flow rates, which was not the case when using smaller diameter beads. During each run, the glass beads were added into the tube to a height of 1 cm prior to filling the tube with water. The tube was then shaken until a relatively planar surface was achieved while water was flowing at a low rate through the tube.

3.2.2 Representativity of scale model

For a scale model to be representative of the real system, it needs to fulfill the criteria of geometric and dynamic similarity (Chanson, 1999). A scale model is geometrically similar to the real system if all the linear length scales of the scale model are a fixed ratio of the corresponding length scales of the real system. Thus our laboratory siphon system of 90 cm length and 2 cm diameter corresponds for example to a structure of 45 m length with a diameter of 1 m which is in a realistic range (Ford and Williams, 2007; Milanovic, 2007). Dynamic similarity is ensured if the forces acting at corresponding locations on the scale model and real system are everywhere in the same ratio. For full-enclosed flow such as in the completely water filled conduits, dynamic similarity is achieved if the Reynolds number is the same for the scale model and reality. Therefore, experimental conditions are always characterized with the Reynolds number in this study. The Reynolds number is given by:

$$Re = \frac{\overline{U_c} H}{\nu} \qquad \text{(Eq. 3.1)}$$

where $\overline{U_c}$ is the average flow velocity in conduit, H the conduit diameter and ν the kinematic viscosity.

Given that the fluid is the same in the scale model and reality (same kinetic viscosity), the linear velocity in the real system with the larger diameter is lower than in the scale model for a given Reynolds number. The velocity ratio is indirectly proportional to the ratio of the length scales. Hence, the experiments presented in this study represent low flow conditions consistent with the assumption that the sediments remain static. Siphons are expected to remain fully saturated even under low flow conditions. To ensure the higher flow rate in the scale models despite the smaller diameter, the pressure gradient needs to be higher than in the real system. Accordingly, the flow rate in the porous medium of the scale model will be higher than in reality i.e. the scale model has to be considered to represent a situation where sediments have a high permeability. While the conditions of geometric and dynamic similarity are fulfilled, the scale model still represents real systems only in a simplified way

especially because the roughness of conduit walls and the heterogeneity of sediments are not taken into account. The detailed scaling analyses on different properties can be found in Appendix c.1-3.

3.2.3 Tracer tests

Reynolds experiments were carried out to characterize the flow regimes in the tube. In these experiments, a dye tracer was injected continuously and the wavering of the dye streak was observed (Tritton, 1988). Sulforodamine G was injected at a constant flow rate of 0.22 ml/min via a fine tube connected to a tracer reservoir (Fig. 3.1). The tracer pattern associated with different flow regimes are illustrated in Appendix a, Fig. A2.

In order to probe the velocity field in the sediment, sediment-source tracer tests were conducted at different conduit flow rates covering laminar, transitional and turbulent flow regimes. A volume of 110 µl Uranine solution 2 g/l was injected into the bottom of sediment via the injection port 2 in the horizontal section of the tube (Fig. 3.1). During each experiment, the tracer was injected under the same low flow rate corresponding to *Re* 200. The flow rate was then adjusted to the respective value of the experiment, corresponding to conduit *Re* of about 200–2000. A syringe with a blunt tip needle was used to ensure that the tracer distributed radially around the needle tip. Tracer tests were repeated three times at each flow rate.

3.2.4 Mathematical description

Modeling approach

The coupling of free and porous media flow has been the focus of intense research (Alazmi and Vafai, 2001; Gobin and Goyeau, 2008; Le Bars and Worster, 2006; Liu and Prosperetti, 2011; Neale and Nader, 1974; Saffman, 1971), much of which was oriented towards heat and mass transfer in industrial applications. Special attention was brought to the exchange boundary condition linking the two domains, with experimental studies pioneered by Beavers and Joseph (1967). The conceptual and numerical approach can be divided into two main class, two domain approach and single domain approach. For details of the two approaches, the reader is referred to Gobin and Goyeau (2008) who provides an overview of the governing equations and range of application of the two approaches.

In this study, the two-domain approach was chosen, which simulated fast conduit flow and slow sediment flow separately. Flow fields were coupled by assuming pressure continuity across the two domains. Hence, the zones of conduit flow and sediment flow were subject to a continuous pressure field. Whereas flow velocity across the sediment water interface (SWI) was discontinuous. In previous studies, this approach was successfully applied for the simulation of hyporheic flow driven by stream bedforms (Cardenas and Wilson, 2007b; Cardenas et al., 2008) and river morphology (Cardenas, 2008). A non-slip boundary was assigned at the SWI. Compared to the criterion of $Da < 10^{-4}$ ($Da = k/h^2$, k is the permeability of underlying porous media, h is the height of flow column) for a negligible slip boundary condition (Jimenez-Islas et al., 1999; Lauriat and Prasad, 1987), the value of *Da*

calculated with the analog model is within the range of 10^{-6}–10^{-5}, hence, no-slip boundary condition was justified to be valid. In addition, the slip boundary was also verified negligible in typical field scale of karst conduit aquifer (Li et al., 2012).

Governing equations

The water flow in the conduit is governed by the Navier–Stokes equations consisting of a momentum and a mass balance equation for the incompressible flow:

$$\frac{\partial}{\partial t}(\rho U) + \rho U \cdot \nabla U = -\nabla p + \mu \nabla^2 U \qquad \text{(Eq. 3.2)}$$

$$\nabla \cdot U = 0 \qquad \text{(Eq. 3.3)}$$

where U the velocity vector, p is the fluid pressure, ρ is the fluid density, μ is the dynamic viscosity, t is time. The left hand-side of Eq. 3.2 corresponds to local acceleration and convective acceleration; and the right hand-side is a summation of the pressure and viscous forces.

Flow in the porous media is described by Darcy's equation.

$$\frac{\mu}{k} q = -\nabla p \qquad \text{(Eq. 3.4)}$$

$$\nabla \cdot q = 0 \qquad \text{(Eq. 3.5)}$$

where k is the permeability of the porous medium, q is the Darcy velocity.

Solute transport is simulated by the advection–dispersion equation:

$$\frac{\partial C}{\partial t} = \nabla \cdot [(D + D_e)\nabla C] - \nabla \cdot (CU) \qquad \text{(Eq. 3.6)}$$

where c is solute concentration, D is the mechanical dispersion coefficient tensor, D_e is the effective molecular diffusion which equals the molecular diffusion coefficient multiplied by the tortuosity (Zheng and Bennett, 2002). The dispersion coefficient tensor is defined as a symmetrical matrix according to the equations given by Burnett and Frind (1987).

The chosen modeling approach is strictly only valid for laminar flow conditions, while in this study experiments were also conducted at transitional and turbulent flow. Nevertheless, the laminar flow approach is expected to provide insights into processes controlling hyporheic flow as a limiting case, similarly as in previous studies on streambeds (Cardenas and Wilson, 2007b).

Parameters

The values of parameters prescribed in the model are listed in Table 3.1. The permeability k was manually calibrated at medium flow rate for both systems by comparing simulated and measured tracer data. The obtained value (1.4e–9 m^2) is close to an experimentally determined value (1e–9 m^2) for glass beads of the same diameter ($\overline{d}_p$ = 1 mm) with a porosity of 0.4 (Gioia et al., 2003).

Table 3.1 Parameter setup

Parameter		Value	Unit	Notes
Porosity		0.4	[-]	Measurement
Permeability k		1.4e–9	m^2	Calibration
Dispersion coefficient in conduit		1e–4	m^2/s	Tracer test
Dispersivity in sediments	α_L	3e–3	m	Calibration
	α_{TH}	3e–4		
	α_{TV}	3e–5		
Tracer concentration		1	g/l	
Initial volume		220	µl	
D_e		2.5e–10	m^2/s	Calculation

Dispersion in the conduit was characterized by carrying out pulse tracer test and fitting the observed breakthrough-curves (BTCs) with CXTFIT (Toride et al., 1995). The in-conduit impulse tracer tests were presented in detail in Appendix b. Dispersion coefficients ranging from 1e–4 m^2/s to 1e–3 m^2/s were obtained for flow velocities between 0.01 m/s and 0.1 m/s. Sensitivity tests showed that dispersion coefficients within range of 1e–5 m^2/s to 1e–3 m^2/s had no significant effect on the BTCs of sediment-source tracer tests. A value of 1e–4 m^2/s was specified for all model runs. Dispersion coefficients in sediments were determined by calibration. Values for longitudinal dispersivity were varied within a range of values from 0.1 to 1 cm (Xu and Eckstein, 1997), which are typical for lab-scale experiments (Zheng and Bennett, 2002). Horizontal transverse dispersivity α_{TH} was set to 1/10 of the α_L (Cardenas et al., 2008; Fetter, 1993) and vertical transverse dispersitivy α_{TV} to 1/10 of α_{TH} (Zheng and Bennett, 2002). The effective diffusion coefficient D_e was calculated by method of Othmer and Thakar (1953). Immediately after injection, the tracer volume expanded to approximately 220 µl as indicated by visual observation. Hence, a spheroid tracer volume of 220 µl with a concentration of 1 g/l was imposed as initial condition. The sensitivity tests of simulated BTC to main parameters were shown in Appendix a, Fig. A3 and Fig. A4.

Numerical approach

Three-dimensional simulation was necessary to describe the initial tracer distribution and the secondary flow in transverse direction of the conduit. A comparison between simulations of the full pipe and half sections with a vertical plane across the center of the tube as symmetrical boundary gave equivalent results. Therefore, the latter approach was chosen to reduce computation time. In the conduit flow domain, the walls of the tube and the SWI were specified as no-slip condition. At the conduit inlet a constant mean flow velocity was specified and at the conduits outlet a pressure of zero as the water exits to the atmosphere. Conduit flow and flow in the sediments were coupled by imposing the pressure field at the SWI from the conduit flow domain to the sediment flow domain. The walls of the tube in contact with the sediment were specified as no-flow boundaries.

The model was discretized using tetrahedral elements, with a mesh size of 2 mm for the conduit flow domain and 1 mm for the sediment domain. Boundary layers were meshed with four layers of prism elements, with a total thickness of about 0.27 mm along the conduit wall and SWI. The dense meshes better resolves the large velocity gradients across the SWI. The total meshing resulted in more than 200,000 elements. With this mesh, stable numerical solutions were obtained and mass balance errors remained below 0.2%.

The numerical solutions for the sets of partial differential equations were obtained using nonlinear iterative solvers in COMSOL multi-physics, which is widely used to resolve flow related issues (Cardenas and Wilson, 2006; Cardenas and Wilson, 2007b; Cardenas et al., 2008; Joodi et al., 2010; Karwan and Saiers, 2012; Shavit et al., 2004). The implicit backward differential formulas (BDF) were used as time dependent solver, which give less oscillation.

3.3 RESULTS AND DISCUSSION

3.3.1 Flow regimes and tracer test results

By observation of tracer movement, flow rates at which the flow regime changes were determined both upstream and downstream of the sediments and converted to Reynolds number *Re* representing flow dynamics. Laminar flow was identified by the presence of continuous streamlines parallel to the conduit wall, transitional flow by the onset of a wavering motion of the tracer filament, and turbulent flow by the loss of distinct tracer filaments (Appendix a, Fig. A2). In the 45D system (downstream), the transition from laminar to transitional flow occurs at *Re* = 380 and from transitional to turbulent flow at *Re* = 980 (Table 3.2). In the 15D system, the change in the flow regime takes place at higher values, *Re* = 590 and *Re* = 1090, respectively. For both systems, critical *Re* numbers are smaller downstream from the sediments than upstream. The critical *Re* numbers are lower than values previously observed for curved tube (1300 for *H* = 1.7 cm (Eustice, 1911)) or straight tubes (1700–2300, (Avila et al., 2011)). Our results demonstrate that a larger conduit curvature and the presence of sediments favor the onset of turbulent flow.

Table 3.2 Critical Reynolds number

		Critical value laminar to transitional flow [-]	Critical values transitional to turbulent flow [-]
45D	Downstream	380	980
	Upstream	590	1460
15D	Downstream	590	1090
	Upstream	880	1470

Tracer patterns from the sediment-source tracer test are illustrated for the 15D system at transitional flow (*Re* = 1000) as an example (Fig. 3.2, left column). The tracer plume is moving downstream horizontally after injection. It elongates and deforms with the upper part travelling faster

than the lower part. Before reaching the downstream end of the sediments, the tracer plume stagnates, enlarges laterally (not visible in Fig. 3.2) and depletes. The point where the tracer plume stagnates is located further upstream at higher flow rate.

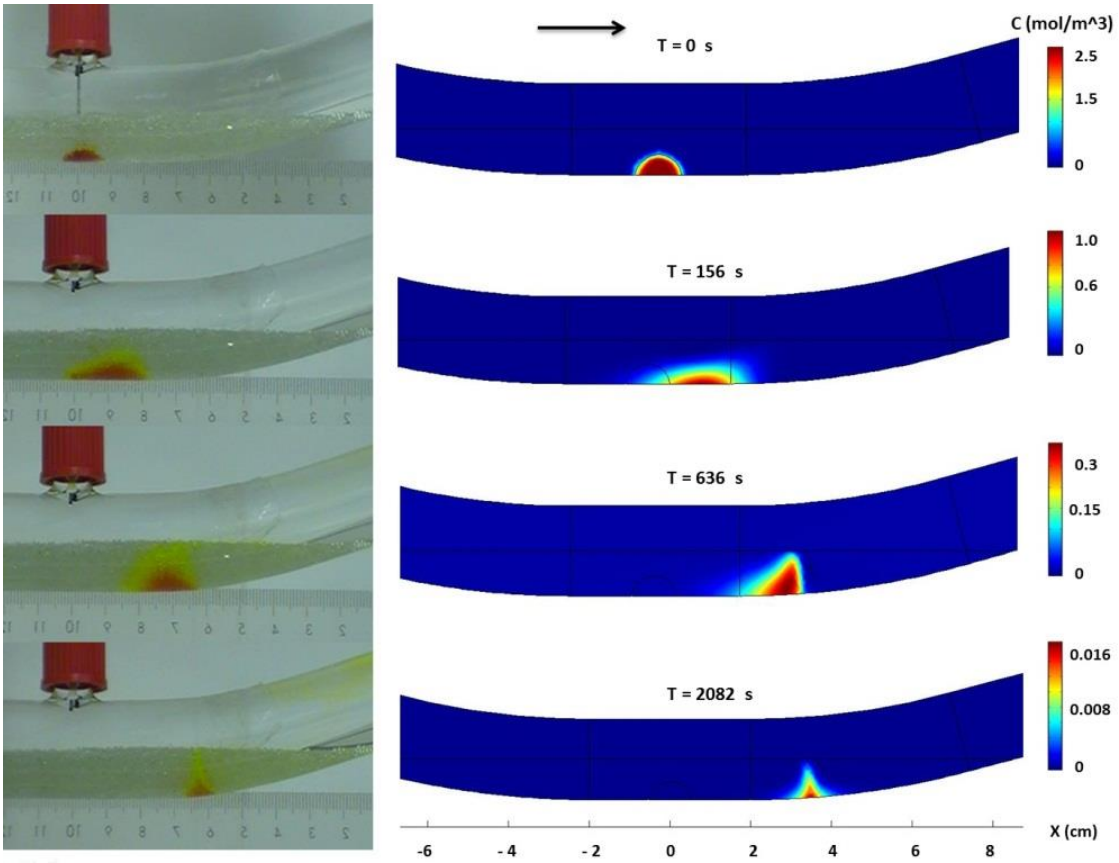

Fig. 3.2 Tracer pattern in 15D system. Left: time-lapse snapshot, right: simulation of solute concentration at a conduit Reynolds number of 1000

Breakthrough curves (BTCs) of the sediment-source tracer tests are presented in Fig. 3.3a. The mean travel time (MTT) and variance of the travel time (σ^2) is summarized for all experiments in Fig. 3.4. The time is non-dimensionalised by dividing it by the time required to renew the conduit volume. The concentration is normalized by dividing it by the injected tracer mass. The information on flow conditions of the tracer tests is presented in Appendix a, Table A1. The BTCs are smoother at low and high flow rates than at intermediate flow rates. The higher the conduit flow rate, the faster solutes are transported from sediments back into the conduit (Fig. 3.3a and Fig. 3.4). Furthermore, at high flow rates the BTCs are steeper and the peak concentrations are higher than at low flow rates (Fig. 3.3a). The MTT and σ^2 is generally higher for 15D system than for the 45D. The effect is particularly large at low flow conditions, e.g., with a MTT twice as long for the 15D system and a peak concentration half as high at Re = 200, but vanished at high Re. The factors contributing to these trends will be further explored in Sections 3.3.4 and 3.3.5 using the numerical model.

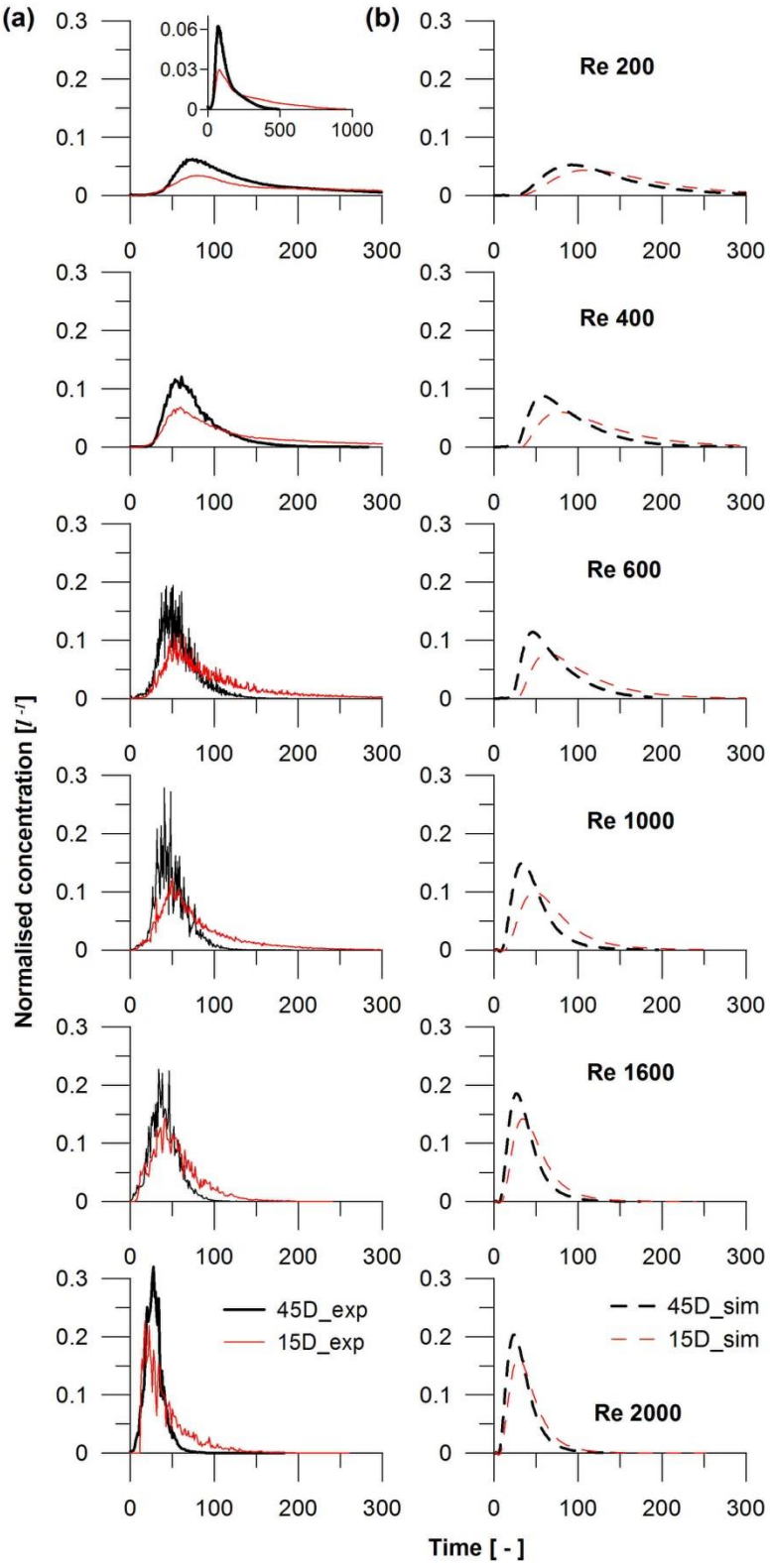

Fig. 3.3 Experimental (a) and simulated (b) breakthrough curves of sediment-source tracer tests

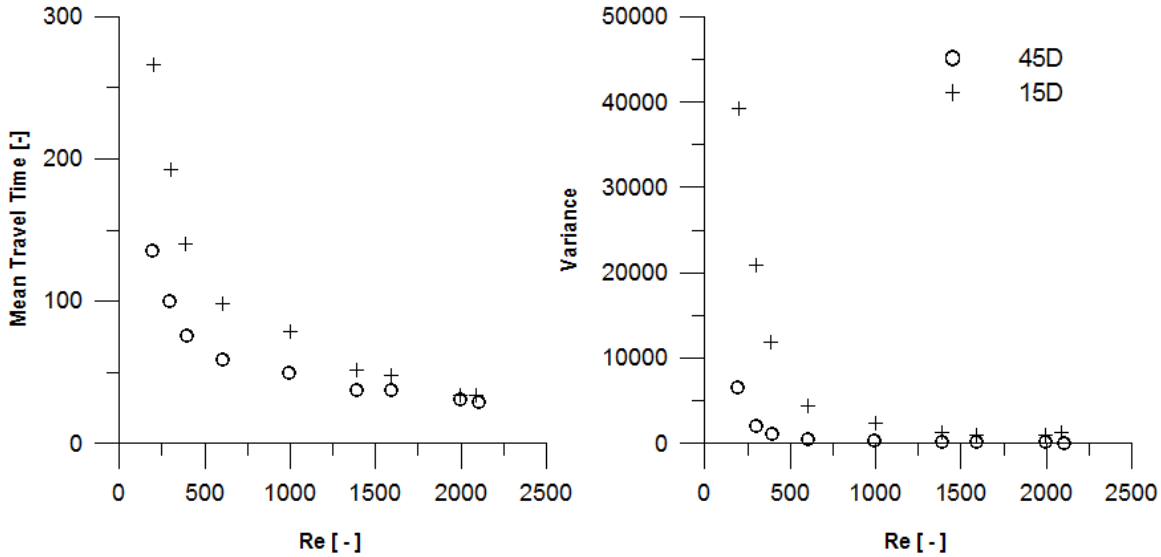

Fig. 3.4 Relationship of mean travel time and variance with Conduit Reynolds (Re) number

3.3.2 Numerical simulation

The simulated tracer plume is shown in Fig. 3.2 right column for transitional flow (*Re* = 1000) in the 15D system. The simulation captures well the main features of the tracer migration, especially the observation that the tracer plume stagnates and depletes before reaching the downstream end of the sediments. This is confirmed by the generally good agreement between measured (Fig. 3.3a) and simulated (Fig. 3.3b) BTCs. To evaluate the model efficiency in more detail, the Nash–Sutcliffe efficiency (NSE) (Xu and Eckstein, 1997) were quantified (Table 3.3). The NSE ranges from $-\infty$ to 1, whereby a value of 1 indicates a perfect model fit. The NSE values varied between 0.74 and 0.95 confirming a good model fit, except for experiments in the 15D system at very low (*Re* = 202) or very high low rates (*Re* = 1994), where values of 0.13 and 0.31, respectively were obtained. The generally good agreement between measured and modeled BTCs, and the good match between observed and modeled tracer patterns indicates that the model captures the main features of the flow patterns in the sediments well. Therefore, the model results are used to evaluate the driving force of hyporheic flow, the flow field and the hyporheic exchange flux in more details.

Table 3.3 Evaluation on mean travel time and model efficiency

	Re	MTT_exp [-]	MTT_sim [-]	NSE
45D	194	136	123	0.95
	397	76	83	0.94
	601	59	65	0.74
	993	50	48	0.74
	1589	38	37	0.78
	1995	31	34	0.84
15D	202	266	177	0.13
	390	140	114	0.88
	602	98	92	0.86
	997	79	70	0.95
	1592	48	47	0.85
	1994	34	42	0.31

3.3.3 Pressure distribution

Pressure gradients are the driving force for exchange processes between the free flow and sediment domain (Janssen et al., 2012). Fig. 3.5 illustrates the simulated pressure distribution in the water-sediment system under varied conduit *Re* for the 45D system. The pressure decreases from upstream to downstream, which exerts a distinct strong pressure gradient along the SWI at the upstream bend. Near the downstream region, a higher pressure zone appears at the outer wall of the tube, which intensifies with increasing flow rate (Fig. 3.5). The high pressure zone originates from the direction of flow towards the outer wall in the downsteam bend. The higher pressure zone leads to a reverse pressure gradient in longitudinal direction in the downstream part of the SWI, which drives the reverse flow in this part of the sediment. In addition, it creates a pressure gradient in transverse direction across the tube from outer to inner wall. The transverse pressure gradient leads to a secondary flow motion in the conduits in the form of two counter-rotating cells, known as Dean's flow (Appendix a, Fig. A5 and Fig. A6), as confirmed by tracer tests (Appendix a, Fig. A2d). Due to the secondary flow, tracer filaments originating from the sediments migrate downstream in spiral form (Appendix a, Fig. A2d), which could lead to the fluctuating concentrations at the outlet.

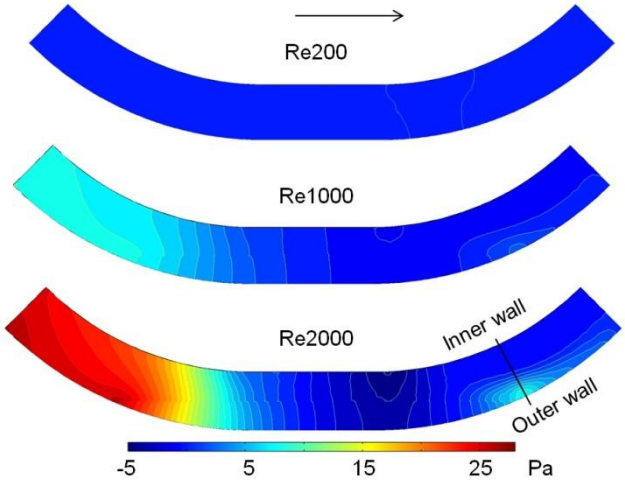

Fig. 3.5 Pressure distribution at different conduit Reynolds number

3.3.4 Flow fields in sediment

Flow fields are of key interest as they control the residence time distribution (RTD) of solute in sediments. To illustrate the effect of conduit hydraulics on the transport process in conduit and sediment, the flow fields at laminar, transitional and turbulent regimes are presented in Fig. 3.6 for the two systems. The conduit flow velocity exhibits a parabolic profile, with velocities several orders of magnitude higher than in the porous media (Appendix a, Fig. A5). Independent of the flow rate, a zone with forward and a zone with reverse flow can be observed (Fig. 3.6) consistent with the results of the tracer tests (Fig. 3.2). The reverse flow zone extends further upstream with increasing conduit *Re* due to the intensified reverse pressure gradient (see Section 3.3.3). Within the zone of forward flow, the velocity fields vary as function of flow rate. At a low flow rate, the flow lines are nearly horizontal between the zones where flow enters and exits from the sediments. At higher flow rate, a pronounced upward flow component appears earlier and flow exits already before reaching the point of flow separation.

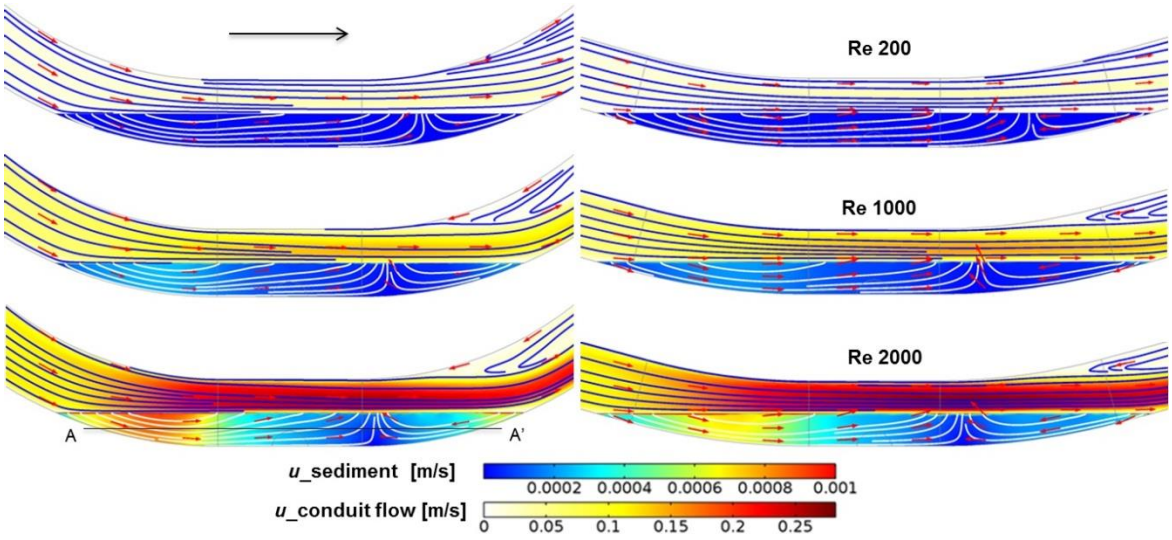

Fig. 3.6 Simulated streamlines and velocity magnitude, Left: 45D system; Right: 15D system

In order to explore the velocity field in more detail and relate it to the results of the sediment-source tracer test, the flow velocity at the depth where the center of mass of the tracer initially occurred is illustrated in Fig. 3.7. Independent of the angle of the system, the velocity magnitude is larger at higher *Re* consistent with the faster flushing out of the tracer at higher *Re* (Fig. 3.4). Considering the zone of forward flow and comparing the two conduit angles for a given *Re*, a particularly large difference in the velocity magnitude can be observed at around -4 cm. For smaller *Re* (200, 1000), a higher velocity magnitude for the steeper conduits angle is still observable at the tracer injection point (x = 0 cm) consistent with the faster flushing of the tracer in the D45 compared to the D15 system. However, at *Re* = 2000, the two velocity profiles converge at around x = -2 cm in agreement with similar MTT in the tracer test for both conduit angles (Fig. 3.4). Considering the section with reverse flow, for all *Re*, the velocity magnitude is much larger for 45D compared to 15D. Hence, a steeper conduit angle mainly induces a stronger flushing of the sediment close to the bends but has less (low *Re*) or no (high *Re*) effect in the central part of the sediment.

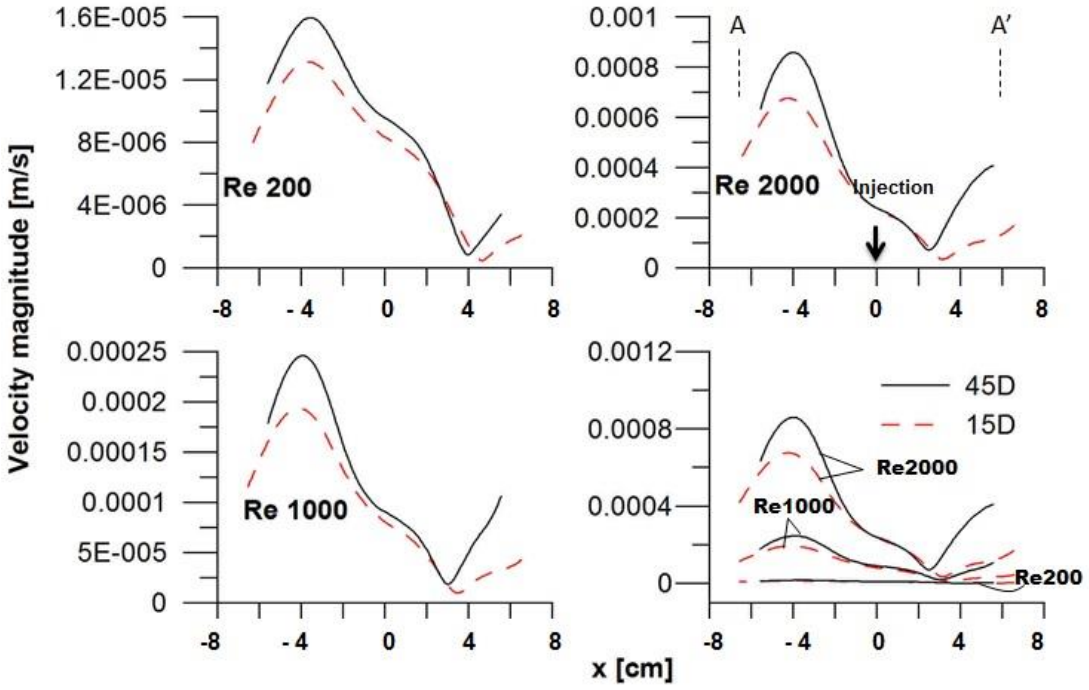

Fig. 3.7 Simulated velocity magnitude along profile AA' (marked in Fig. 6.) in sediment at different conduit Reynolds numbers

3.3.5 Hyporheic exchange flux

Finally, the effect of flow rate and conduit angle on the overall hyporheic exchange flux is explored. The exchange flux is obtained by integrating the normal flux across the SWI, dividing it by two as the in and out flux is equal. The obtained value is non-dimensionalised by dividing it by the conduit flux. For both conduit angles, the dimensionless exchange flux linearly increases with *Re* (Fig. 3.8). Previous studies on hyporheic flow induced by a triangular bedforms also observed a nearly linear increase with *Re* (Cardenas and Wilson, 2007a; Cardenas and Wilson, 2007b). The exchange

flux is higher for the steeper conduits angle due to the more intense flushing close to the two bends. For the steeper conduit, as much as 2% of the conduits flux transits through the sediment.

The hyporheic exchange in karst conduit has some implications on the interpretation of field tracer tests. Exchange between fast flow in conduit and slow flow in sediment could contribute to the long tailing of BTCs from in-conduit tracer tests (Field and Pinsky, 2000; Goppert and Goldscheider, 2008). However, in karst conduits, tailing can also occur during passage of tracers through pools as shown with laboratory analog models and computational fluid dynamics calculations by Hauns et al. (2001).

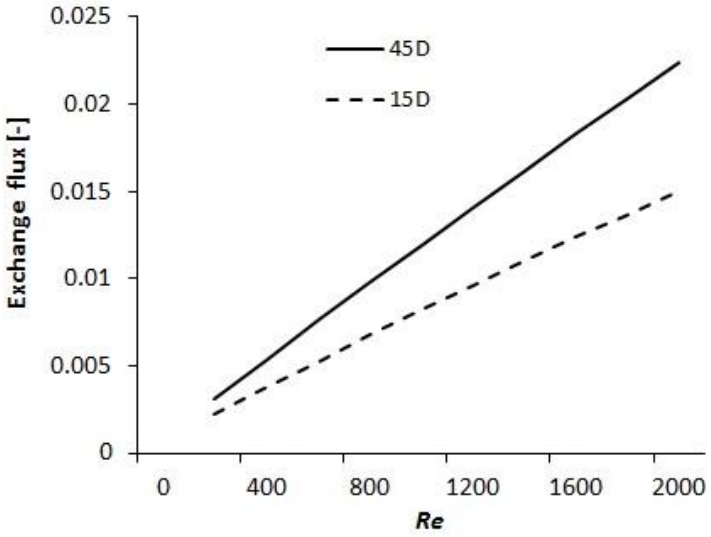

Fig. 3.8 Simulated exchange flux under varied conduit Reynolds number

3.4 SUMMARY AND CONCLUSIONS

The study demonstrates that in a sediment-filled bent conduit, strong hyporheic flow can be induced even for a flat sediment surface. Similarly as for hyporheic flow caused by irregular bedforms, zones with forward and reverse flow occur. Reverse flow originates from reverse pressure gradients caused by the downstream conduit bend. The general features of the flow field and the results from sediment-source tracer tests are reproduced fairly well with a two-domain numerical model with pressure continuity across the SWI. Based on the model, it is expected that the overall hyporheic flux increases with *Re* and is higher for a steeper conduit angle. However, a detailed analysis of the flow field indicates that the flushing intensity does not increase evenly throughout the sediments. Stronger flushing mainly occurs closer to the bends at high flow rate and steep conduit angle. In real systems, flow patterns in sediments are expected to be more complex due to the heterogeneity of karst sediments and more complex conduit geometries. The hyporheic flow through karst sediments could have a manifold influence on the fate of contaminants in karst system and biogeochemical processes in sediments. Contaminants travelling along conduits might become trapped, especially particle bound contaminants or microbial contaminants; soluble contaminants present in sediments such as

chlorinated hydrocarbon in form of DNAPLS might be released from sediments; or microbial processes might become enhanced by an input of dissolved organic matters into sediments.

While this study clearly highlights the potential for hyporheic flow in karst sediments, further studies are required to evaluate this phenomenon under different experimental conditions. The experimental conditions chosen in this study represent hyporheic flow through very permeable sediments under low flow conditions when sediments remain stable. In further studies, the effect of higher flow velocities, when sediments might become mobile, variable sediment permeabilities, different conduit geometries and different wall roughness should be addressed.

3.5 REFERENCES

Alazmi, B., Vafai, K., 2001. Analysis of fluid flow and heat transfer interfacial conditions between a porous medium and a fluid layer. International Journal of Heat and Mass Transfer, 44(9): 1735-1749.

Avila, K. et al., 2011. The onset of turbulence in pipe flow. Science, 333(6039): 192-196.

Beavers, G.S., Joseph, D.D., 1967. Boundary conditions at a naturally permeable wall. Journal of Fluid Mechanics, 30: 197-207.

Boulton, A.J., Findlay, S., Marmonier, P., Stanley, E.H., Valett, H.M., 1998. The functional significance of the hyporheic zone in streams and rivers. Annual Review of Ecology and Systematics, 29: 59-81.

Burnett, R.D., Frind, E.O., 1987. Simulation of contaminant transport in 3 dimensions .2. Dimensionality effects. Water Resources Research, 23(4): 695-705.

Cardenas, M.B., 2008. The effect of river bend morphology on flow and timescales of surface water-groundwater exchange across pointbars. Journal of Hydrology, 362(1-2): 134-141.

Cardenas, M.B., Gooseff, M.N., 2008. Comparison of hyporheic exchange under covered and uncovered channels based on linked surface and groundwater flow simulations. Water Resources Research, 44(3).

Cardenas, M.B., Wilson, J.L., 2006. The influence of ambient groundwater discharge on exchange zones induced by current-bedform interactions. Journal of Hydrology, 331(1-2): 103-109.

Cardenas, M.B., Wilson, J.L., 2007a. Dunes, turbulent eddies, and interfacial exchange with permeable sediments. Water Resources Research, 43(8).

Cardenas, M.B., Wilson, J.L., 2007b. Hydrodynamics of coupled flow above and below a sediment-water interface with triangular bedforms. Advances in Water Resources, 30(3): 301-313.

Cardenas, M.B., Wilson, J.L., Haggerty, R., 2008. Residence time of bedform-driven hyporheic exchange. Advances in Water Resources, 31(10): 1382-1386.

Chanson, H., 1999. The hydraulics of open channel flow. Amold, London, UK.

Choe, K.Y. et al., 2004. Sediment-water exchange of total mercury and monomethyl mercury in the San Francisco Bay-Delta. Limnology and Oceanography, 49(5): 1512-1527.

Eustice, J., 1911. Experiments on stream-line motion in curved pipes. Proceedings of the Royal Society A- Mathematical Physical and Engineering Sciences, 85(576): 119-131.

Faulkner, J., Hu, B.X., Kish, S., Hua, F., 2009. Laboratory analog and numerical study of groundwater flow and solute transport in a karst aquifer with conduit and matrix domains. Journal of Contaminant Hydrology, 110(1-2): 34-44.

Fetter, C.W., 1993. Contaminant hydrogeology. Prentice-Hall, Upper Saddle River, New Jersey.

Field, M.S., Pinsky, P.F., 2000. A two-region nonequilibrium model for solute transport in solution conduits in karstic aquifers. Journal of Contaminant Hydrology, 44(3–4): 329-351.

Ford, D., Williams, P., 2007. Karst hydrologeology and geomorphology. Wiley, England.

Ford, D.C., Ewers, R.O., 1978. Development of limestone cave systems in dimensions of length and depth. Canadian Journal of Earth Sciences, 15(11): 1783-1798.

Gioia, F., Alfani, G., Andreutti, S., Murena, F., 2003. Oil mobility in a saturated water-wetted bed of glass beads. Journal of Hazardous Materials, 97(1-3): 315-327.

Gobin, D., Goyeau, B., 2008. Natural convection in partially porous media: a brief overview. International Journal of Numerical Methods for Heat & Fluid Flow, 18(3-4): 465-490.

Goppert, N., Goldscheider, N., 2008. Solute and colloid transport in karst conduits under low- and high-flow conditions. Ground Water, 46(1): 61-68.

Harvey, J.W., Fuller, C.C., 1998. Effect of enhanced manganese oxidation in the hyporheic zone on basin-scale geochemical mass balance. Water Resources Research, 34(4): 623-636.

Hauns, M., Jeannin, P.Y., Atteia, O., 2001. Dispersion, retardation and scale effect in tracer breakthrough curves in karst conduits. Journal of Hydrology, 241(3-4): 177-193.

Janssen, F. et al., 2012. A comparative experimental and multiphysics computational fluid dynamics study of coupled surface-subsurface flow in bed forms. Water Resources Research, 48.

Jimenez-Islas, H., Lopez-Isunza, F., Ochoa-Tapia, J.A., 1999. Natural convection in a cylindrical porous cavity with internal heat source: a numerical study with Brinkman-extended Darcy model. International Journal of Heat and Mass Transfer, 42(22): 4185-4195.

Joodi, A.S. et al., 2010. Development of a Darcy-Brinkman model to simulate water flow and tracer transport in a heterogeneous karstic aquifer (Val d'Orl,ans, France). Hydrogeology Journal, 18(2): 295-309.

Karwan, D.L., Saiers, J.E., 2012. Hyporheic exchange and streambed filtration of suspended particles. Water Resources Research, 48.

Lauriat, G., Prasad, V., 1987. Natural-convection in a vertical porous cavity - a numerical study for brinkman-extended darcy formulation. Journal of Heat Transfer-Transactions of the Asme, 109(3): 688-696.

Le Bars, M., Worster, M.G., 2006. Interfacial conditions between a pure fluid and a porous medium: implications for binary alloy solidification. Journal of Fluid Mechanics, 550: 149-173.

Li, G., Cheng, Y., Zhao, B., 2012. Analysis of the effect of the beavers-joseph interface condition on flow in karst conduits. Journal of the American Water Resources Association, 48(6): 1233-1240.

Li, G., Loper, D.E., Kung, R., 2008. Contaminant sequestration in karstic aquifers: Experiments and quantification. Water Resources Research, 44(2).

Liu, Q., Prosperetti, A., 2011. Pressure-driven flow in a channel with porous walls. Journal of Fluid Mechanics, 679: 77-100.

Loop, C.M., White, W.B., 2001. A conceptual model for DNAPL transport in karst ground water basins. Ground Water, 39(1): 119-127.

Mermillod-Blondin, F., Des Chatelliers, M.C., Marmonier, P., Dole-Olivier, M.J., 2000. Distribution of solutes, microbes and invertebrates in river sediments along a riffle-pool-riffle sequence. Freshwater Biology, 44(2): 255-269.

Mermillod-Blondin, F. et al., 2004. Relative influence of bioturbation and predation on organic matter processing in river sediments: a microcosm experiment. Freshwater Biology, 49(7): 895-912.

Milanovic, S., 2007. Hydrogeological characteristics of some deep siphonal springs in Serbia and Montenegro karst. Environmental Geology, 51(5): 755-759.

Neale, G.H., Nader, W.K., 1974. Prediction of transport processes within porous-media-creeping flow relative to a fixed swarm of spherical-particles. Aiche Journal, 20(3): 530-538.

Othmer, D.F., Thakar, M.S., 1953. Correlating diffusion coefficients in liquids. Industrial and Engineering Chemistry, 45(3): 589-593.

Packman, A.I., Brooks, N.H., 2001. Hyporheic exchange of solutes and colloids with moving bed forms. Water Resources Research, 37(10): 2591-2605.

Pronk, M., Goldscheider, N., Zopfi, J., 2006. Dynamics and interaction of organic carbon, turbidity and bacteria in a karst aquifer system. Hydrogeology Journal, 14(4): 473-484.

Pronk, M., Goldscheider, N., Zopfi, J., 2007. Particle-size distribution as indicator for fecal bacteria contamination of drinking water from karst springs. Environmental Science & Technology, 41(24): 8400-8405.

Saffman, P.G., 1971. Boundary condition at surface of a porous medium. Studies in Applied Mathematics, 50(2): 93-&.

Santos, I.R., Eyre, B.D., Huettel, M., 2012. The driving forces of porewater and groundwater flow in permeable coastal sediments: A review. Estuarine Coastal and Shelf Science, 98: 1-15.

Sawyer, A.H., Cardenas, M.B., Buttles, J., 2011. Hyporheic exchange due to channel-spanning logs. Water Resources Research, 47.

Shavit, U., Rosenzweig, R., Assouline, S., 2004. Free flow at the interface of porous surfaces: A generalization of the Taylor brush configuration. Transport in Porous Media, 54(3): 345-360.

Thibodeaux, L.J., Boyle, J.D., 1987. Bedform-generated convective-transport in bottom sediment. Nature, 325(6102): 341-343.

Toride, N., Leij, F.J., M.T., G.v., 1995. The CXTFIT code for estimating transport parameters from laboratory or field tracer experiments. Research Report No. 137, US Salinity Laboratory, USDA, ARS, Riverside, California.

Tritton, D.J., 1988. Physical fluid dynamics. Oxford Science Publication, Oxford.

Vervier, P., Dobson, M., Pinay, G., 1993. Role of interaction zones between surface and ground waters in doc transport and processing - considerations for river restoration. Freshwater Biology, 29(2): 275-284.

Vesper, D.J., White, W.B., 2003. Metal transport to karst springs during storm flow: an example from Fort Campbell, Kentucky/Tennessee, USA. Journal of Hydrology, 276(1-4): 20-36.

Xu, M., Eckstein, Y., 1997. Statistical analysis of the relationships between dispersivity and other physical properties of porous media. Hydrogeology Journal, 5(4): 4-20.

Zhang, Y., Wu, R.S.S., Hong, H.S., Poon, K.F., Lam, M.H.W., 2000. Field study on desorption rates of polynuclear aromatic hydrocarbons from contaminated marine sediment. Environmental Toxicology and Chemistry, 19(10): 2431-2435.

Zheng, C., Bennett, G.D., 2002. Applied contaminant transport modeling. Wiley interscience, New York.

Zoumis, T., Schmidt, A., Grigorova, L., Calmano, W., 2001. Contaminants in sediments: remobilisation and demobilisation. Science of the Total Environment, 266(1-3): 195-202.

Chapter 4

Effect of sediment properties on hyporheic exchange

ABSTRACT

It is generally accepted by the scientific community that hyporheic flow plays an important role in surface and subsurface interactions. There have been numerous studies dedicated to hyporheic flow in surface water bodies due to its significance for benthic ecological system. In contrast, hyporheic exchange in karst conduits has received little attention so far despite its potential importance for the fate of contaminants. In Chapter 3, hyporheic exchange in a karst conduit-sediment system was investigated using a laboratory analog model for different flow conditions and conduit angles. In this chapter influence of sediment characteristics on hyporheic exchange was studied, and compared to the effect of other factors. Three different sediment materials were used with different gain size and shape. Sediment-source tracer tests were carried out to probe the flow field in the sediments. Numerical simulations were employed to explore hyporheic exchange in more detail. For all sediments, a zone of forward and reverse flow occurred in the sediments as indicated by the tracer tests and numerical simulations. The mean travel time (MTT) and variance (σ^2) of the injected tracer plume increased with the decrease of sediment grain size/permeability. The simulated flow patterns in the sediment were independent of sediment properties, while the magnitude of flow increased with increasing permeability. In comparison to the sediment permeability, the conduit flow rate and conduit angle had a weaker influence on the hyporheic exchange rate. In summary, the study demonstrates that the magnitude of hyporheic exchange strongly depends on sediment characteristics.

4.1 INTRODUCTION

Hyporheic exchange in streambed sediments has been widely investigated since several decades due to its significant role on benthic ecology and water chemistry (Cardenas and Wilson, 2007; Hancock et al., 2005). Although the hyporheic exchange in karst settings has received little attention so far (Koski and Wilson, 2009), some field studies suggest that it could have an effect on nutrients cycling (He et al., 2010), karst groundwater ecology (Gunn et al., 2000) and self-purification in karst aquifers (Iker et al., 2010; Morasch, 2013; Wilhartitz et al., 2009). Hence, karst hyporheic exchange is a fundamental process that needs to be explored for a better understanding of the occurrence and attenuation of contaminants in karst aquifer.

The large amount of clastic sediments present in karst conduit has been recognized to have intimate relationship with the fate of contaminants in karst aquifer (Herman et al., 2012; Schroeder and Ford, 1983). Sediments are transported to their place of deposition by means of sinking streams, soil wash-down from the epikarst, and residual insoluble material from the dissolution of limestone. In the karst developed in old carbonate rock, clastic sediments usually form a permeable medium encapsulated by the impermeable limestone matrix. Using a scaled model, karst hyporheic flow has been confirmed to occur in a closed karst conduit by hydraulic coupling between the conduit flow and sediment domains (Chapter 3). The pressure field caused by the flowing fluid along the sediment/water interface (SWI) was identified to drive fluid flow from the conduit into sediment. Conduit geometry/angle was shown to play a role in the hyporheic flow exchange and transport of sediment-born solutes.

Sediment properties are one of the key factors that determining the hyporheic exchange rate in streambeds, in addition to the flow rate (Elliott and Brooks, 1997a; Elliott and Brooks, 1997b; Eylers et al., 1995; Marion et al., 2002; Marion et al., 2003; Nagaoka and Ohgaki, 1990; Packman et al., 2004). While the effect of the conduit flow rate and conduit angle on hyporheic exchange have been investigated in the previous chapter, the following chapter is devoted to the effect of sediment properties on karst hyporheic flow in conduits. Sediment-source tracer tests and numerical modeling for sediments representing different grain size and material were carried out. In addition, the overall hyporheic exchange flux under varied flow rates for different sediments and conduit angle was calculated. Based on these studies, the relative roles of conduit flow, sediment properties and conduit angle on the exchange flux will be evaluated.

4.2 METHODS

4.2.1 Experimental setup and material

The experimental setup and procedures were same as presented in Chapter 3, except for the sediment material. In order to investigate the role of sediments on hyporheic exchange and solute transport, three types of sediments with different grain size and material were used, including coarse (1

mm) glass beads, fine (0.45 mm) glass beads and quartz sand (0.4–0.7 mm) (Table 4.1). The coarse glass beads correspond to the material used in experiments presented Chapter 3.

Table 4.1 Information on sediments and simulated exchange flux

	Diameter ϕ (mm)	Permeability k (m^2)	Porosity ε	Exchange flux q_{int} [-]
Coarse glass beads	1	1.4e–9	0.4	0.24–2%
Medium Quartz sand	0.4–0.7	4e–10	0.38	0.06–0.4%
Fine glass beads	0.4	1.6e–10	0.39	0.02–0.18%

4.2.2 Tracer experiments and numerical simulation

In order to characterize and compare the flow fields and solute transport among different sediments, the sediment-source tracer tests were performed in the same manner as for the coarse beads (Chapter 3) by injecting a tracer solution into the bottom of the sediment via the central port 2 under different conduit flow rates. Conduit flow ranged from Re = 200 to Re = 1600 (Appendix a, Table A1) to ensure sediment stability. Similarly, the experimental processes were reproduced by numerical simulations, based on which the parameters such as sediment permeability and dispersivity were calibrated (Table 4.1). For all types of sediment, dispersivities in sediment were set as $\alpha_{TV} = 1/10\alpha_{TH} = 1/100\alpha_L$ = 3e–5 m. The modeling approach (calibration/validation) implemented for fine beads and medium quartz sand were the same as for the coarse beads (Chapter 3). While the sediment-source tracer tests provide insight into the flow field in the sediments, they do not represent the whole flow paths as the tracer was injected in the central part of the sediment pack (Fig. 3.1 in Chapter 3). Due to the small sediment volume (5.8% of the whole system), continuous tracer injection from the upstream inlet for quantifying the overall exchange flux is not feasible as implemented in surface hyporheic study (Elliott and Brooks, 1997a). Therefore, such tracer tests were carried out numerically by prescribing a constant concentration boundary (2 g/l, 2.66 mol/m^3) at the inlet of the conduit for simulations.

4.3 RESULTS

4.3.1 Tracer tests

Breakthrough curves (BTCs) observed at the outlet under flow representing conduit Re = 200, 1000, 1600 for each type of sediment in both the 15D and 45D system are shown in Fig. 4.1. The concentration was normalized by dividing it by the injected tracer mass. The shapes of BTCs were influenced by conduit flow rates and sediment properties. At higher conduits flow rates, the tracer breakthrough occurred earlier and was characterized by a sharper peak. Under the same conduit flow conditions, the tracer appeared earliest in coarse glass beads, followed by medium sand, and finally the

fine glass beads, indicating longer travel times with the decrease of grain size as expected. The peak concentration increased about 2–4 times from low (*Re* = 200) to high (*Re* = 1600) flow, and was 3–5 times higher in coarse beads than in fine beads. All tracer BTCs show faster transport and higher peak concentration in the 45D than the 15D system. The mean travel time (MTT) and variance of the travel time distribution (σ^2) were plotted as function of conduit Reynolds number for comparison among different sediments as shown in Fig. 4.2. At equal flow rate, dispersion in conduit is assumed to be the same among different sediments. Hence, the variance σ^2 mainly indicates dispersion of tracer plume traveling downstream among different sediments. Both the MTT and variance σ^2 decreased with the increase of conduit flow rate and sediment grain size/permeability. Independent of sediment materials, the MTT and σ^2 in both systems showed a trend to converge with increasing conduit *Re*. Additionally, a longer mean travel time and stronger dispersion of tracer plume occurred in the 15D than 45D system irrespective of sediment grains and conduit flow condition.

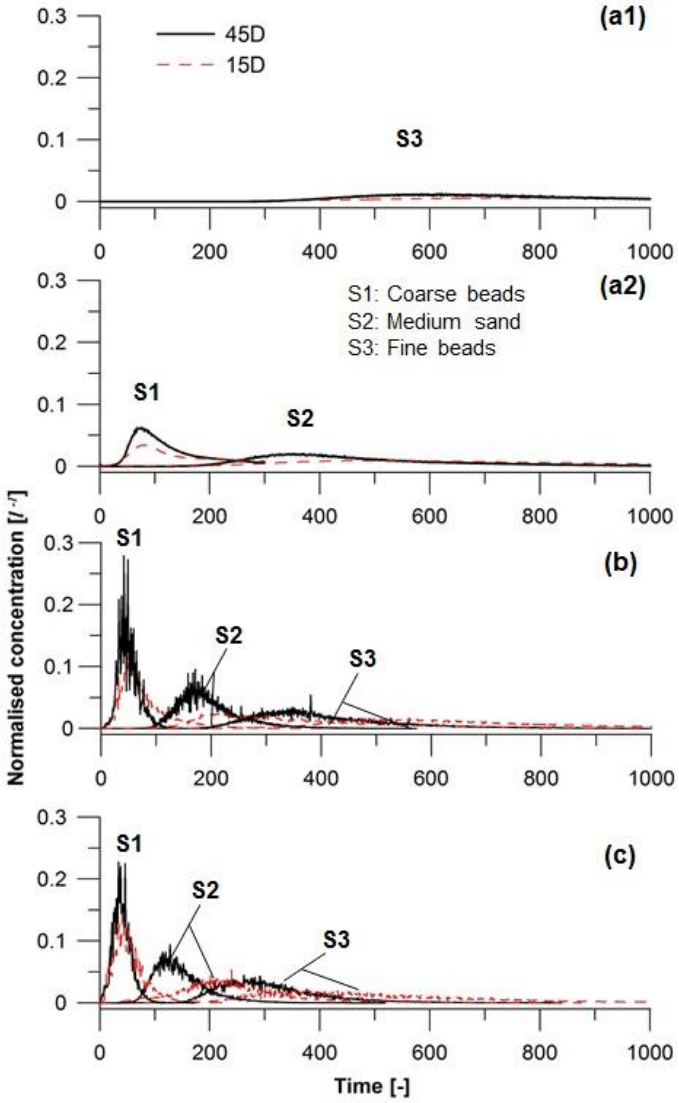

Fig. 4.1 Breakthrough curves for tracer tests in systems with 15 degree (15D) and 45 degree (45D) angles for different sediments and different flow conditions expressed as Reynolds number (Re). S1-Coarse glass beads; S2-Medium quartz sand; S3-Fine glass beads. (a1)(a2) conduit Re = 200, (b) Re = 1000, (c) Re = 1600

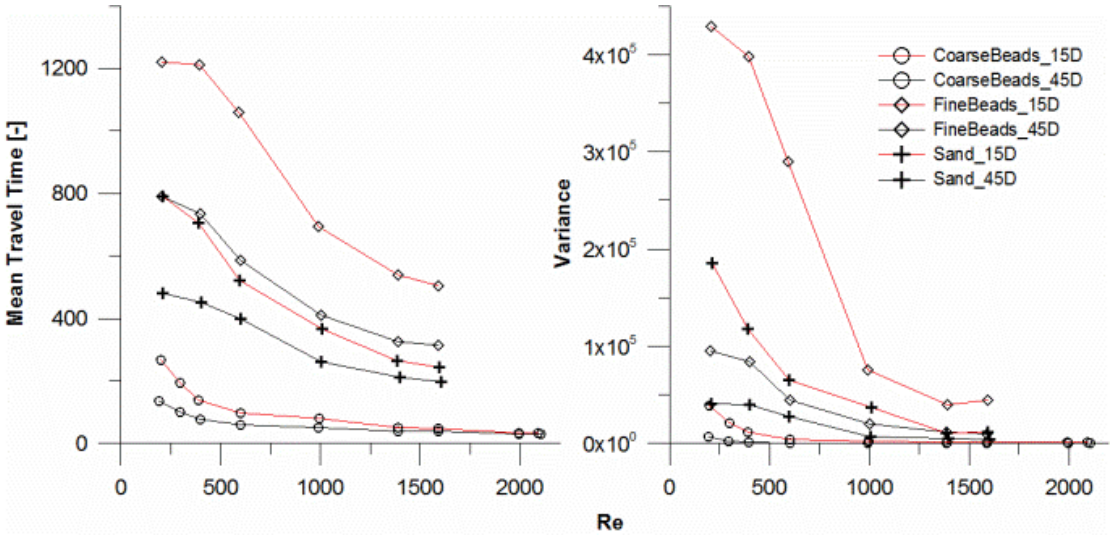

Fig. 4.2 Mean travel time and variance (σ^2) for different sediment at varied conduit Reynolds (Re) number.

As pointed out above, the hyporheic flow is dependent on the conduit flow rate, sediment properties, and conduit angle. However, these factors interact with each other. The ratios of MTT between 15D and 45D system were plotted as a function of conduit *Re* (Fig. 4.3), as a means to evaluate the relation of these controlling factors. A nearly linear relationship between the ratio and conduit *Re* was observed for larger grain size (coarse glass beads and medium quartz sand). In contrast, the ratio for fine beads shows no significant dependence on conduit *Re*. This indicates that the influence of the conduit angle on MTT depends on both the conduit flow rate and sediment grain size/permeability. For more permeable sediments, the conduit angle has a stronger effect on the MTT i.e. the flow velocity in the sediments.

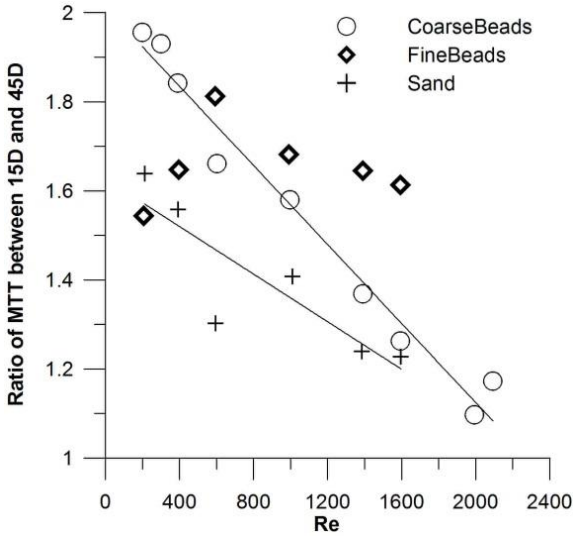

Fig. 4.3 The ratio of MTT between the two systems (15D/45D) at corresponding conduit Reynolds (Re) number.

4.3.2 Numerical tracer test

Additional numerical experiments were conducted to evaluate the overall exchange flux between conduit flow and sediment. The time-dependent images of tracer penetrating from a continuous source

at the inlet into different sediment at a conduit *Re* = 1000 in 45D system are shown in Fig. 4.4. The tracer penetrated the sediment not only at the upstream side but also at the downstream end. The tracer fronts were steadily advancing from both the two bend sides towards the flow dividing point, and eventually filled the whole sediment domain. The speed of penetration was faster for coarse beads than for sand and fine beads, reflecting the influence of permeability on flow velocity in sediment. Previous analyses of the flow fields (see Section 3.3.4 in Chapter 3) revealed a forward and reverse flow pattern in sediment, resulting from the reverse pressure gradient along the SWI. This explains why the tracer penetrated from both sides of the sediments. The downstream bend contributes to a backward flow motion in sediment, leading to an enhanced overall flow exchange between conduit and sediment.

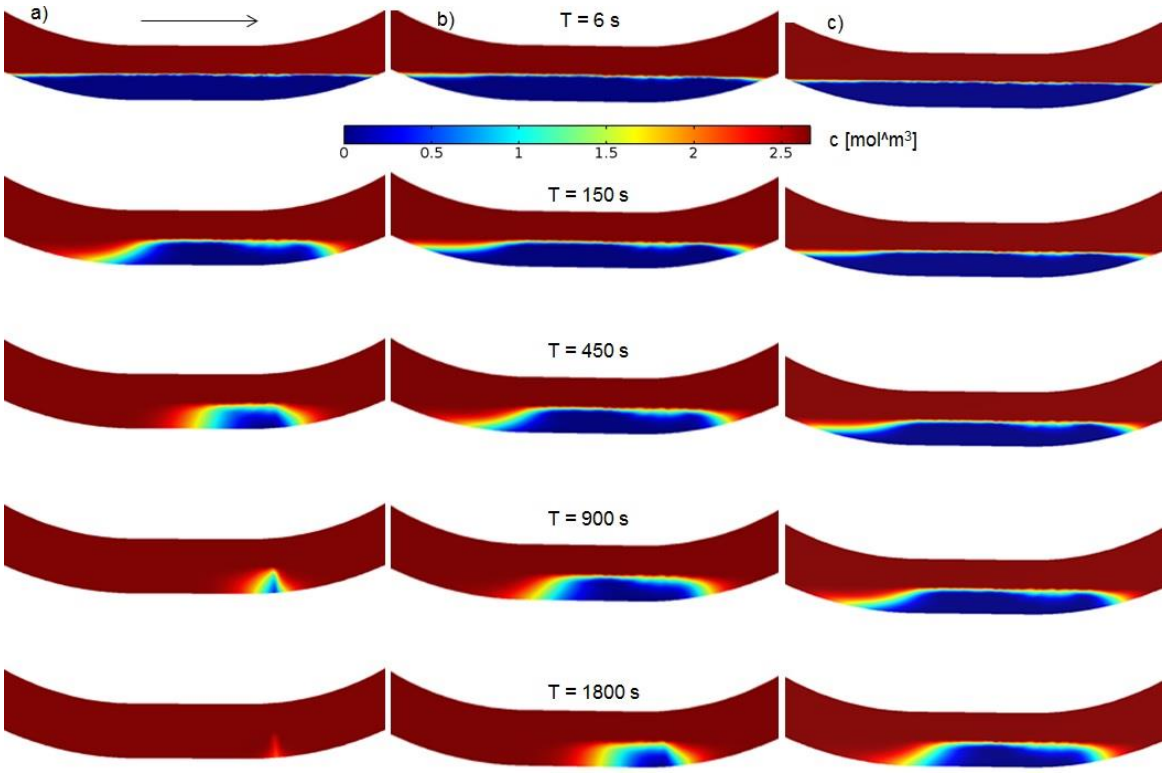

Fig. 4.4 Numerical tracer tests with inlet constant concentration for different sediments. a) Coarse beads, b) Medium sand c) Fine beads

To examine the temporal dynamics of the exchange flux in more detail, the time-dependent intruded mass is plotted. The intruded mass was normalized by dividing with final mass when tracer solution has filled the entire pore space of the sediments (Fig. 4.5). The time required to penetrate into the fine grain sediments was about 10 times longer than for the coarse grains. The turnover time scale of flow through sediments will influence sequestration and residence of contaminants in karst conduit aquifer.

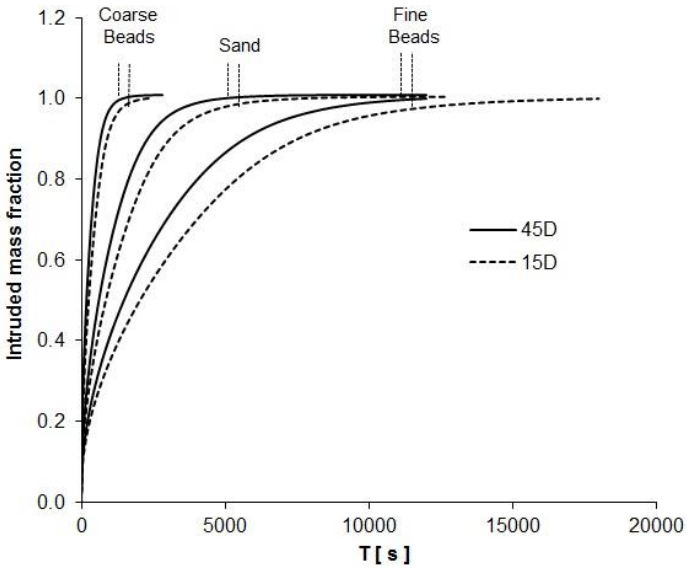

Fig. 4.5 Simulated time-dependent sequestered mass of solute in different sediment at conduit Re = 1000 in 45D and 15D system.

The exchange flux was shown above to vary among different sediments. In the following, flow patterns were simulated to investigate their dependence on sediment properties and conduit flow rate. Simulations of flow fields among different sediments are shown in Fig. 4.6. The flow pattern and especially the size of the zone of forward and reverse flow was similar for different sediments while magnitude of flow varied among sediments. Taking simulations at a conduit *Re* = 1000 for example, velocity magnitudes at a depth z = –0.5 cm in the sediment ranged (as velocity fields were quite non-uniform) from $1e^{-4}$ to $8e^{-4}$ m/s for coarse beads, $2.5e^{-5}$ to $2e^{-4}$ m/s for medium sand, and $1e^{-5}$ to $8e^{-5}$ m/s for fine beads. Both the sediment-source tracer tests and numerical simulations show that the length of the reverse flow zone changed as a function of conduit flow rate and conduit angle independent of sediment grain size/permeability. The same conduit flow and conduit angle led to the same pressure gradient along the SWI, resulting in the same flow patterns among different sediments. Flow velocities in sediments varied due to different sediment permeabilities, leading to different time scales of exchange flux.

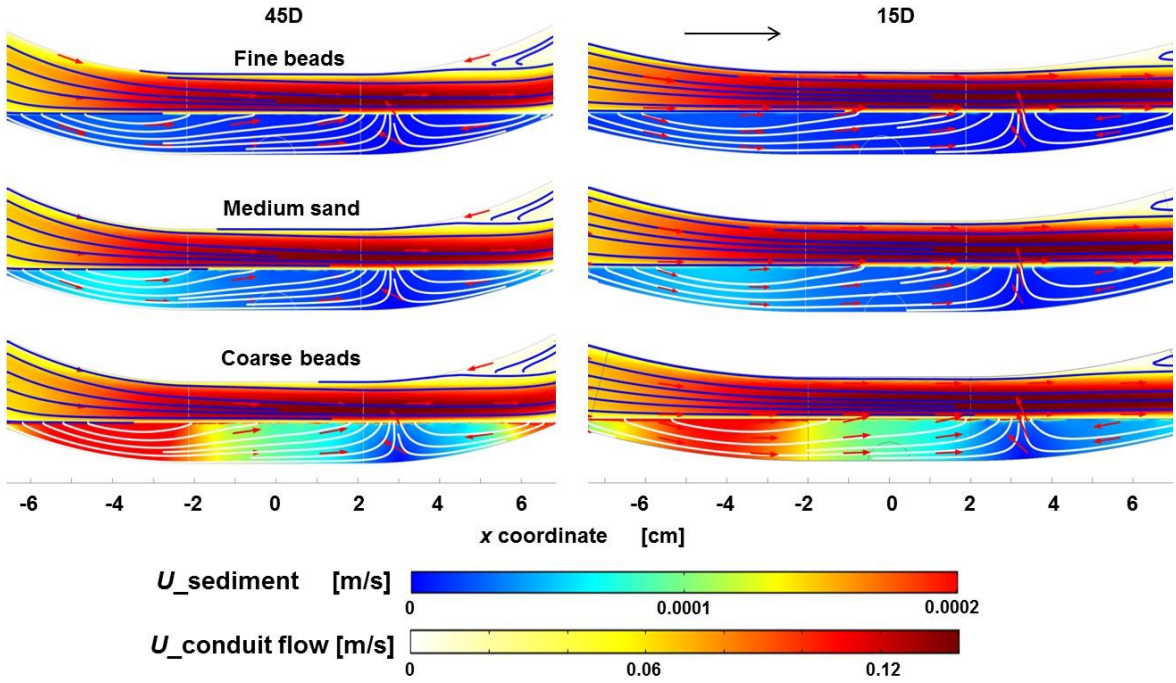

Fig. 4.6 Illustration of the same flow pattern in sediment independent of sediment permeability, taking the simulated flow fields at a conduit Reynolds number of 1000 for both conduit angles as an example.

4.3.3 Exchange rate

To evaluate the relative importance of conduit flow, sediment permeability and conduit angle on the exchange rate, relationships of the exchange flux and these factors were analyzed by numerical simulations. The dimensionless exchange flux q_{int} along the SWI corresponding to the ratio of flow passing through the sediment versus total flow through the conduits were calculated from numerical simulations (Table 4.1). The exchange flux ranged from low 0.02% (at conduit *Re* = 200) in fine beads to high 2% in coarse beads (at conduit *Re* = 2000).

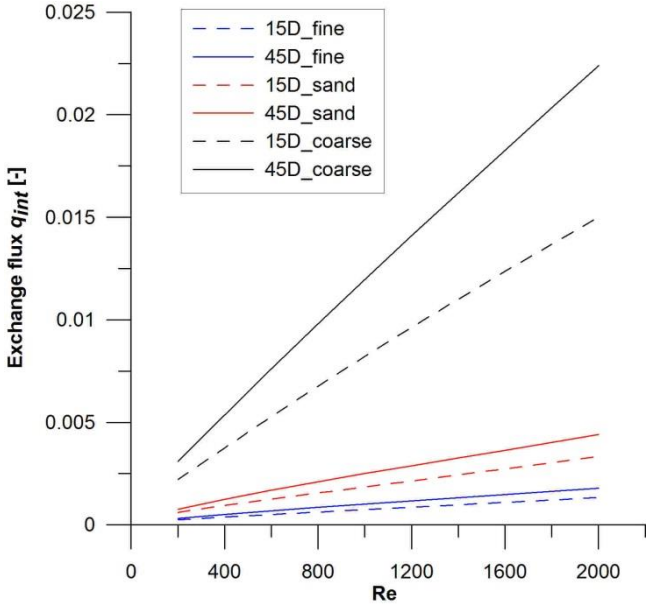

Fig. 4.7 Exchange flux as a function of conduit *Re* for different sediment

The relationships between the exchange flux and conduit *Re* for different sediments and both angles are shown in Fig. 4.7, which are all linear as found in the previous study for coarse beads. Independent of the sediment material, the exchange flux increases with the conduit flow rate and is higher in 45D than in 15D. Sediments of a higher permeability have larger q_{int} than less permeable material. The statistical analysis (Packman and Salehin, 2003) of experimental studies for hyporheic exchange in streambeds (Elliott and Brooks, 1997a; Eylers et al., 1995; Marion et al., 2002; Nagaoka and Ohgaki, 1990; Packman et al., 2004; Packman and Brooks, 2001) indicated that the exchange flux scaled with the square of Reynolds number (3000-80,000) irrespective of grain size and bedforms. Results of this study showed however that q_{int} varies linearly with *Re*. The different relationship might be caused by the different *Re* range and by the constrain flow in a saturated conduit. At low *Re*, the relationship might also be approximately linear for streambed studies.

Calculations of the increased exchange fluxes in response to the increased permeability, conduit *Re* and conduit angle showed the following relationships: $\Delta q_{int} \propto (1.36 +/- 0.2) \cdot (\Delta k/k_0)$, $\Delta q_{int} \propto (0.57 +/- 0.1) \cdot (\Delta Re/Re_0)$, $\Delta q_{int} \propto (0.14 +/- 0.01) \cdot (\Delta\theta/\theta_0)$, where Δq_{int} is the change in exchange flux, $(\Delta k/k_0)$, $(\Delta Re/Re_0)$, $(\Delta\theta/\theta_0)$ is the relative change of each factor. The values of proportionality from these relationships suggest that under the experimental flow conditions, sediment permeability has the strongest effect on the exchange flux. Influences of conduit flow velocity and conduit angle are less strong than sediment permeability.

4.3.4 Flow-regime dependent BTC fluctuation

Though not the main objective of the study, the BTC concentration fluctuations are discussed as it might be indicator of dispersive behaviors within the conduit and sediment system. Concentration variations, particularly at BTC peaks, were observed in tracer tests under medium flow rates (Fig. 4.8a), for which artifacts from measurement can be excluded. The BTC was in contrast smoother under low conduit flow (Fig. 4.8b). Concentration noise was calculated to evaluate the amplitude of variation using discrete Fourier transformation (DFT), which converts the time domain signal (the monitored BTCs) to the frequency domain. A low-pass filter was used to separate low-frequency signals from higher frequency noise. The noise of BTCs in different sediments at varying conduit flow rates are presented in Fig. 4.9. The noise generally increased with conduit flow rate (except for very high flow in coarse beads) and was higher in the 45D than 15D system. It was particularly high for coarse grain sediment at medium flow rate. A combining effect of conduit flow velocity and conduit angle on dispersive and mixing behavior was assumed to cause the fluctuations.

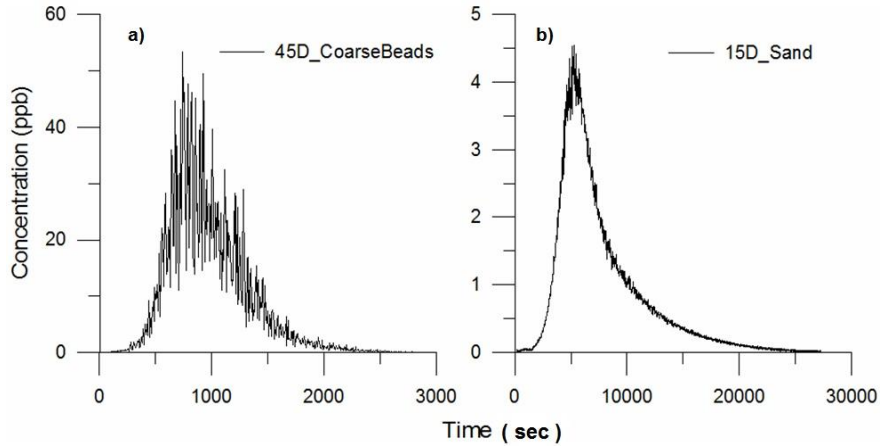

Fig. 4.8 Observed BTCs. Left a): conduit Re 1000; Right b): conduit Re200

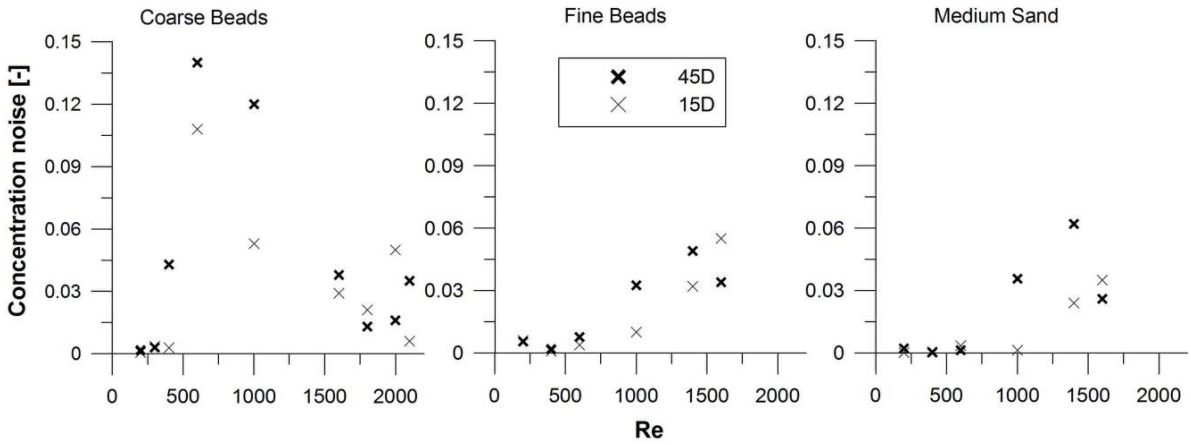

Fig. 4.9 Concentration noise of BTCs for different sediment at varied conduit flow calculated by DFT processing.

Conduit flow velocity affects dispersion when passing through curved bends. The parabolic velocity profile at low laminar flow regime favors apparent dispersion and mixing of solutes in conduit. However, as conduit flow velocity increases, secondary flow motion induced by centrifugal force tends to enhance transverse mixing and hence reduces the longitudinal dispersion (Erdogan, 1967; Jarrahi et al., 2011; Marion and Zaramella, 2006; McConalogue, 1970; Zhao and Bau, 2007), which is likely to lead to the concentration fluctuations of BTCs. Numerical simulations of flow field show clearly an enhanced secondary flow developing with conduit *Re* (Appendix a, Fig. A7). The secondary flow could also be observed to appear as spirals along the tube wall at conduit bend under medium flow during experiments, which proved less longitudinal mixing in conduit. Concentration fluctuations tends to reduce after the onset of turbulent flow (*Re*>1000), which might be attributed to turbulent mixing. However, the trend is sediment dependent, which is the case for coarse grains, not for medium and fine grains. While the mechanisms proposed could explain the experimental observations, influences of conduit flow velocity, conduit angle and sediment permeability on the BTC fluctuations still need further investigations.

4.4 SUMMARY AND CONCLUSIONS

The effect of sediment properties on hyporheic exchange was investigated by a laboratory analog model and numerical simulations. The relative roles of conduit flow, sediment permeability and conduit angle on the hyporheic exchange rate was evaluated by numerical tracer tests. Results of sediment-source tracer tests showed that both the MTT and variance σ^2 decreased with the increase of conduit flow rate and sediment grain size/permeability, and were smaller for the steeper conduit angle. Results of numerical tracer tests showed that flow patterns characterized by zones of forward and reverse flow were identical for the same conduit geometry and flow rate independent of sediment permeability. The same flow patterns were caused by the same pressure distribution along the SWI which depends only on the conduit geometry and flow rate. However, the magnitude of flow in the sediment was determined by sediment permeability for the same conduit flow and geometry. Based on the relationships established between exchange flux q_{int} and different controlling factors by numerical modeling, sediment permeability was identified to have the strongest influence on the exchange rate.

The study demonstrated that sediment properties had strong influence on the hyporheic exchange. Hence, hydrogeological condition (sediment properties) needs to be taken into account as well as flow condition for evaluating the effect of hyporheic flow on the fate of contaminants in karst aquifer. Less permeable sediment needs longer time to renew flow in the sediment, while it might provide more efficient contacting time for reaction processes.

4.5 REFERENCES

Cardenas, M.B., Wilson, J.L., 2007. Hydrodynamics of coupled flow above and below a sediment-water interface with triangular bedforms. Advances in Water Resources, 30(3): 301-313.

Elliott, A.H., Brooks, N.H., 1997a. Transfer of nonsorbing solutes to a streambed with bed forms: Laboratory experiments. Water Resources Research, 33(1): 137-151.

Elliott, A.H., Brooks, N.H., 1997b. Transfer of nonsorbing solutes to a streambed with bed forms: Theory. Water Resources Research, 33(1): 123-136.

Erdogan, M.E., 1967. Effect of secondary flow in a curved pipe on longitudinal dispersion. Journal of the Physical Society of Japan, 22(4): 1093-1101.

Eylers, H., Brooks, N.H., Morgan, J.J., 1995. Transport of adsorbing metals from stream water to a stationary sand-bed in a laboratory plume. Marine and Freshwater Research, 46(1): 209-214.

Gunn, J., Hardwick, P., Wood, P.J., 2000. The invertebrate community of the Peak-Speedwell cave system, Derbyshire, England pressures and considerations for conservation management. Aquat. Conserv.-Mar. Freshw. Ecosyst., 10(5): 353-369.

Hancock, P.J., Boulton, A.J., Humphreys, W.F., 2005. Aquifers and hyporheic zones: Towards an ecological understanding of groundwater. Hydrogeology Journal, 13(1): 98-111.

He, Q. et al., 2010. The use of nitrate, bacteria and fluorescent tracers to characterize groundwater recharge and contamination in a karst catchment, Chongqing, China. Hydrogeology Journal, 18(5): 1281-1289.

Herman, E., Toran, L., White, W., 2012. Clastic sediment transport and storage in fluviokarst aquifers: an essential component of karst hydrogeology. Carbonates and Evaporites, 27(3-4): 211-241.

Iker, B.C., Kambesis, P., Oehrle, S.A., Groves, C., Barton, H.A., 2010. Microbial atrazine breakdown in a karst groundwater system and its effect on ecosystem energetics. Journal of Environmental Quality, 39(2): 509-518.

Jarrahi, M., Castelain, C., Peerhossaini, H., 2011. Secondary flow patterns and mixing in laminar pulsating flow through a curved pipe. Experiments in Fluids, 50(6): 1539-1558.

Koski, K., Wilson, J.L., 2009. Is the hyporheic zone a useful concept for karst aquifers with conduits? Geol Soc Amer Abstr Programs, pp. 400.

Marion, A., Bellinello, M., Guymer, I., Packman, A., 2002. Effect of bed form geometry on the penetration of nonreactive solutes into a streambed. Water Resources Research, 38(10).

Marion, A., Bellinello, M., Guymer, I., Packman, A., 2003. Effect of bed form geometry on the penetration of nonreactive solutes into a stream bed (vol 39, art no 1209, 2002). Water Resources Research, 39(1).

Marion, A., Zaramella, M., 2006. Effects of velocity gradients and secondary flow on the dispersion of solutes in a meandering channel. Journal of Hydraulic Engineering-Asce, 132(12): 1295-1302.

McConalogue, D.J., 1970. The effects of secondary flow on the laminar dispersion of an injected substance in a curved tube. Proceedings of the Royal Society of London. Series A, Mathematical and Physical Sciences, 315(1520): 99-113.

Morasch, B., 2013. Occurrence and dynamics of micropollutants in a karst aquifer. Environ. Pollut., 173: 133-137.

Nagaoka, H., Ohgaki, S., 1990. Mass-transfer mechanism in a porous riverbed. Water Research, 24(4): 417-425.

Packman, A., Salehin, M., Zaramella, M., 2004. Hyporheic exchange with gravel beds: Basic hydrodynamic interactions and bedform-induced advective flows. Journal of Hydraulic Engineering-Asce, 130(7): 647-656.

Packman, A.I., Brooks, N.H., 2001. Hyporheic exchange of solutes and colloids with moving bed forms. Water Resources Research, 37(10): 2591-2605.

Packman, A.I., Salehin, M., 2003. Relative roles of stream flow and sediment conditions in controlling hyporheic exchange. Hydrobiologia, 494(1-3): 291-297.

Schroeder, J., Ford, D.C., 1983. Clastic sediments in castleguard cave, columbia icefields, alberta, canada. Arctic and Alpine Research, 15(4): 451-461.

Wilhartitz, I.C. et al., 2009. Heterotrophic prokaryotic production in ultraoligotrophic alpine karst aquifers and ecological implications. Fems Microbiology Ecology, 68(3): 287-299.

Zhao, H., Bau, H.H., 2007. Effect of secondary flows on Taylor-Aris dispersion. Analytical Chemistry, 79(20): 7792-7798.

Chapter 5

Experimental investigation of DNAPL dissolution

ABSTRACT

Organic contaminants in form of DNAPLs (Dense Non-aqueous Phase Liquids) constitute a long term contaminant source that can threaten the groundwater quality of karst aquifers. DNAPLs are likely entrapped in karst conduit sediment as pools due to the karst features and properties of DNAPLs. The lifetime of a DNAPL pool in karst conduits depends on the rate of water flow through the sediment. In this chapter, DNAPL dissolution facilitated by hyporheic exchange between conduit and sediment was investigated. Influences of conduit flow and conduit geometry/angle on the mass transfer rate were evaluated. A well-defined DNAPL pool was created in the same laboratory analog setup as used in the previous chapters to quantify the mass transfer rate of DNAPL compounds to the aqueous phase. The mass transfer processes and rates were compared to a reference scenario consisting of a DNAPL pool in a semi-infinite porous media that is well documented in the literature. Results showed that the mass transfer coefficient k_m increased with conduit flow rate and was higher for the steeper conduit angle. The relationship between the mass transfer coefficient k_m and the average groundwater flow velocity in the sediment was linear in both the experiments and the numerical model. However, the observed and model k_m for the sediments in the conduit was higher than the one calculated with an analytical expression for the semi-infinite porous media. Then higher k_m was likely caused by the hyporheic flow pattern which moved solute away from DNAPL surface. The conduit angle had an effect on k_m by influencing the average flow velocity in the sediment. Sensitivity analyses showed that the sediment permeability had the strongest influence on k_m. The study highlighted that higher mass transfer of DNAPL pool dissolution could occur in karst conduit sediment than in the semi-infinite porous medium due to the characteristics of hyporheic flow. Hence, a shorter lifetime of DNAPLs in karst conduit aquifer is to be expected.

5.1 INTRODUCTION

Dense Non-aqueous Phase Liquids (DNAPLs), especially chlorinated solvents, are among the most common groundwater organic contaminants. In karst research, a need for improved conceptual models for DNAPL behavior in karst aquifers has been recognized (White, 2002). Several studies have reported DNAPL contamination in karst aquifers (Crawford and Ulmer, 1994; Han and Wang, 2004; Jancin and Ebaugh, 2002; Mahler and Massei, 2007; Zhang et al., 2011). These studies show that it is difficult to locate DNAPLs in karst systems due to the heterogeneity of the aquifer. DNAPL-migration pathways and the DNAPL distribution in karst aquifer cannot be mapped routinely (Ewers et al., 2005). Hence in many cases it will not be possible to implement remediation methods. Then the question arises how long DNAPLs present in karst aquifers will contaminate a spring. In order to answer this question it needs to be known what controls the rate of DNAPL dissolution.

Interphase mass transfer limitations during DNAPL dissolution have a strong influence on the persistence of DNAPLs in the subsurface (Dickson and Thomson, 2003). The dissolution and mass transfer rate have been extensively investigated for DNAPL ganglia and pools in porous environment using laboratory experiments and numerical simulations (Anderson et al., 1992a; Anderson et al., 1992b; Chrysikopoulos, 1995; Chrysikopoulos et al., 2000; Imhoff et al., 1998; Johnson and Pankow, 1992; Kim and Chrysikopoulos, 1999; Miller et al., 1990; Powers et al., 1992; Powers et al., 1991). These studies show that the dissolution rate depends on source morphology. In a spill morphology that involves zones of residual saturation and pools, it will generally take substantially longer to dissolve pools than the mass present as residual saturation (Anderson et al., 1992b). As DNAPL pool surfaces are usually aligning parallel to the groundwater flow direction, mass transfer from the DNAPL pool to the water is slow leading to long-lasting groundwater contamination. While DNAPL dissolution processes are well understood for granular porous media, there is a lack of understanding of DNAPL dissolution processes in karst settings.

Conceptual models of DNAPL behavior in karst aquifer were presented in Chapter 1 (e.g. Fig.1.1 in Chapter 1). DNAPLs can enter karst aquifers via sinking streams and sinkholes or penetrate through regolith and rock interfaces. Accumulation of DNAPL in conduits is expected to be common as they constitute preferential pathways of DNAPL migration and particularly problematic since most water transits through conduits (Loop and White, 2001; Wolfe et al., 1997). DNAPLs might especially accumulate at low points of conduits which frequently also trap sediments. Hence, the scenario of DNAPLs trapped in the sediment of conduits is the main focus of this study (Fig. 1.1, Case 3 in Chapter 1).

For DNAPL pools entrapped in cave sediments, the dissolution rate will be strongly influenced by the rate at which water passes along the DNAPL surface. Hence, to understand DNAPL dissolution processes, water exchange processes between the conduit and sediments i.e. hyporheic flow needs to be understood. Hyporheic flow refers to the water exchange that occurs between sediments and the overlying water column of rivers and streams (Harvey et al., 1996; Orghidan, 1959). Recent studies

suggest that hyporheic flow likely occurs in karst sediments as indicated by the sequestration of metals (Munteanu et al., 2012) and organic compounds (Iker et al., 2010) in sediments. Moreover, the likely occurrence of karst hyporheic exchange has been confirmed using a laboratory analog model (Chapter 3). The study revealed that the exchange rate increased with conduit flow rate and was higher for a steeper conduit angle.

This study will focus on the dissolution of sediment-entrapped DNAPL pools mediated by hyporheic exchange between the conduit and sediment domains. As natural karst systems are complex and as there are hardly any sites where DNAPLs have been located and are accessible for study, a laboratory analog approach was used. Pool dissolution tests with a surrogate DANPL under varied conduit flow conditions were carried out. In addition, numerical modeling was used to explore the relationship between mass transfer rates and conduit flow conditions.

*5.*2 METHODS

5.2.1 Experimental setup and material

The same apparatus as presented in Chapter 3 was used for investigating the dissolution of DNAPL pools. The detailed description of the setup and motivation for studying such a conduit morphology were presented in Chapter 3. The experimental setup is shown in Fig. 5.1 and Appendix a, Fig. A7. Glass tubes with two conduit angle were used, 15° (denoted as 15D) and 45° (denoted as 45D) respectively. The sediments consisted of glass beads with a diameter of 0.4 mm. The effluent was circulated through the flow cell (path length 50 mm, internal volume 650 µL) of an ultraviolet-visible (UV-Vis) spectrum photometer using a small peristaltic pump and teflon tubing (I.D. 0.8*O.D.1.6 mm).

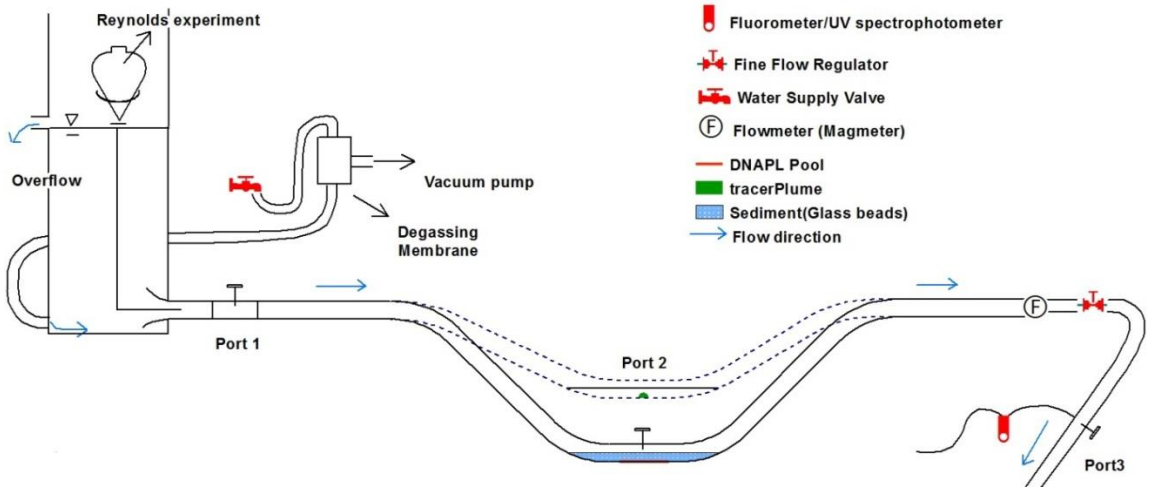

Fig. 5.1 Schematic diagram of experimental apparatus for sediment-source tracer tests and dissolution tests

Although chlorinated solvents are the most common DNAPLs found in karst systems, they were not used in this study due to their toxicity and due to their high interfacial tension that leads to the

formation of larger blobs that perturb the sediments. In this study, 2-methoxyphenol (Guaiacol, liquid 99+%, Acros Organics) was used to mimic the DNAPL dissolution. The physical and chemical properties of Guaiacol are shown in Table 5.1 (Boards, 1913). The density of liquid Guaiacol is also higher than water i.e. it is a DNAPL. The relatively high solubility compared to the common chlorinated solvents, for instance TCE (solubility 1100 mg/l), makes it possible to detect it continuously using UV-spectroscopy in the conduit where lower concentrations occur due to dilution. The compound can be easily solidified at room temperature which makes it possible to create relatively well-defined source zones for quantifying the dissolution rate.

Table 5.1 Physical and Chemical Properties of 2-methoxyphenol

Property		Unit
Colour	Colorless to pale yellow	
Density	1.12	g/cm^3
Molecular weight	124.14	g/mol
Vapor pressure	0.11	hPa
Melting/Freezing point	28-32	°C
Water solubility	17 g/l at 15 °C	
	15 g/l at 10 °C	

For visual observation purposes, the liquid was dyed with oil red O (< 5µg/l). In order to maintain a well-defined source of solutes and prevent its migration during the experiment, Guaiacol was used as a solid in the experiments.

5.2.2 DNAPL pool dissolution tests

The effect of conduit flow rate and conduit angle on the dissolution rate was investigated by dissolution experiments. The experiments were conducted by first injecting slowly 0.4 ml dyed Guaiacol liquid into the bottom of the central part of the tube via port 2 (Fig. 5.1 and Fig. 5.2a). The liquid was then solidified by using an ice-water cooling bath for accelerating the freezing and by adding small crystals (< 5mg) that acted as nuclei for solidification. The crystals were generated by freezing Guaiacol at -20°C for 1 day. The solidified pool appeared as an overall flat continuous surface composed of snow-flakes, and needle-like crystals attached to the bottom glass wall (Fig. 5.2b). Glass beads were filled afterwards through a funnel above port 2. The glass tube was then filled with water at a low flow rate to avoid perturbation of the sediments. The tube with the beads was shaken manually to achieve a relatively flat surface (Fig. 5.2c). The water tank was filled with pre-degassed water to start the experiment. The flow rate in the conduit was then adjusted to the desired value (Appendix a, Table A1). The guaiacol source was kept in a solid state by using tap waters for the experiments with a temperature of 10 °C, which is below the melting point of Guaiacol (28 °C).

Although Guaiacol was kept as a solid, it is referred to as DNAPL pool given that we intend to simulate such a contamination scenario.

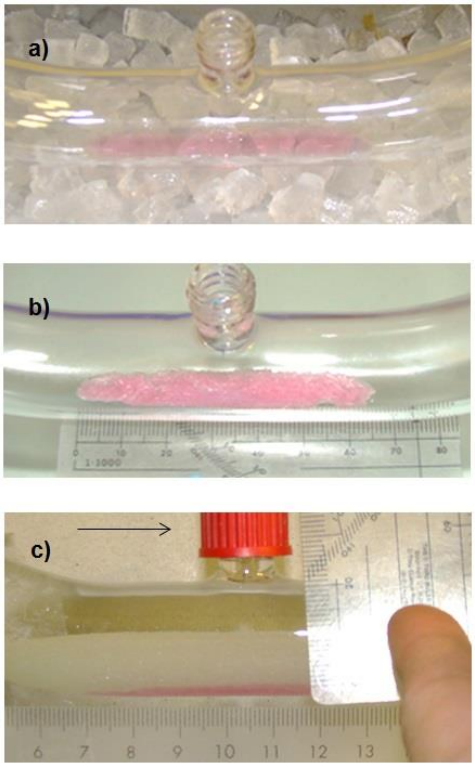

Fig. 5.2 Illustration of DNAPL pool creation with Guaiacol for dissolution tests.

The UV spectrophotometer was calibrated using degassed tap water spiked with Guaiacol. Calibration curve is reported in Appendix a, Fig. A8. The pumping rate to the flow cell was set to 12 ml/min to ensure that water in the sampling tube and flow through cell was renewed (total residence time of 5 s). Concentrations were averaged over a time interval of 20 s. In addition to the on-line UV measurement, water samples of 10 ml volume were withdrawn manually from the sampling port 3 (Fig. 5.1) at intervals depending on the duration of each experiment and kept in brown vials (as the compound is light-sensitive). They were measured with the UV spectrophotometer after the experiments in static conditions for comparison.

5.2.3 Flow characterization

In addition to the Guaiacol experiments, tracer test with a solid source resembling a DNAPL pool was carried out to visualize the shape of the plume originating from the DNAPL surface and its migration through the sediments. This was not possible with Guaiacol as it is colorless. Before filling glass beads into the tube, tracer in suspension (Sulforhodamine G) was injected and the water evaporated to create a solid coating along the central bottom wall of the glass tube.

Modeling approach

Numerical simulations were employed to further explore the impact of conduit geometry and conduit flow conditions on mass transfer rates using the same approach as presented in Chapter 3. Briefly, a two-domain approach was adopted with the Navier-Stokes equation describing fast conduit flow and Darcy's law describing low flow in the sediment domain. The two domains were coupled by imposing pressure continuity across the two domains. A Dirichlet boundary condition corresponding to saturated concentrations was prescribed at the pool surface. The DNAPL-water contact area was assumed to remain approximately constant during the experiment consistent with experimental observations.

The values of the main parameters are shown in Table 5.2. The permeability and dispersivities in sediments were calibrated by fitting the simulated results to the observed BTCs from sediment-source tracer tests carried out as described in Chapter 3. The molecular diffusion coefficient D_m was estimated by the method from Othmer and Thakar (1953). The effective diffusion coefficient D_e corresponded to $D_e = \tau D_m$ (Fetter, 1993; Zheng and Bennett, 2002), where τ is tortuosity, taking a value of 0.7 for sand (De Marsily, 1986). A constant concentration of 137 mol/m^3 was specified at the pool surface which corresponds to the guaiacol solubility at 15 °C (17g/L). The DNAPL pool had a surface area of 5.5 cm^2 and a thickness of 1.1mm based on measurements from the laboratory experiment.

Table 5.2 List of main parameters

Property	Symbol	Value	Unit
Permeability	k	1.6e-10	m2
Porosity	ε	0.38	[-]
Dispersivity	α_L	3e-3	
	α_{TH}	3e-4	m
	α_{TV}	3e-5	
Molecular diffusion coefficient	D_m	6e-10	m^2/s
Effective diffusion coefficient	D_e	4.2e-10	m^2/s
Conduit Dispersion	Dc	1e-4	m^2/s
Boundary concentration	C_s	137	mol/m^3
Pool thickness (max)		1.1	mm
Pool surface area		5.5	cm^2

Scaling analysis

As presented in Section 3.2.3 of Chapter 3, scaling effects have to be considered when relating findings from the laboratory experiment to the field scale. Scaling relationships show that the flow rate

in the porous medium of the scale model is much higher than in reality due to the higher pressure gradient imposed in the scale model for achieving the same Reynolds number as in a real system. Similar scaling analysis was carried out to relate the dissolution rate observed in the laboratory experiment to the field scale (see Appendix c.4 for details). The scaling analysis reveals that the lifetime of the DNAPL pool is much shorter in the scale model than in "reality" for a given *Re*. For a geometric scaling factor (model/reality) β (<1), the ratio of the DNAPL lifetime between model and reality scales with β^3–$\beta^{4.5}$ depending on whether diffusion or mechanical dispersion dominates mass transfer. However, the flow velocities in karst conduit are usually high with turbulence. Dissolution of DNAPLs is likely to be enhanced due to the high conduit Reynolds number in reality.

5.3 RESULTS AND DISCUSSION

5.3.1 Steady state concentration & conduit flow

The time-dependent effluent concentrations are shown in Fig. 5.3. The time was non-dimensionalized by dividing it by the time required to renew once the conduit volume. The concentration increased continuously until reaching a steady state. The steady state concentration was reached earlier at higher conduit flow rate and in the 45D compared to the 15D system. Steady state concentrations ranging from 200 to 400 µg/l were observed. Concentrations measured continuously by UV spectrophotometry were generally in agreement with those obtained by manual sampling and static measurements, with an average deviation of about 15%. The concentrations show a strong dilution of the solutes released from the DNAPL pool given that Guaiacol has a solubility of 17 g/l at 15°C. Steady state concentrations C_e varied little as function of the conduit flow rate. The simulated effluent concentrations are shown in Fig. 5.3, which were generally in a good agreement with the observed values except for conduit *Re* = 1600. At *Re* = 1600, the measured concentrations were only about half of the simulated concentrations.

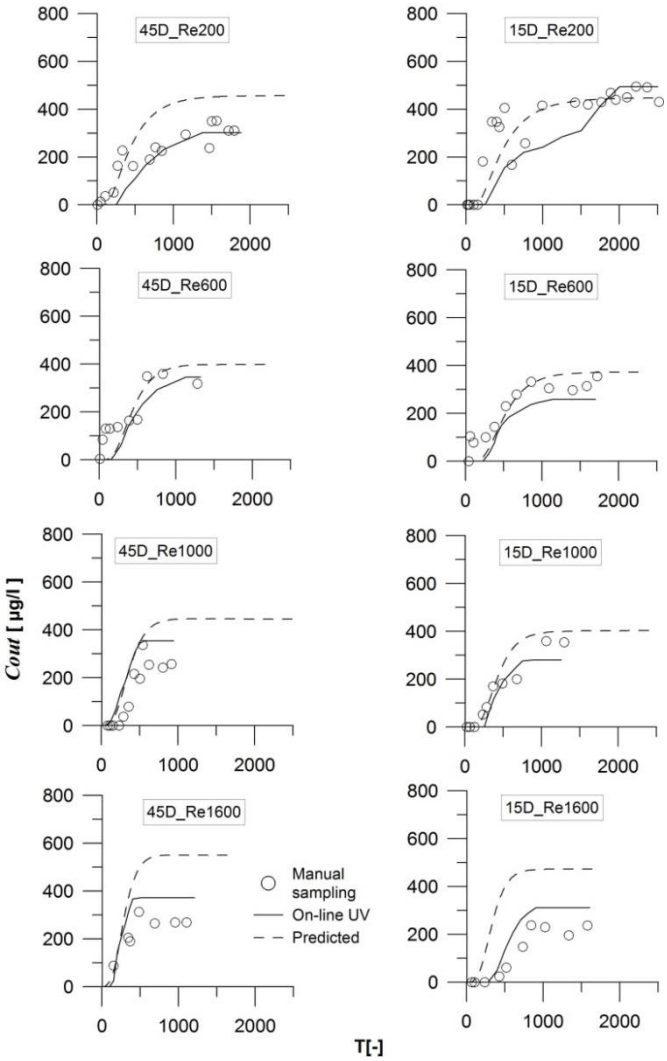

Fig. 5.3 Measured and simulated time-series of effluent concentrations at varied conduit flow rates (expressed by Reynolds number)

Solute plume originating from DNAPL pool

The solute plume originating from the DNAPL pool was traced experimentally by the dissolution of a solidified pool of tracer (Sulforhodamine G) and simulated with numerical model for comparison. The observed and simulated plume at *Re* = 600 for T = 3600 s is shown in Fig. 5.4a&b. The observed plume was generally well reproduced by numerical simulation (Fig. 5.4). Illustrations for other time steps can be found in Appendix a, Fig. A9.

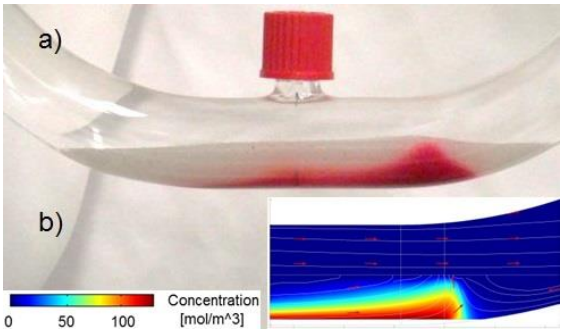

Fig.5.4 Observed and simulated solute plume at conduit Re 600 for 45D.

The simulated steady state concentration contours as a function of conduit *Re* are shown in Fig. 5.5. Concentrations decreased from the water/DNAPL interface (WDI) to the sediment water interface (SWI), where they reached a concentration close to zero. The shape and size of the plume was controlled by the flow field in sediment which was characterized by a zone of forward flow and a zone of reverse flow (detailed in Section 3.3.4 in Chapter3). The concentration boundary layer in the zone of forward flow became thinner with increasing conduit *Re* independent of conduit angle (Fig. 5.5). The effect of boundary layer/concentration gradients on mass transfer will be discussed in the following section 5.3.2.

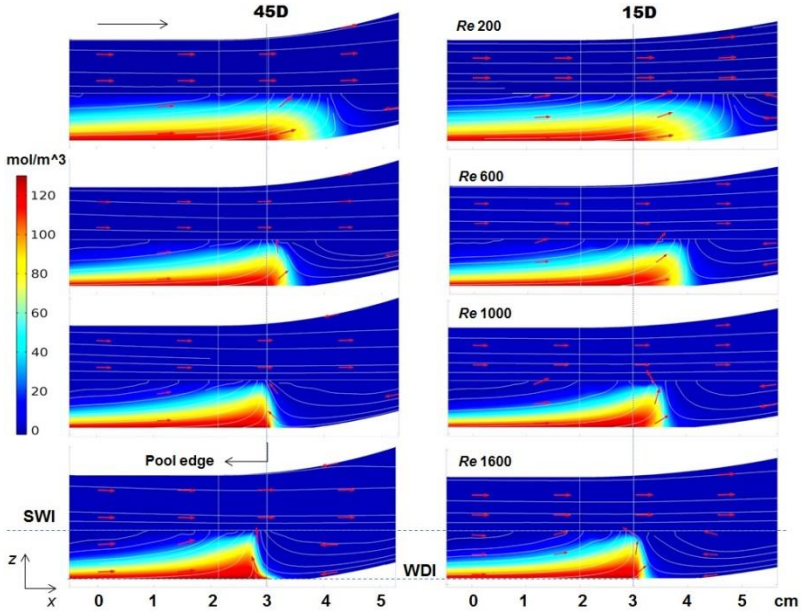

Fig. 5.5 Solute plumes of DNAPL pool depicts the concentration contours at steady state under varied conduit Reynolds number (*Re*) and flow fields (streamlines) for the 45D and 15D system. Pool edge denotes to the downstream end of DNAPL pool.

5.3.2 Mass transfer rate

For each experiment, the dissolution kinetics was characterized by calculating the mass transfer coefficient k_m. It is not a fundamental physical property, but rather an effective parameter influenced by different factors. The following equation was used to quantify mass transfer coefficients from the steady state effluent concentrations (Miller et al., 1990):

$$J = \frac{C_{out} \cdot Q}{A_{int}} = k_m (C_s - C_\infty) \quad \text{(Eq.5.1)}$$

where J ($ML^{-2}T^{-1}$) is the mass flux to the aqueous phase, C_{out} (ML^{-3}) is the average effluent concentration measured from experiments, Q (L^3T^{-1}) is conduit flow rate, A_{int} (L^2) is the DNAPL pool and water interfacial area, k_m (LT^{-1}) is the mass transfer coefficient, C_s (ML^{-3}) is the aqueous phase solute solubility concentration and C_∞ is the aqueous phase solute concentration further away from the DNAPL pool. C_∞ was set to be zero, as flow in the sediment was continuously renewed. Hence k_m can be obtained by:

$$k_m = \frac{C_{out} \cdot Q}{A_{int} \cdot C_s} \quad \text{(Eq.5.2)}$$

To calculate the mass transfer coefficient k_m, the steady state concentration measured by the continuous UV spectrometry was used as C_{out}.

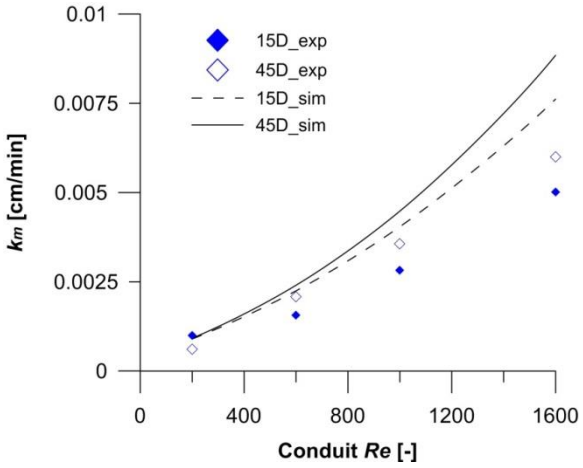

Fig. 5.6 Observed and simulated mass transfer coefficients k_m as a function of conduit Reynolds numbers (Re).

Fig. 5.6 shows the relationship between mass transfer coefficients k_m and conduit Reynolds number. The observed mass transfer coefficient increased with conduit *Re* and was higher for the steeper conduit angle at most flow conditions. The mass transfer coefficient at 45D was about 2% higher than at 15D for a conduit *Re* 200, and 14% higher for *Re* 1600, indicating that the influence of conduit angle on mass transfer increases at high conduit flow rates.

The mass transfer coefficients were also calculated with the modeled steady state concentrations, and were plotted in Fig. 5.6. The predicted values show generally a good agreement with the observed values at low to medium conduit flow rate, with deviations of 2 – 25%. However, simulation became less efficient in predicting k_m at high conduit flow, with deviations as high as 50%. This might be partly caused by the changing source function due to the substantial mass loss at high flow rates. The percentage of mass dissolved until reaching a steady state was about 10 – 13% at low flow, while it was 25 – 30% at high flow.

The mass transfer coefficients k_m of pool dissolution in the conduit and sediment system strongly depends on the flow velocity as shown in Fig. 5.6. In the following, the velocity dependence of the mass transfer coefficient was compared to the well-investigated case of a DNAPL pool in a semi-infinite homogenous porous media as a reference case. Such an approach was used because also in the current study, dissolution took place in a porous media, which was however of finite height. Using a 2D advection-dispersion equation for a pool of length L_p, an analytical expression for k_m has been derived by Johnson and Pankow (1992):

$$k_m = \frac{J}{C_s} = \frac{2\varepsilon}{\sqrt{\pi}}\sqrt{D_{TV}\overline{U}/L_p} \qquad \text{(Eq.5.3)}$$

where D_{TV} (L^2/T) is the transverse vertical dispersion coefficient, $D_{TV} = D_e + \alpha_{TV}\overline{U}$, $\overline{U}$ (L/T) is the average flow velocity, L_p (L) is the pool length, and ε is the porosity. The mass transfer coefficients k_m

predicted by the 2D analytical solution (Eq. 5.3) were plotted in Fig. 5.7 as a function of the average groundwater flow velocity $\overline{U}$ in the sediment. The results from the experiments and the numerical modeling are shown in the same figure (Fig. 5.7) for comparison. The measured and predicted (both numerical model and 2D analytical solution) k_m increased linearly with the average groundwater flow velocity (above 0.1 m/d). A linear relationship between k_m and $\overline{U}$ was also found in the DNAPL pool dissolution experiments by Schwille (1988). A linear trend is expected according to Eq.5.3 for higher velocities when mechanical dispersion dominated over diffusion. In this case, k_m approaches $2\varepsilon\overline{U}\sqrt{\alpha_{TV}/\pi L_p}$ (Eq.5.4). Both the observed and simulated k_m followed the same trend irrespectively of the conduit angle, suggesting that it is the average flow velocity in sediment that essentially controls the mass transfer rate, which is indirectly influenced by the conduit geometry/angle. In the following, concentration profiles of the simulated solute plume are plotted to explore how the flow velocity influences the mass transfer of DNAPL pool dissolution.

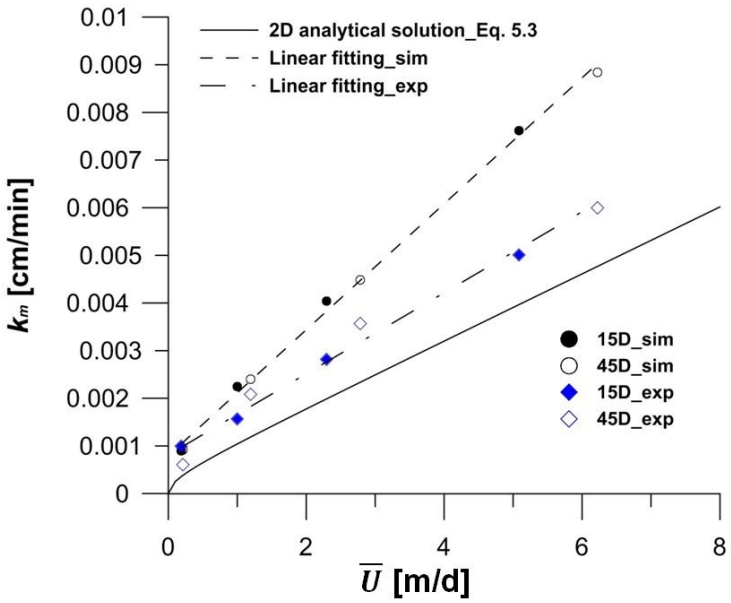

Fig. 5.7 Comparison of the observed and predicted mass transfer coefficient by numerical simulation and 2D analytical solution.

Concentration profiles at coordinate x = 0 under varied conduit Reynolds number were plotted to evaluate how concentration gradients above the WDI evolve with flow rate (Fig. 5.8). The steeper concentration gradients/thinner boundary layer thickness at higher *Re*, as well as the increased amount of water passing along the WDI led to the higher k_m. An increase in k_m with flow velocity was also observed in studies for homogeneous porous media containing DNAPL residue (Schaefer et al., 2009) or DNAPL pools (Chrysikopoulos and Lee, 1998).

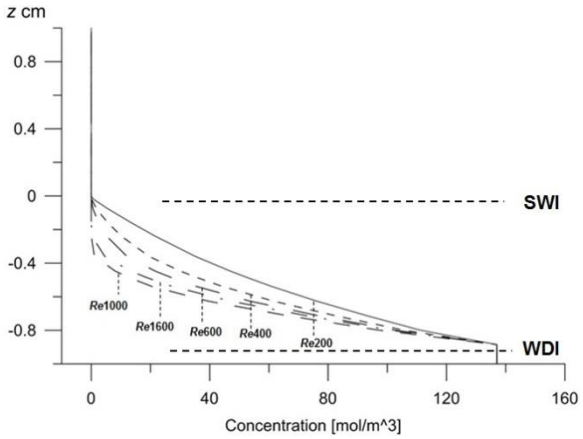

Fig. 5.8 Concentration profile at x= 0 at varied conduit Reynolds number (Re).

While the simple 2D analytical model predicted the linear relationship between k_m and $\overline{U}$, the k_m were smaller than both the observed and simulated values for the conduit system. This deviation is likely due to the conceptual simplification of DNAPL dissolution in the 2D model, e.g., the neglected transverse horizontal dispersion for large pool width. In order to investigate why the 2D model tends to underestimate the mass transfer rate, concentration profile of DNAPL pool dissolution was simulated by the 2D model and compared with the 3D model at an equivalent average groundwater flow velocity (1 m/d). Concentrations are generally higher for the 3D model than the 2D model (Fig. 5.9). This means that a higher mass of compounds has reached the aqueous phase in the 3D compared to the 2D case. The higher mass flux can be explained by the curved streamlines in the 3D model that advect molecules away from the WDI. In the 2D model, streamlines are parallel to the surface and molecules are only transferred away from the WDI by transverse dispersion. Hence the pattern of hyporheic flow in karst conduit sediment enhances mass transfer compared to a uniform flow field in an infinite porous media. In addition, transverse horizontal/vertical dispersion induced by the reverse flow at the downstream bend (Appendix a, Fig. A10) tends to carry solutes away from the WDI, which is also likely to yield mass transfer rate higher for the 3D conduit model than for the 2D model.

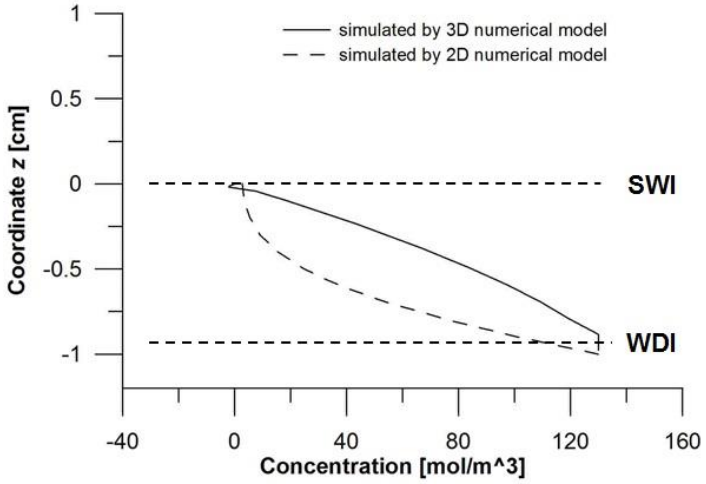

Fig. 5.9 Comparison of concentration profiles simulated by 2D and 3D model for 15D at coordinate x = 3 cm (downstream pool edge) under the same average groundwater flow velocity in the sediment (1 m/d)

5.3.3 Sensitivity analysis of main parameters

In this study, the conduit flow rate was shown to be one of the key parameters that control the rate of DNAPL pool dissolution. Sediment properties (permeability k, dispersivity α_{TV}) and DNAPL properties (pool length L_p, solubility C_s) influence the mass transfer rate as well. Sensitivity analyses were conducted by numerical simulations to evaluate the dependence of k_m on these parameters (Fig. 5.10). The parameters were varied within a typical range. The mass transfer coefficient increased with increasing permeability k, transverse dispersitivity α_{TV} and solubility C_s, while it decreased with increasing pool length L_p. The sensitivity of k_m to these parameters was higher at higher Re. k_m increased linearly with sediment permeability k which appears to be the most sensitive variable (Fig.5.10a). This trend is expected as k_m varies linearly with the flow velocity (see above) and the flow velocity is proportional to k according to Darcy's law. The non-linear trends for α_{TV} and L_p are consistent with Eq.5.4, which predicts that k_m varies according to a power law approximately with exponents of 0.5 and -0.5 (R^2 value of 0.97-0.99 for α_{TV}, and 0.92-0.96 for L_p), respectively. However, k_m increased also with C_s, though least strongly, in contrast to what is expected in the 2D model.

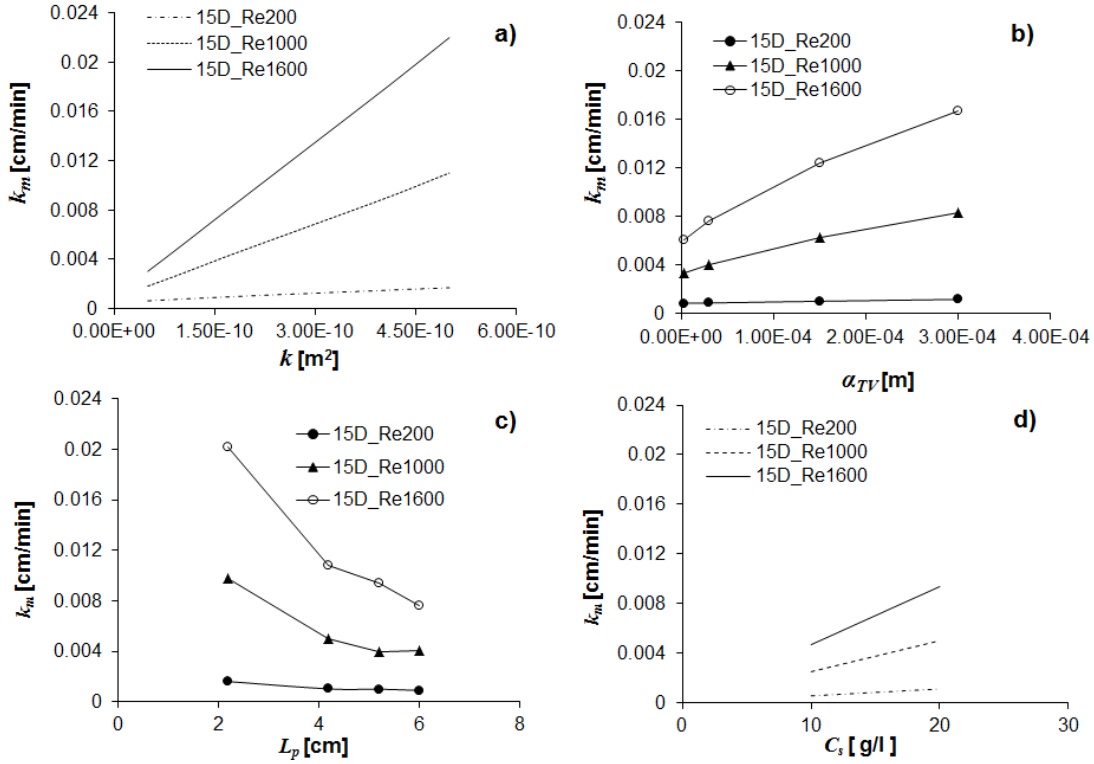

Fig. 5.10 Dependence of the mass transfer coefficient k_m on different variables

5.4 SUMMARY AND CONCLUSIONS

The study investigated the dissolution of DNAPL pools entrapped in karst conduit sediments in a laboratory analog model. A well-defined DNAPL pool was created to evaluate the influence of conduit flow rate and conduit angle on the mass transfer of pool dissolution. The solute plume originating from the DNAPL pool was visualized with a soluble tracer. A two-domain flow model was calibrated

and applied to simulate the dissolution process. The effects of flow field on the mass transfer of pool dissolution were explored by numerical simulation. The mass transfer of pool dissolution in the sediment of karst conduit was also compared to that occurring in the semi-infinite porous media as a reference case. In addition, sensitivity analyses were carried out by numerical simulations to evaluate the dependence of mass transfer rate on different variables.

Results of the dissolution experiments showed that the effluent concentrations were highly diluted compared to the DNAPL solubility at the source zone. The mass transfer coefficient k_m increased with the conduit flow rate and was higher for the steeper conduit angle. Thinner boundary layer thickness/steeper concentration gradients as well as the increased amount of water flow passing WDI led to the higher mass transfer with the increasing conduit flow rate. The relationship between k_m and the average groundwater flow velocity $\overline{U}$ in the sediment was linear for a velocity range where mechanical dispersion dominates over diffusion in both the experiments and in the numerical model. However, the observed and model k_m for the sediments in the conduit was higher than the one calculated by the 2D analytical solution for the semi-infinite porous media. The higher dissolution rate was likely attributed to hyporheic flow pattern characterized by vertical upward flow indicated by simulations of flow fields and concentration profiles. Conduit angle had an effect on the mass transfer rate by influencing the average flow velocity in sediment essentially. Sediment permeability was found to have the strongest influence on k_m by sensitivity analyses.

The study has some implications on the DNAPL behaviors in karst aquifer. Sediment-entrapped DNAPLs will provide a persistent contamination source to karst springs by hyporheic exchange between conduit flow and the underlying sediment. For a same conduit flow rate, the lifetime of DNAPLs is much longer in the field scale than in the laboratory analog as the mass transfer rate is much smaller in reality than in the model by scaling analysis. However, compared to the DNAPL pool dissolution in a semi-infinite porous medium, DNAPL longevity is anticipated to be shorter in karst conduit sediment due to the influence of karst hyporheic flow. While the model DNAPL in the study was kept immobile during dissolution, the migration of DNAPL associated with the flow and sediment plays also roles in the longevity of DNAPLs in karst aquifer. In addition, the effect of sediment properties deserves further investigations due to its important role in hyporheic exchange. Other karst hyporheic flow-mediated biogeochemical processes, such as the transport of colloids, heavy metals, and microbial degradation of contaminants could be future study interests.

5.5 REFERENCE

Anderson, M.R., Johnson, R.L., Pankow, J.F., 1992a. Dissolution of dense chlorinated solvents into ground-water .1. Dissolution from a well-defined residual source. Ground Water, 30(2): 250-256.

Anderson, M.R., Johnson, R.L., Pankow, J.F., 1992b. Dissolution of dense chlorinated solvents into groundwater .3. Modeling contaminant plumes from fingers and pools of solvent. Environmental Science & Technology, 26(5): 901-908.

Boards, S.M.E.a.L., 1913. A handbook of useful drugs. Press Of The American Medical Association, Chicago.

Chrysikopoulos, C.V., 1995. 3-dimensional analytical models of contaminant transport from nonaqueous phase liquid pool dissolution in saturated subsurface formations. Water Resources Research, 31(4): 1137-1145.

Chrysikopoulos, C.V., Lee, K.Y., 1998. Contaminant transport resulting from multicomponent nonaqueous phase liquid pool dissolution in three-dimensional subsurface formations. Journal of Contaminant Hydrology, 31(1-2): 1-21.

Chrysikopoulos, C.V., Lee, K.Y., Harmon, T.C., 2000. Dissolution of a well-defined trichloroethylene pool in saturated porous media: Experimental design and aquifer characterization. Water Resources Research, 36(7): 1687-1696.

Crawford, N.C., Ulmer, C.S., 1994. Hydrogeologic investigations of contaminant movement in karst aquifers in the vicinity of a train derailment near lewisburg, tennessee. Environmental Geology, 23(1): 41-52.

De Marsily, G.P., 1986. Quantitative hydrogeology: Groundwater hydrology for engineers. Academic Press, San Diego.

Dickson, S.E., Thomson, N.R., 2003. Dissolution of entrapped DNAPLs in variable aperture fractures: Experimental data and empirical model. Environmental Science & Technology, 37(18): 4128-4137.

Ewers, R.O., White, K.A., Paschl, K., Hanish, M.B., 2005. Shallow groundwater and dnapl movement within slightly dipping limestone, southwestern kentucky. Sinkholes and the Engineering and Environmental Impacts of Karst: 365-379.

Fetter, C.W., 1993. Contaminant hydrogeology. Prentice-Hall, Upper Saddle River, New Jersey.

Han, B.P., Wang, X.Y., 2004. Groundwater contamination by carbon tetrachloride in Karstic area in China. Acta Scientiae Circumstantiae (In Chinese), 24(6): 982-988.

Harvey, J.W., Wagner, B.J., Bencala, K.E., 1996. Evaluating the reliability of the stream tracer approach to characterize stream-subsurface water exchange. Water Resources Research, 32(8): 2441-2451.

Iker, B.C., Kambesis, P., Oehrle, S.A., Groves, C., Barton, H.A., 2010. Microbial atrazine breakdown in a karst groundwater system and its effect on ecosystem energetics. Journal of Environmental Quality, 39(2): 509-518.

Imhoff, P.T., Arthur, M.H., Miller, C.T., 1998. Complete dissolution of trichloroethylene in saturated porous media. Environmental Science & Technology, 32(16): 2417-2424.

Jancin, M., Ebaugh, W.F., 2002. Shallow lateral DNAPL migration within slightly dipping limestone, southwestern Kentucky. Engineering Geology, 65(2-3): 141-149.

Johnson, R.L., Pankow, J.F., 1992. Dissolution of dense chlorinated solvents into groundwater .2. Source functions for pools of solvent. Environmental Science & Technology, 26(5): 896-901.

Kim, T.J., Chrysikopoulos, C.V., 1999. Mass transfer correlations for nonaqueous phase liquid pool dissolution in saturated porous media. Water Resources Research, 35(2): 449-459.

Loop, C.M., White, W.B., 2001. A conceptual model for DNAPL transport in karst ground water basins. Ground Water, 39(1): 119-127.

Mahler, B., Massei, N., 2007. Anthropogenic contaminants as tracers in an urbanizing karst aquifer. Journal of Contaminant Hydrology, 91(1-2): 81-106.

Miller, C.T., Poiriermcneill, M.M., Mayer, A.S., 1990. Dissolution of trapped nonaqueous phase liquids - mass-transfer characteristics. Water Resources Research, 26(11): 2783-2796.

Orghidan, T., 1959. Ein neuer Lebensraum des unterirdischen Wassers, der hyporheische Biotop. Archiv für Hydrobiologie, 55(3): 392-414.

Othmer, D.F., Thakar, M.S., 1953. Correlating diffusion coefficients in liquids. Industrial and Engineering Chemistry, 45(3): 589-593.

Powers, S.E., Abriola, L.M., Weber, W.J., 1992. An experimental investigation of nonaqueous phase liquid dissolution in saturated subsurface systems - steady-state mass-transfer rates. Water Resources Research, 28(10): 2691-2705.

Powers, S.E., Loureiro, C.O., Abriola, L.M., Weber, W.J., 1991. Theoretical-study of the significance of nonequilibrium dissolution of nonaqueous phase liquid in subsurface systems. Water Resources Research, 27(4): 463-477.

Schaefer, C.E., Callaghan, A.V., King, J.D., McCray, J.E., 2009. Dense nonaqueous phase liquid architecture and dissolution in discretely fractured sandstone blocks. Environmental Science & Technology, 43(6): 1877-1883.

Schwille, F., 1988. Dense chlorinated solvents in porous and fractured media - Model experiments. Lewis, Boca Raton, FL.

White, W.B., 2002. Karst hydrology: recent developments and open questions. Engineering Geology, 65(2-3): 85-105.

Wolfe, W.J., Haugh, C.J., Webbers, A., Diehl, T.H., 1997. Preliminary conceptual models of the occurrence, fate, and transport of chlorinated solvents in karst regions of Tennessee. USGS Water-Resources Investigation Report 97-4097.

Zhang, J.P., Qi, S.H., Yao, H.L., 2011. The distribution characteristics of OCPs residues in karst underground river of Guangxi. Environmental Pollution & Control (In Chinese), 33(4): 54-57.

Zheng, C., Bennett, G.D., 2002. Applied contaminant transport modeling. Wiley interscience, New York.

Chapter 6 Summary, Conclusions and Outlook

Summary

DNAPLs are preferentially entrapped in karst conduit and sediment system, due to the good surface-and-subsurface connectivity in karst aquifer and the special physico-chemical properties of DNAPLs. The main purpose of the study was to evaluate the lifetime of sediment-entrapped DNAPL pool in karst conduit aquifer that will contaminate a spring and the controlling factors of dissolution rate. Pools are a likely morphology for DNAPLs that accumulate at the impermeable sediment/bedrock interface. The flow rate and pattern though the sediments will directly influence the dissolution process. Hence, the exchange of flow between conduit and the underlying sediment was first investigated, which was termed as karst hyporheic flow in the thesis in analogy to hyporheic exchange in surface hydrology studies. As suggested by recent field studies, hyporheic flow in karst sediments could potentially play a significant role in the transport and fate of contaminants in karst aquifer. However, karst hyporheic flow processes and their effects on DNAPL dissolution have not been investigated so far, which motivated this thesis.

The thesis consisted of two core parts: 1) The first part was devoted to the conduit-sediment exchange processes and the effects of different controlling factors on the pattern and magnitude of hyporheic flow; 2) The second part investigated the dissolution of sediment-entrapped DNAPL pool facilitated by hyporheic exchange. Laboratory studies of hyporheic exchange and the hyporheic exchange-mediated DNAPL pool dissolution were performed with an analog model resembling a karst siphon conduit partly filled with sediments. The analog consisted of glass tubes (conduit angle of 15D and 45D respectively) representing conduits and glass beads representing the sediment matrix. Soluble tracer Uranine was used as solute to trace flow and transport process in sediment. A surrogate DNAPL with a well-defined pool morphology was used for a quantitative analysis of the mass transfer rate of DNAPL compounds to the aqueous phase.

To characterize hyporheic flow pattern, sediment-source tracer tests were carried out under varied flow rates via direct injection of tracer solution into sediment consisting of coarse beads. Influences of conduit *Re* and conduit angle on the mean travel time (MTT) and dispersion (variance σ^2) of tracer plume were evaluated by evaluating the BTCs from tracer tests. Numerical modeling was employed to reproduce the sediment-source tracer test and to analyze the flow fields in the sediment. The simulation applied a two-domain approach for the conduit-sediment, with the Navier-Stokes equation describing conduit flow, and Darcy's law flow motion in the sediments. Flow fields were coupled by assuming pressure continuity across the two domains. The solute transport process was modeled by

the advection-dispersion equation. The relationship between the overall exchange flux and different controlling factors were explored using numerical simulations.

The results of sediment-source tracer tests showed that independent of the conduit angle, MTT and σ^2 decreased with increasing conduit *Re* and were smaller for a steeper conduit angle. The measured tracer breakthrough curves (BTCs) were well reproduced by numerical modeling, which validated the mathematical representation of the flow and transport processes in the system. The effect of conduit angle on MTT and σ^2 tended to disappear at high conduit *Re* (2000), consistent with numerical simulations that indicate similar flow velocities for the two conduit angles at high *Re*. The hyporheic flow pattern was characterized by a zone of forward flow and a zone of reverse flow in the sediment both by observation and simulation. The reverse flow was caused by the reverse pressure gradient along the sediment and water interface (SWI) at the downstream bend. The zone of reverse flow became more extensive with increasing conduit *Re*. The reverse pressure gradient originated from the higher pressure at the outer wall of the downstream bend, which was induced by the centrifugal force of flowing water when passing through the bend. Streamlines in sediment at low *Re* were relatively horizontal, whereas, they became curved at higher conduit flow influenced by the hyporheic flow pattern. The simulated flow field was non-uniform in the sediment with higher velocity magnitudes near the bends where a stronger flushing intensity occurred. The calculated overall exchange flux q_{int} between the two domains by numerical simulation increased linearly with the conduit flow rate, and was higher for the steeper conduit angle. For the steeper conduit, as much as 2% (for coarse beads) of the conduits flux transited through the sediment of coarse grains.

The effect of sediment properties on the hyporheic exchange was further investigated through sediment-source tracer tests using sediments of different grain size and numerical simulations. Permeability of sediment chosen for experiments ranged from 1e–10 to 1e–9 m^2, representing well sorted sand to gravel. Sediment-source tracer tests showed that the MTT and σ^2 of the tracer plume decreased with the increase of sediment grain size/permeability and conduit flow rate, and were smaller for the steeper conduit angle. Numerical tracer tests showed that the flow patterns (but not its magnitude) in the sediments were similar for all sediments. This is expected as the pressure distribution imposed at the SWI is independent of the sediment properties. Analysis of relationships established among the simulated exchange flux q_{int} and different controlling factors suggested a stronger influence of sediment properties (permeability *k*) on the magnitude of hyporheic exchange than conduit flow condition (*Re*), and conduit angle.

Once the hyporheic exchange processes were well understood, a surrogate DNAPL pool was created to investigate the relationship of the hyporheic exchange-mediated mass transfer with conduit flow and conduit angle. Tracer test with a solid source (soluble tracer Sulforhodamine G) was carried out to trace the solute plume from the water/DNAPL interface (WDI). The observed plume was compared to results of the numerical simulation of pool dissolution and used for exploring the influence of the flow fields on the mass transfer rate. Results of the mass transfer were also compared

with the well-investigated case of pool dissolution in a semi-infinite porous media as a reference to highlight specific features of pool dissolution in the karst conduit-sediment system. Expected dissolution rates for the reference scenario were characterized using a 2D analytical solution.

The observed mass transfer coefficient k_m for quantifying the mass transfer rate increased with conduit flow rate and was higher at a steeper conduit angle. The k_m increased linearly with the average groundwater flow velocity $\overline{U}$ in sediments for both experiments and simulations. However, the observed and model k_m were higher than that calculated by the 2D analytical model. The higher k_m was caused by the hyporheic flow pattern which enhanced solute transport away from the source by the curved streamlines. In addition, the transverse horizontal dispersion likely also contributed to the higher k_m in 3D than the 2D model due to small pool width. The conduit angle essentially influenced the mass transfer rate via flow velocity in the sediment. Sensitivity analyses of the mass transfer coefficient k_m showed that sediment permeability k was the most sensitive variable due to its influence on flow velocity in sediment.

In conclusion, the study confirmed that hyporheic exchange could occur between karst conduits and sediment using a laboratory analog. The conduit angle-influenced pressure distribution along the SWI, acted as the driving force for transferring fluid into the sediment, in contrast to streambed sediments where bedforms usually play a key role. The pattern and magnitude of the hyporheic flow was influenced by the combined effects of conduit flow rate, sediment properties and conduit angle. Therein, flow patterns were determined by the pressure gradients at the SWI which evolve with both the conduit flow rate and conduit angle independent of sediment properties. The magnitude of flow in sediment was only influenced by sediment properties (grain size/permeability) for the same conduit geometry and conduit flow rate. The dissolution rate of sediment-entrapped DNAPL pools was highly influenced by the hyporheic flow between conduit and the sediment. The mass transfer of DNAPL pool dissolution was found to increase linearly with the average groundwater flow velocity in sediment. Compared to the dissolution of a DNAPL pool in a semi-infinite porous medium, a higher mass transfer and shorter lifetime is to be anticipated in karst conduits with shallow sediment due to the influence of hyporheic flow pattern. The study also demonstrated that numerical modeling with the two-domain approach was valid and efficient in simulating hyporheic flow and predicting DNAPL pool dissolution. Last but not least, scaling analyses suggested that a much smaller exchange flux and much lower mass transfer rate occur in reality than in the investigated analog model. Hence a much longer lifetime of DNAPLs in reality than in the laboratory model is to be expected. However, flow conditions in reality need to be taken into account for the evaluation of the dissolute rate and lifetime of DNAPLs.

Problems and future study

The term ‘karst hyporheic flow’ was proposed quite recently. There is a lack of knowledge about the occurrence and fate of DNAPLs in karst aquifer compared to porous media. The thesis provided a first investigation of the karst hyporheic flow-facilitated DNAPL pool dissolution with a conceptualized laboratory analog model. However, the occurrence of hyporheic flow and relevant processes still need to be verified by field investigation, e.g. in phreatic karst conduits. The analog model was conceptualized to ressemble karst conduits developed in the limestone of very low primary porosity. Hence, the feature of karst aquifer needs to be considered when applying this theoretical study of karst hyporheic flow to field cases.

While the study mainly focused on the low laminar flow regime in conduits and sediments were kept stable, the influences of turbulent flow on the hyporheic exchange as well as contaminant behavior associated with sediment motion need further investigations. For future laboratory studies large devices should be used to reduce scale effects and to be able to carry out experiments that correspond to higher flow rates in the field. Guaiacol was demonstrated to be a promising surrogate for simulating DNAPL dissolution processes due to its low melting point and high solubility. However, the dissolution of real DNAPLs of different solubilities (much lower than Guaiacol) and a mixture of DNAPLs need further investigations as they are commonly the situations encountered in field.

The karst hyporheic flow-mediated geochemical processes could be of future interest, which will bring new insights into the occurrence and attenuation of contaminants in karst aquifer. Although karst aquifers are conventionally considered to be fragile due to the fast transport of contaminants by conduit flow, hyporheic flow through the underlying sediment may lead to some self-purification. Nitrification and denitrification processes occurring in karst conduits could be influenced by flow exchange with sediments, leading to a source or sink of nitrate. Organic compounds could be degraded by microbial processes in cave sediment, which also in turn influence the microbial community diversity. Therefore, the hyporheic flow and relevant processes need to be taken into account when evaluating vulnerability of karst aquifers.

Appendices

a. Additional figures

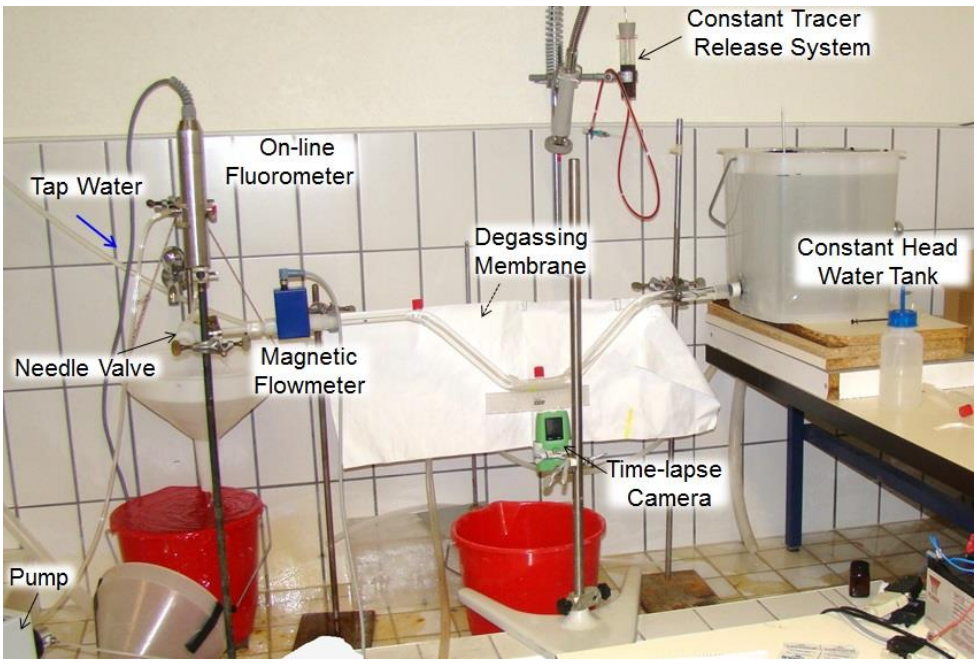

Fig. A1 Experimental setup for tracer tests

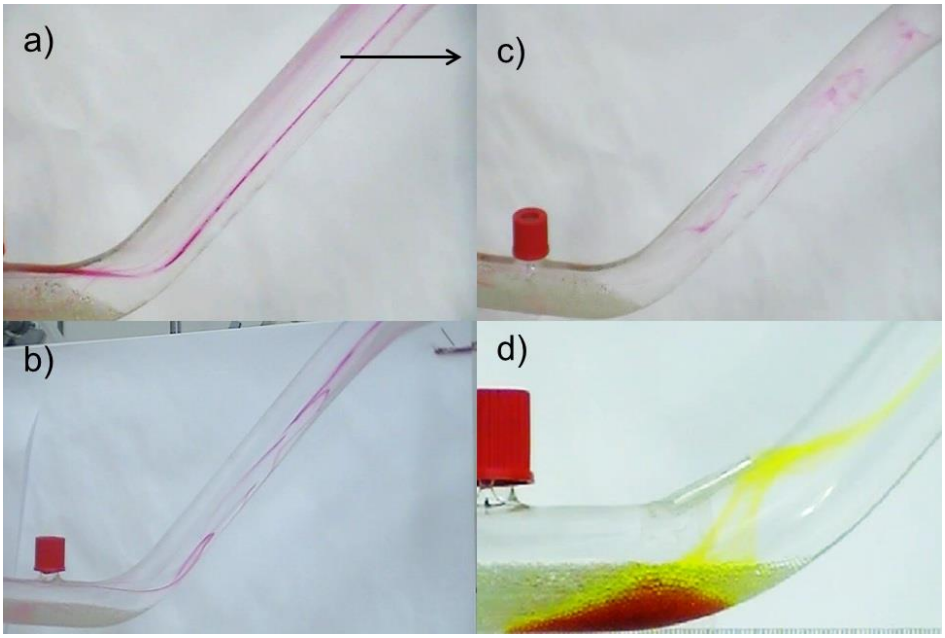

Fig. A2 Flow regimes at downstream bend in Reynolds experiments. a)Laminar; b)Transitional flow; c)Turbulent; d) Observed secondary flow at bend

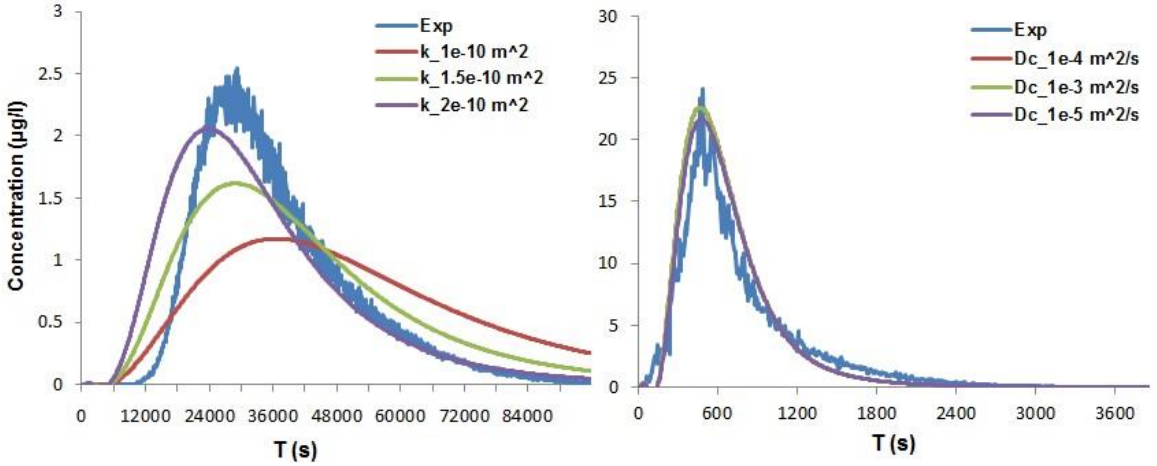

Fig. A3 Sensitivity test of simulated BTC to k (Permeability) and Dc (Dispersion coefficient in conduit)

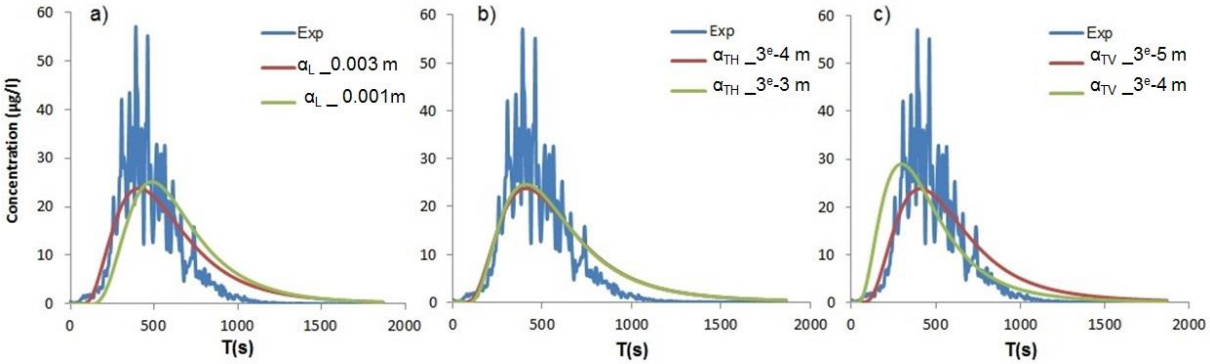

Fig. A4 Sensitivity test of simulated BTC to dimensional dispersivity in sediment

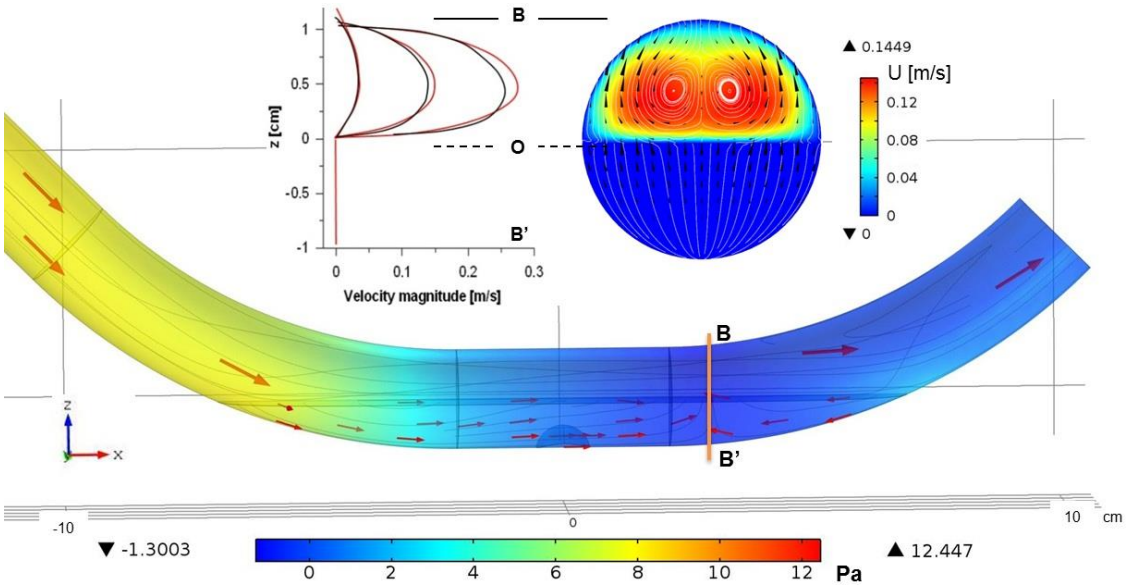

Fig. A5 Illustration of pressure distribution, velocity profile, and secondary flow at conduit *Re* = 1000 in 45D

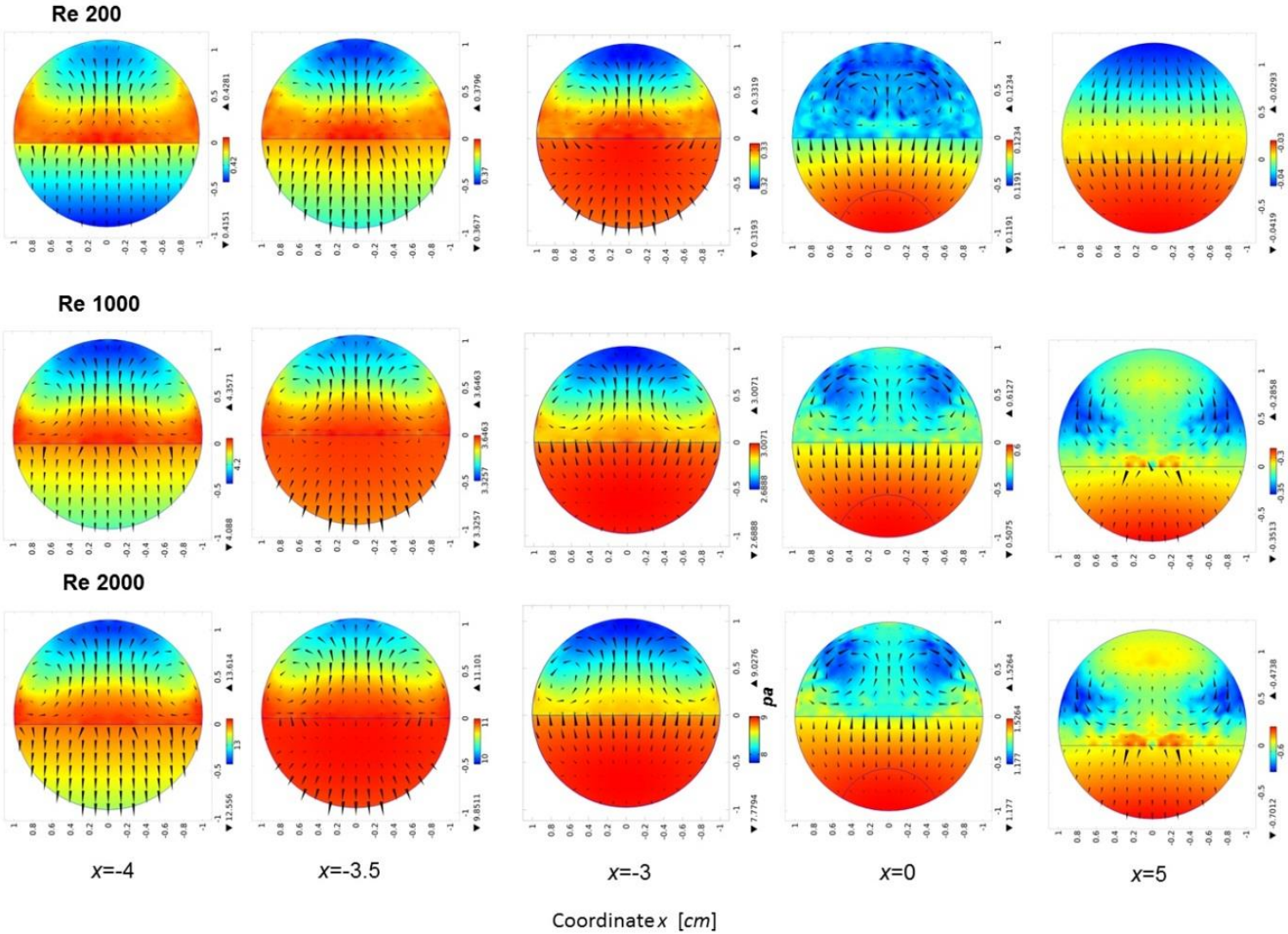

Fig. A6 Secondary flow motion (streamline line) and pressure field at the cross-section of conduit under varied conduit flow rates from up to downstream

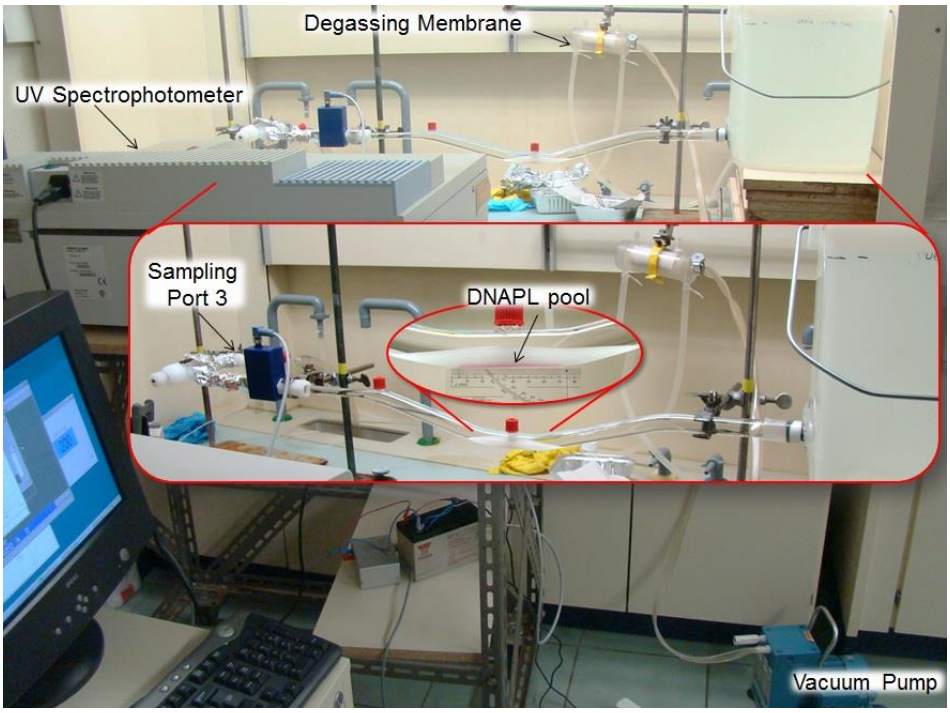

Fig. A7 Experimental setup for DNAPL pool dissolution tests

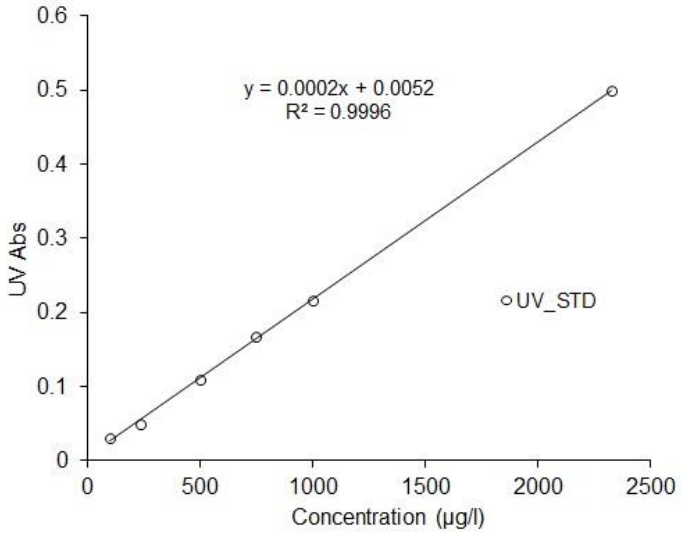

Fig. A8 Standard curve of concentration measured by UV spectrum

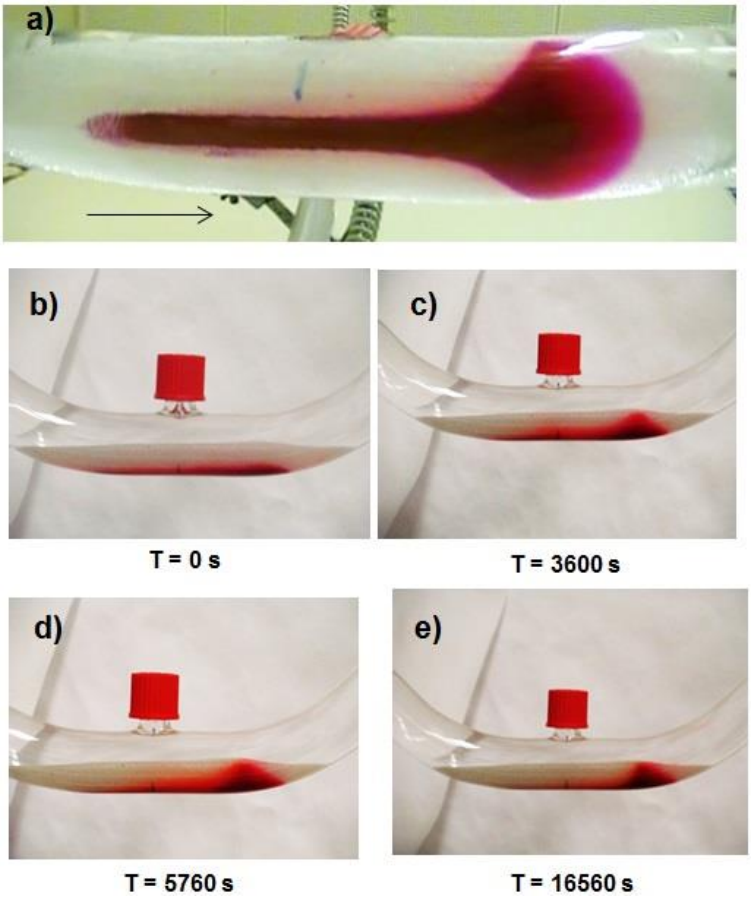

Fig. A9 The observed time-dependent dissolving plumes in tracer test with tracer Sulforhodamine G at a conduit Reynolds number of 600 for 45D.

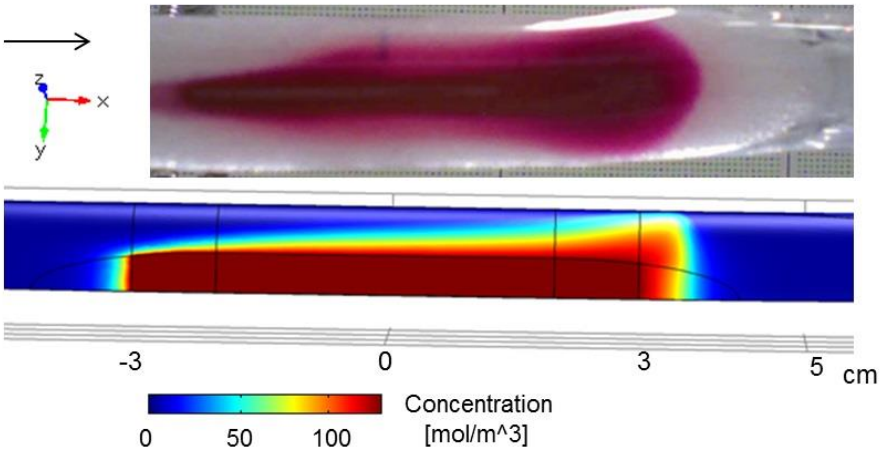

Fig. A10 45D Re = 600 Transverse Dispersion Illustration

Table A1 Tracer experiments information

	Mean flow velocity (cm/s)	*Re*	Mass recovered* (µg)	Resdience time[-]	Residence time [hour]
	1.0	194	216	488	6.67
	2.0	397	213	324	2.17
	3.0	601	216	186	0.83
45D	5.0	993	201	180	0.48
	7.9	1589	196	141	0.24
	10.0	1995	205	145	0.19
	1.0	202	218	947	12.6
	1.9	390	213	673	4.58
	3.0	602	213	510	2.25
15D	5.0	997	197	400	1.07
	8.0	1592	201	251	0.42
	10.0	1994	191	242	0.31

*Injected mass in all experiments is 220 µg

b. In-conduit impulse tracer tests

Impulse tracer tests were performed for the estimation of dispersion coefficient D_c in conduit assuming the dispersion is isotropic. The tracer solution of Uranine (40 mg/l, 0.5ml) was injected via the upstream port 1 and the central port 2, and the downstream BTC was monitored by the fluorometer at the outlet. The value of dispersion coefficient was evaluated by fitting the observed BTCs in the code CXTFIT as plotted in Fig. A13 below, for conduit *Re* = 200 to *Re* = 2000. Generally, before the onset of turbulence, the dispersion increases with flow velocity, which is in agreement with that observed for straight tube (Taylor, 1953). Compared to the values calculated by the analytical equation (Lee, 2004) for straight tube of the equal length, D_c are smaller, indicating the smaller dispersion contributed by curved bends. The dispersion shows the trend to decrease with the increasing flow rate at transitional flow regime (*Re* = 500 — *Re* = 1500). The theoretical equilibrium Taylor's dispersion coefficient under laminar regime ranges from 0.5 to 50 m^2/s, which is not achievable due to the small scale of the laboratory analog.

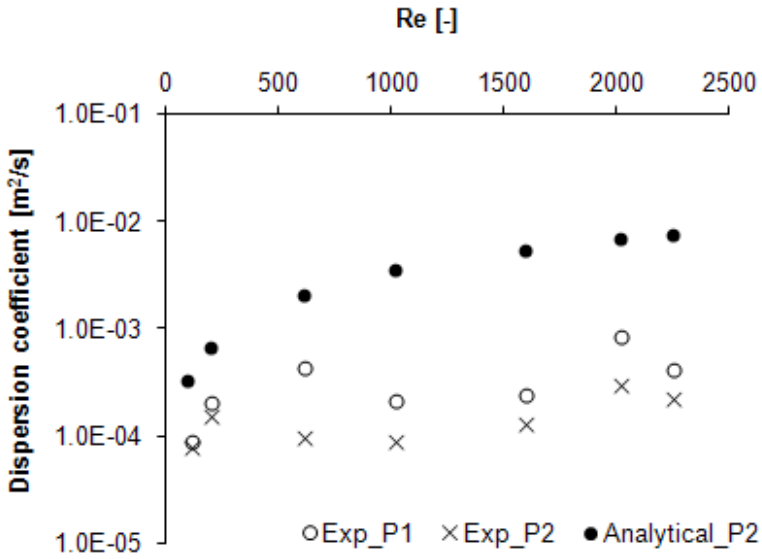

Fig. A13 Dispersion coefficient from in-conduit impulse tracer tests; P1 is injection port upstream, P2 is injection port at the central bottom, the same as for sediment-source tracer tests. The analytical equation is referenced to (Taylor, 1953).

c. Scaling analysis

In terms of the transferability of the laboratory model to the real system, scale analysis was performed. The similarity between two objects includes two criteria: geometric and dynamic similarity (McDonough, 2009).

In particular, if flow fields associated with two geometrically similar objects have the same Reynolds (pipe flow) and Froude numbers (open channel flow), then they have the same scaled velocity and pressure fields. In turn, it is easily seen from the equations of motion that this implies that they will exhibit the same scaled forces at all locations in the flow. Then, in light of geometric similarity, the unscaled forces will be in a constant ratio at all corresponding points of the two flow fields, and dynamic similarity will have been achieved. Hence, for flows in, or around, geometrically similar objects, dynamic similarity is achieved if all dimensionless parameters associated with these flows are the same.

In the following, it explored how different properties scale between the model (glass tube) and "reality". It is assumed that the model fulfills the criteria of geometric similarity and the analysis focusses on the dynamic similarity. A key objective is to evaluate how the free flow and porous media flow scale, and how the ratio between porous media flow and free flow scales. In other words, the goal is to find out how the ratio between porous media and free flow would be in the full scale situation (denoted as "reality"). The derivations are based on the principle that in a closed pipe, Reynolds scaling applies (Chanson, 1999).

As a first step, dimensionless parameters are introduced and dimensionless governing equations.

The independent and dependent variables are scales as follows:

$$x^* = x/H\ ,\quad y^* = y/H\ ,\quad t^* = t/t_s$$

and

$$u^* = u/\overline{U_c}\ ,$$
$$v^* = v/\overline{U_c}\ ,$$
$$p^* = p/P_s$$

with *x*, *y* is the spatial coordinates, *u* and *v* is velocity components, *t* is the time, *H* is diameter of conduit, $t_s = H/\overline{U_c}$, $\overline{U_c}$ is the average flow velocity in conduit, $P_s = \rho \cdot \overline{U_c}^2$ (twice the dynamic fluid pressure), "*" quantities are all dimensionless. In the following, the subscript *m* denotes to model, *r* denotes to reality, *c* denotes to conduit and *p* denotes to porous medium.

The dimensionless incompressible continuity and N-S equations are given by: (McDonough, 2009).

$$\frac{\partial U^*}{\partial t^*} + U^* \cdot \nabla U^* = -\nabla P^* + \frac{1}{Re}\nabla^2 U^* \qquad \text{(Eq. A1)}$$

where U^* is the flow velocity vector, U^*, P^*, t^*, *Re* are all dimensionless,

Whereby the Reynolds number is given by:

$$Re = \frac{\overline{U_c}H}{\nu} \qquad \text{(Eq. A2)}$$

ν is the kinematic viscosity

c.1) Relationship between pressure field in model and reality

For a given *Re*, the scaled pressure field will be the same in the model and reality. The ratio of the unscaled pressure between reality and model at a location is given by:

$$\frac{p_r}{p_m} = \frac{p_r^* \cdot P_{s,r}}{p_m^* \cdot P_{s,m}} = \frac{p_r^* \cdot \rho \cdot \overline{U_{c,r}}^2}{p_m^* \cdot \rho \cdot \overline{U_{c,m}}^2}$$

If the Reynolds number is the same in the model and reality:

$$\frac{p_r}{p_m} = \frac{\overline{U_{c,r}}^2}{\overline{U_{c,m}}^2} \qquad \text{(Eq. A3)}$$

Given that the Reynolds number is the same:

$$\frac{\overline{U_{c,r}}}{\overline{U_{c,m}}} = \frac{H_m}{H_r} = \beta \text{ , and } \left[\frac{\overline{U_{c,r}}}{\overline{U_{c,m}}}\right]^2 = \beta^2$$

Where β is the geometric scaling factor

Hence:

$$\frac{p_r}{p_m} = \frac{\overline{U_{c,r}}^2}{\overline{U_{c,m}}^2} = \beta^2 \qquad \text{(Eq. A4)}$$

For a given Reynolds number, the unscaled pressure is proportional to the square of the conduit diameter or proportional to the square of the geometric scaling factor.

c.2) Dynamic similarity in laminar pipe flow

The concept of dynamic similarity can also be illustrated for laminar flow in tubes which can be descripted by an analytical equation (Hagen-Poiseuille equation). According to this equation, the maximum flow velocity in the center of the tube is given by:

$$\overline{U_c} = -\frac{1}{32\eta} \cdot \frac{\Delta p}{\Delta x} \cdot H^2 \qquad \text{(Eq. A5)}$$

Assuming two geometrically similar tubes are compared with a diameter H and a length Δx

Hence:

$$\frac{H_m}{H_r} = \frac{\Delta x_m}{\Delta x_r} = \beta \qquad \text{(Eq. A6)}$$

If models and reality are compared:

$$\beta = \frac{\overline{U_{c,r}}}{\overline{U_{c,m}}} = \frac{\Delta p_r / \Delta x_r}{\Delta p_m / \Delta x_m} \cdot \frac{(H_r)^2}{(H_m)^2} = \frac{\Delta p_r / \Delta x_r}{\Delta p_m / \Delta x_m} \cdot \frac{1}{\beta^2} \qquad \text{(Eq. A7)}$$

Inserting of Eq. A6 and rearrangement leads to:

$$\beta = \frac{\overline{U_{c,r}}}{\overline{U_{c,m}}} = \frac{\Delta p_r / \Delta x_r}{\Delta p_m /(\Delta x_r \cdot \beta)} \cdot \frac{1}{\beta^2} = \frac{\Delta p_r}{\Delta p_m} \cdot \frac{1}{\beta} \qquad \text{(Eq. A8)}$$

Or

$$\frac{\Delta p_r}{\Delta p_m} = \beta^2 \qquad \text{(Eq. A9)}$$

For a given Reynolds number the pressure drop across the tube is proportional to the square of the geometric scaling factor consistent with the general pressure scaling relationship given by Eq. A4.

Or for the pressure gradient:

$$\frac{\Delta p_r / \Delta x_r}{\Delta p_m / \Delta x_m} = \beta^3 \qquad \text{(Eq. A10)}$$

This equation shows that in the model a much higher pressure gradient needs to be applied than in the reality to reach a flow velocity that corresponds to the same Reynolds number. The higher pressure gradient likely also leads to a higher flow in the porous media (see below).

The volumetric flow rate is given by:

$$Q = \frac{\pi \cdot (H/2)^4}{8\eta} \cdot \frac{\Delta p}{\Delta x} \qquad \text{(Eq. A11)}$$

For a given Reynolds number the ratio of flow between the model and reality is:

$$\frac{Q_{c,r}}{Q_{c,m}} = \frac{H_r{}^4}{H_m{}^4} \cdot \frac{\Delta p_r / \Delta x_r}{\Delta p_m / \Delta x_m} = \frac{1}{\beta^4} \cdot \frac{\Delta p_r}{\Delta p_m} \cdot \frac{\Delta x_m}{\Delta x_r} = \frac{1}{\beta} \qquad \text{(Eq. A12)}$$

Hence for a given Reynolds number, the ratio of the flow rate between reality and model is inversely proportional to the geometric scaling factor.

c.3) Scaling of coupled porous media flow

So far only flow in a conduit was considered. In the following, it will be explored how flow in a coupled porous media scales. For simplicity, it is assumed that the porous media is placed around a straight tube and fulfills the criteria of geometric similarity. Furthermore, it is assumed that pressure continuity between conduit flow and porous media flow is established.

Assuming the cross-section of the porous medium layer is annular with a thickness of *b*, while the conduit has a diameter of *H*.

According to principle of geometric similarity, this ratio is the same for model and reality.

Given that b<<H, the ratio of the cross-section between the porous media and the conduit for the model is given by

$$\frac{A_{c,m}}{A_{p,m}} = \frac{(H_m/2)^2 \cdot \pi}{H_m \cdot \pi \cdot b_m} = \frac{H_m}{4b_m} = \frac{H_r \cdot \beta}{4b_r \cdot \beta} = \frac{H_r}{4b_r} = \frac{A_{c,r}}{A_{p,r}} \qquad \text{(Eq. A13)}$$

Hence in case of geometric similarity, the ratio of cross-section area between the porous media and conduit flow remain the same in model and reality.

The porous media cross-section scales as follows:

$$\frac{A_{p,r}}{A_{p,m}} = \frac{H_r \cdot \pi \cdot b_r}{H_m \cdot \pi \cdot b_m} = \frac{H_r \cdot b_r}{H_m \cdot b_m} = \frac{1}{\beta^2} \qquad \text{(Eq. A14)}$$

The Darcy flux in the porous media given by (assuming that the pressure gradient dominates and given that the porous media is placed horizontally):

$$q = K \cdot \frac{\Delta p}{\Delta x} \qquad \text{(Eq. A15)}$$

If the hydraulic conductivity is the same in the model and reality, the ratio of the Darcy flux between reality and model is given by:

$$\frac{q_r}{q_m} = \frac{K \cdot \Delta p_r / \Delta x_r}{K \cdot \Delta p_m / \Delta x_m} = \beta^3 \qquad \text{(Eq. A16)}$$

Hence, the Darcy flux scales with the power of three of the geometric scaling factor.

The flow rate in the porous media scales as follows:

$$\frac{Q_{p,r}}{Q_{p,m}} = \frac{A_{p,r}}{A_{p,m}} \frac{q_r}{q_m} = \frac{1}{\beta^2} \cdot \beta^3 = \beta \qquad \text{(Eq. A17)}$$

Finally, the ratio of the flux between porous media and free flow scales as follows:

$$\frac{Q_{p,r} / Q_{f,r}}{Q_{p,m} / Q_{f,m}} = \frac{Q_{p,r} / Q_{p,m}}{Q_{f,r} / Q_{f,m}} = \frac{\beta}{1/\beta} = \beta^2 \qquad \text{(Eq. A18)}$$

In other words, in "reality" the porous media flow rate relative to the free flow rate is by a factor of β^2 smaller than in the model. In other words, if the geometric factor is 0.04 (2cm glass tube versus 0.5m conduit), 625 less flow passed through the porous media in reality compared to the model. Or to maintain a similar proportion of flow in reality compared to the model, the hydraulic conductivity of the real system should be 625 times higher than the model (which is not really possible given that the hydraulic conductivity is already very high in the model).

The relationship between hydraulic conductivity and permeability is given by:

$$k(m^2) = K \cdot \frac{\mu}{\rho \cdot g} = K(m/s) \cdot 1.02 \cdot 10^{-7} ms$$

The permeability in the experiment corresponds to the following hydraulic conductivity:

$$K(m/s) = \frac{k(m^2)}{1.02 \cdot 10^{-7} ms} = \frac{1.4 \cdot 10^{-9} m^2}{1.02 \cdot 10^{-7} ms} = 1.4 \cdot 10^{-2} m/s$$

c.4) Scaling of mass transfer rate and lifetime of DNAPL pool dissolution

Based on the scale analysis on the flow in sediment, extensive analyses on the scaling of mass transfer rate between the reality and model were performed. For a DNAPL pool of regular geometry, e.g., rectangular pool, the solute mass flux to aqueous phase J ($ML^{-2}T^{-1}$) could be calculated by an analytical formula:

$$J = \frac{2C_s\varepsilon}{\sqrt{\pi}}\sqrt{D_{TV}\overline{U}/L_p} \qquad \text{(Eq. A19)}$$

Where C_S is the solubility of DNAPL, ε is the porosity of the medium, D_{TV} is the transverse vertical dispersion coefficient, $D_{TV} = D_e + \overline{U}\alpha_{TV}$, where D_e is the effective molecular diffusion coefficient, $\overline{U}$ is the average groundwater flow velocity in porous medium, α_{TV} is the transverse vertical dispersivity, L_p is the pool length

$$\frac{D_{TV,r}}{D_{TV,m}} = \frac{D_e+\overline{U}_r\cdot\alpha_{TV,r}}{D_e+\overline{U}_m\cdot\alpha_{TV,m}} \qquad \text{(Eq. A20)}$$

Case 1 At low groundwater velocities (0.1 m/d), D_{TV} is not scale dependent (Sudicky, 1986), assuming D_{TV} is the same in porous medium for the model and reality.

$$\frac{J_r}{J_m} = \frac{\sqrt{\overline{U}_r}}{\sqrt{L_{p,r}}}\cdot\frac{\sqrt{L_{p,m}}}{\sqrt{\overline{U}_m}} = \sqrt{\frac{q_r}{q_m}}\cdot\sqrt{\frac{L_{p,m}}{L_{p,r}}} \qquad \text{(Eq. A21)}$$

Substitute Eq. A16 into Eq. A21, the mass flux scales by:

$$\frac{J_r}{J_m} = \beta^2 \qquad \text{(Eq. A22)}$$

Case 2 At high groundwater velocities, influence of mechanical dispersion is significant, substitute Eq. A16 and Eq. A20 into Eq. A19, the mass flux scales by:

$$\frac{J_r}{J_m} = \frac{\overline{U}_r}{\overline{U}_m}\cdot\sqrt{\frac{L_{p,m}}{L_{p,r}}} = \beta^{3.5} \qquad \text{(Eq. A23)}$$

The relationship between mass transfer coefficient and mass flux is given by

$$k_m = \frac{J}{C_s - C_\infty} \qquad \text{(Eq. A24)}$$

where k_m is the overall mass transfer coefficient, C_s is the aqueous phase solute solubility concentration (ML^{-3}), C_∞ is aqueous phase solute concentration (ML^{-3}) which is assumed to be zero at the infinite boundary.

Hence,

$\frac{k_{m,r}}{k_{m,m}} = \beta^2$, low flow velocity < 0.1 m/d

$\frac{k_{m,r}}{k_{m,m}} = \beta^{3.5}$, high flow velocity > 1 m/d

Lifetime scaling of DNAPL pool

Supposing the dimensions of pool are L_p (Pool length), W_p (Pool Width), T_p (Pool thickness), the total mass of DNAPL pool will be $S_p=\rho_{DNAPL}\cdot L_p\cdot W_p\cdot T_p$, ρ_{DNAPL} is the density of DNAPL

$$\frac{T_{p,m}}{T_{p,r}}=\frac{S_{p,m}}{n_{p,m}}\cdot\frac{n_{p,r}}{S_{p,r}}=\frac{\rho\mathrm{DNAPL}}{\rho\mathrm{DNAPL}}\cdot\frac{L_{p,m}}{L_{p,r}}\cdot\frac{W_{p,m}}{W_{p,r}}\cdot\frac{T_{p,m}}{T_{p,r}}\frac{J_r}{J_m}\frac{L_{p,r}}{L_{p,m}}\frac{W_{p,r}}{W_{p,m}}=\beta\cdot(\beta^2\sim\beta^{3.5})=\beta^3\sim\beta^{4.5}$$

where n_p is the rate of mass transfer (M/T)

d. References

Chanson, H., 1999. The hydraulics of open channel flow. Amold, London, UK.

Lee, Y., 2004. Mass dispersion in intermittent laminar flow, University of Cincinnati, Cincinnati.

McDonough, J.M., 2009. Lectures in elementary fluid dynamics: Physics, Mathematics and Applications. University of Kentucky, Lexington, KY, pp. 83-98.

Sudicky, E.A., 1986. A natural gradient experiment on solute transport in a sand aquifer - spatial variability of hydraulic conductivity and its role in the dispersion process. Water Resources Research, 22(13): 2069-2082.

Taylor, G., 1953. Dispersion of soluble matter in solvent flowing slowly through a tube. Proceedings of the Royal Society A- Mathematical Physical and Engineering Sciences, 219(1137): 186-203.